REDUCING THE ACTIVATION OF THE IRIS REACTOR BUILDING USING THE SCALE/MAVRIC METHODOLOGY

A Thesis
Presented to
The Academic Faculty

By

Jordan M. McKillop

In Partial Fulfillment
of the Requirements for the Degree
Master of Science in Nuclear Engineering
School of Mechanical Engineering

Georgia Institute of Technology
December 2009

REDUCING THE ACTIVATION OF THE IRIS REACTOR BUILDING USING THE SCALE/MAVRIC METHODOLOGY

Approved by:

Professor Bojan Petrović, Advisor
School of Mechanical Engineering
Georgia Institute of Technology

Professor Nolan E. Hertel
School of Mechanical Engineering
Georgia Institute of Technology

Professor C.-K. Chris Wang
School of Mechanical Engineering
Georgia Institute of Technology

Date Approved: 11 November 2009

ACKNOWLEDGMENTS

Gratitude goes to my advisor, Dr. B. Petrović, for without his assistance, guidance, and back of the envelope calculations, this thesis would not be possible.

I would like to thank Drs. N. Hertel and Dr. C. Wang for taking time out of their busy schedules to sit on my committee.

I would like to thank Drs. F. Franceschini and G. Storrick from Westinghouse Electric Company who provided data on IRIS. I would also like to thank the following people from ENEA (Italy) who provided data and information for this thesis: Drs. K. Burn, M. Ciotti, M. Sarotto, and R. Orsi. D. Peplow from ORNL provided the activation cross sections in a convenient form and was very helpful working out issues with the MAVRIC sequence. He also provided alpha releases of SCALE6 and 6.1 which helped tremendously. Particular thanks to D. Hartmangruber who helped with input deck geometry debugging.

Recognition needs to be given to the people behind the CADIS and the FW-CADIS methods: Drs. J. C. Wagner and A. Haghighat. Their method was used to generate data. Without it, it would have been very difficult to and much more time consuming to generate results with the same statistical merit.

TABLE OF CONTENTS

ACKNOWLEDGMENTS iii

LIST OF TABLES vii

LIST OF FIGURES viii

SUMMARY xi

1 INTRODUCTION 1

2 BACKGROUND 6

2.1 IRIS Reactor 6

2.2 Concrete Boration 8

2.3 Cross-sections 10

3 METHOD 12

3.1 Monte Carlo 12

3.2 Variance Reduction 13

3.3 CADIS and FW-CADIS 13

3.4 Monaco 15

3.5 MAVRIC 15

4 MODEL DEVELOPMENT 17

4.1 Core Description 17

4.2 Homogenization of the core 21

4.3 Reflector 24

4.4 Core Barrel 25

4.5 Steam generators 27

4.5.1 Steam Generator Body 27
4.5.2 Steam Generator Headers 30
4.5.3 Steam Generator Support 31
4.6 Pressure Vessel 31
4.7 Containment Vessel 33
4.8 Reactor Building 35
4.9 Model Geometry Structure 37
4.10 Temperature profile of the pressure vessel 38
4.11 Other Model Options 39
4.11.1 Response Functions 39
4.11.2 Grid Geometries 39
4.11.3 Source 40
4.11.4 MAVRIC Options 41
4.12 Materials used 42
5 IRIS MODEL VERIFICATION AND VALIDATION 43
5.1 Geometry verification by model “flooding” 43
5.2 Verification of the overall variance reduction procedure functionality 45
5.3 Validation 53
5.3.1 MCNPX Comparison 53
5.3.2 TORT Comparison 55
5.3.3 Discussion 56
6 ANALYSIS OF CONCRETE ACTIVATION IN THE IRIS REACTOR VESSEL CAVITY 57
6.1 Model Features and Options Used in Analysis 57

6.2 Activation Response 60

6.3 Baseline Results with “standard” (unborated) concrete..... 61

6.4 Results with boration 70

7 CONCLUSIONS..... 77

8 FUTURE WORK..... 81

APPENDIX A: IAEA Data..... 83

APPENDIX B: Activation Cross-Sections 87

REFERENCES 93

LIST OF TABLES

Table 1: Fuel pin dimensions 20

Table 2: Guide tube dimensions 21

Table 3: Core homogenization parameters 22

Table 4: Steam generator sections for the model 29

Table 5: Pressure vessel major dimensions 32

Table 6: Materials in the model 42

Table 7: CPU times for the fast flux calculations 51

Table 8: Comparing the values of the MAVRIC and MCNPX Models 54

Table 9: Comparing the flux values of the MAVRIC and TORT Models 56

Table 10: Isotopes of interest 59

Table 11: Response weights 59

Table 12: Impurities of interest assumed in concrete 60

Table 13: List of several points and responses 75

Table 14: Maximum impurity content resulting in activation still below clearance limit 79

Table A.1: Values of Activity Concentration for Radionuclides of Artificial Origin in Bulk 84

Table B.1: List of microscopic cross sections used for activation 87

LIST OF FIGURES

Figure 1: IRIS Reactor Building 7

Figure 2: $^{59}Co(n,\gamma)^{60}Co$ cross-sections 11

Figure 3: $^{151}Eu(n, \gamma)^{152}Eu$ cross-sections 11

Figure 4: $^{153}Eu(n, \gamma)^{154}Eu$ cross-sections 11

Figure 5: Assembly layout in core 18

Figure 6: Assembly layout 18

Figure 7: Fuel pin cross section 20

Figure 8: Guide and instrumentation tube cross section 20

Figure 9: Upper half of the homogenized assembly description 23

Figure 10: Lower half of the homogenized assembly description 23

Figure 11: Reflector, ¾ view without the core 24

Figure 12: Barrel with reflector and core 25

Figure 13: Bottom plate (dimensions in mm) 26

Figure 14: Ring shown with the core, reflector, barrel, bottom plate, and pressure vessel 27

Figure 15: Density change throughout the steam generators 28

Figure 16: Steam generator 29

Figure 17: One half of the steam generator header 30

Figure 18: Steam generator support structure 31

Figure 19: IRIS pressure vessel in containment with all modeled internals 32

Figure 20: Feedwater nozzle model cutaway view 33

Figure 21: Containment 34

Figure 22: Concrete in containment 35

Figure 23: Whole reactor building 36

Figure 24: Hierarchal tree diagram of the model 37

Figure 25: Temperature profile superimposed on the pressure vessel 38

Figure 26: Materials as computed with a 100^3 mesh 40

Figure 27: Pressure and containment vessel flood 44

Figure 28: Forward deterministic estimate 46

Figure 29: Fast flux adjoint estimate 47

Figure 30: Fast flux importance map for neutron group 1 48

Figure 31: Consistent-biased source for the fast flux verification 49

Figure 32: Fast flux Monte Carlo results 50

Figure 33: Relative uncertainty for Figure 32 50

Figure 34: Fast flux for 20 times more histories 52

Figure 35: Relative uncertainty for Figure 34 52

Figure 36: MCNPX model showing locations of tallies for comparison 54

Figure 37: Location of maximum flux in the TORT model 55

Figure 38: Comparing the MAVRIC model to TORT 56

Figure 39: Mesh and geometry used for results 58

Figure 40: Total flux with no boron 62

Figure 41: Relative uncertainty for Figure 40 62

Figure 42: ^{60}Co response 63

Figure 43: Relative uncertainty for Figure 42 64

Figure 44: ^{60}Co response above the IAEA clearance 64

Figure 45: ^{60}Co response above IAEA clearance limit with applied safety factor 65

Figure 46: Total ^{152}Eu response with no boron 66

Figure 47: ^{152}Eu response above the IAEA clearance (no boron) 67

Figure 48: ^{152}Eu response above the clearance with the safety factor (no boron) 67

Figure 49: Total ^{154}Eu response with no boron 68

Figure 50: ^{154}Eu response above the IAEA clearance 69

Figure 51: ^{154}Eu response above the clearance with the safety factor (no boron) 69

Figure 52: Total flux with boron 70

Figure 53: Relative uncertainty for Figure 52 71

Figure 54: Total ^{60}Co response with boron 72

Figure 55: ^{60}Co response above the IAEA clearance with boron 72

Figure 56: ^{60}Co response above the IAEA clearance with boron and safety factor 73

Figure 57: Total ^{152}Eu response 73

Figure 58: ^{152}Eu response above the IAEA clearance with boron 74

Figure 59: ^{152}Eu response above the IAEA clearance with safety factor and boron 74

Figure 60: Activation by depth 76

SUMMARY

This thesis analyzes the concrete activation within the pressure vessel cavity in the IRIS nuclear power plant design from Westinghouse. This new integral reactor design with a proposed 335 MW_e output has potential to minimize activation due to the large reactor pressure vessel with a wide downcomer, required by an integral reactor configuration. The downcomer coupled with a reflector for neutron economy reduces activation of materials outside the reactor vessel. The reactor cavity concrete wall is still activated to a level above the limit of IAEA clearance for free release of the concrete after decommissioning. The objective of this work was to investigate whether borating the concrete could reduce the activation below the free release limit.

Modeling of the reactor is done using the MAVRIC sequence in the SCALE code. This sequence is an implementation of the CADIS method (by J.C. Wagner and A. Haghighat) and FW-CADIS method (by J.C. Wagner and D. Peplow) designed to automate variance reduction for deep shielding problems.

Results of the simulations are presented with and without borating the concrete, a common method for reducing activation in materials because of ^{10}B large thermal capture cross section. The results are based on the (n,γ) reaction of three isotopes identified as being the main drivers of activation in the concrete: ^{59}Co, ^{151}Eu and ^{153}Eu.

The activation was found to be manageable. With boration, all of the activation products considered, ^{60}Co, ^{152}Eu, and ^{154}Eu, were found to be below the free release limit after applying a safety factor.

CHAPTER 1

INTRODUCTION

The challenge when designing a new nuclear power plant (NPP) is to be better than other offered designs and competitive with non-nuclear power plants. The ultimate goal for the designer is seeing the utility select the design, construct the plant and have it operate as intended. There is no advantage to the design if it offers nothing to the utility versus the currently operating plants. IRIS attempts to reduce the total installed cost per kilowatt as well as the total cost of ownership. This thesis addresses two large costs for the utility: collective dose for the operators and decommissioning.

The first large cost to any nuclear facility is radiation dose monitoring. All plant employees and maintenance crew must wear radiation badges and strict tallies of doses are kept. If a worker exceeds the annual dose limit, then they become another cost for the utility as they can no longer perform their normal duties for the remainder of that year.[1] The ultimate goal of IRIS would be to have all open areas of the plant accessible with negligible radiation levels. Here reduction of the activated materials would also reduce the overall dose during maintenance significantly.

Decommissioning any power facility is a great challenge and expense.[33] In addition to all the legal requirements that must be met, there is the cost of ultimate disposal of material that is activated above the free release limit. This cost could be as much as 1000 times what it would

be to dispose of material under the free release limit.[30] Even with the US NPP fleet receiving 20 year license extensions, every plant site will eventually need to be returned to a green field.[1]

The IRIS Reactor is a new integral pressurized water reactor (PWR) design that offers improved safety though its "safety-by-design" approach and deploys integral steam generators.[7] Its design power is 335 MWe and design life is greater than sixty years. IRIS was identified as a grid-appropriate reactor design and is targeted towards electrical utilities and countries where a 1000 MWe plant would be too large for the local power grid or too costly to finance.[9] It has a unique potential to reduce both the dose in operation from the core as well as the dose during maintenance from activated materials, most notably cobalt (in steel) and europium (in concrete). The integral pressure vessel provides a 1.6 meter wide/thick downcomer with downward flowing coolant that has exited the integral steam generators and through the lower plenum will return to be reheated by the core. This downcomer reduces the flux at the pressure vessel about six orders of magnitude versus a currently operating loop PWR where the downcomer is normally only about 20 cm. Based on work at ENEA (Italy), this flux level has been identified as just around the level where with minor modifications to the containment vessel design, there could be very little to no activated material beyond the pressure vessel boundary.[5] The objective of this research is to quantify the activation and make recommendations about reducing it below the fee release limit.[27]

Such analysis requires accurate shielding calculations, and the Monte Carlo method is the method of choice to analyze complex three dimensional geometries. One of the biggest hurdles to any Monte Carlo deep penetration shielding analysis is with so many orders of magnitude reduction in the flux, it is very difficult and time intensive to create a model that will give reasonable results and statistical uncertainty in acceptable time. This stems from the fact that the

standard deviation is inversely proportional to the square root of the number of histories. To reduce the relative error n times requires that one runs n^2 as many histories as before. As an example, to reduce the uncertainty from 10% to 1% requires 100 times more histories. For a large and complex geometry such as IRIS, it would require processor-years in the straightforward, analog mode of Monte Carlo simulation, and effective variance reduction is necessary.

IRIS provides a perfect test bed for the hybrid methodology approach that is employed in the Standard Computational Analysis for Licensing Evaluation (SCALE) 6.0 package called Monaco with Automated Variance Reduction using Importance Calculations (MAVRIC).[34] MAVRIC automates the process of variance reduction. It biases the pure analog problem in a way that generates results more quickly in the area of interest. Instead of the skilled modeler spending time traversing through trial-and-error iterations where importances for individual areas must be tuned to get the best results, MAVRIC will use an automated approach that is transparent to the user.

MAVRIC works by combining the two methods of solving any shielding problem: deterministic and stochastic approach. By using the deterministic functions to generate the weight windows for the stochastic portion of the simulation, the problem can be speed up orders of magnitude, which have been demonstrated on large realistic problems.[36] MAVRIC approach is based on the consistent adjoint driven importance sampling (CADIS) method which is a technique using the adjoint to develop weight windows and consistent source biasing. It is extended with forward-weighted CADIS (FW-CADIS), where the CADIS portion is weighted with the expected forward flux so that multiple tallies can achieve the same relative uncertainty in approximately the same amount of computational time. Both the forward and adjoint

calculations are performed using the discrete ordinates code Denovo. Then the importance map generated by the FW-CADIS method is passed to the Monte Carlo code Monaco for the final portion of the simulation.

Applying MAVRIC to IRIS serves as a great way to test the code and the method, while generating real results that can become part of the next IRIS engineering iteration. A "real" problem, such as IRIS, provides a better test than any conceived problem. With MAVRIC, the fluxes in the concrete support annulus will be analyzed to determine the flux distribution and its energy spectrum. This data will be used to make a determination about the activation of the two isotopes that have been identified as the most troublesome: ^{59}Co and ^{151}Eu. Those two isotopes have a large thermal neutron capture cross section resulting in ^{60}Co and ^{152}Eu. Both are gamma emitters. Thus the goal will be to determine the flux leaving the core and how it is thermalized in the liner and concrete. Based on the previous work at ENEA[5], these are the only isotopes that need to be addressed. Moreover, this study will evaluate whether borated concrete can be used to reduce the overall activation of the concrete pushing it below the regulatory limit, and what is the impact on the overall flux in the reactor building and the control room that is relatively close to the core?

The following sections will attempt to answer that question. An in depth literature review focusing on the regulatory limits and the work that has been done with borated concrete both in neutron shielding and considerations to its strength is presented in chapter two. Chapter three describes the methodology and software used. Chapter four contains a full model description with assumptions and justifications included. Chapter five will compare the model developed in this thesis to two other models of IRIS for validation as well as verification work. The results of the simulations will be analyzed in chapter six and appropriate recommendations made including

suggestions for further work. Additional specific information will be included in the appendix for reference.

CHAPTER 2

BACKGROUND

2.1 IRIS Reactor

IRIS is an integral type PWR producing 335 MW_e.[8, 9] It is being developed with Westinghouse as the leader of a multinational team of industry and academia. The purpose of the reactor is to fill the need of a smaller developed, developing nation, or smaller utility that is looking for energy independence but does not have the grid or the financial resources to support a gigawatt plant. The integral design means all of the primary systems are contained inside the reactor pressure vessel including the control rod drives, minimizing the number of pressure vessel penetrations. It has the added bonus of eliminating all but one of the Class IV accidents, scenarios with the potential for radiological release. IRIS is designed with passive safety systems as well.[44]

The design of the IRIS nuclear power plant includes enough change from the currently operating fleet that it needs some special considerations. The entire reactor portion of the plant is contained within a single building. This reactor building would house containment as well as the control room and associated office space necessary to operate the plant. With people within 15 meters of the core, accurate analysis of the all activated materials is necessary. The goal in reducing the activated materials also allows an increase in the accessible areas of the plant and eliminates concern that maintenance personal would exceed their annual dose.

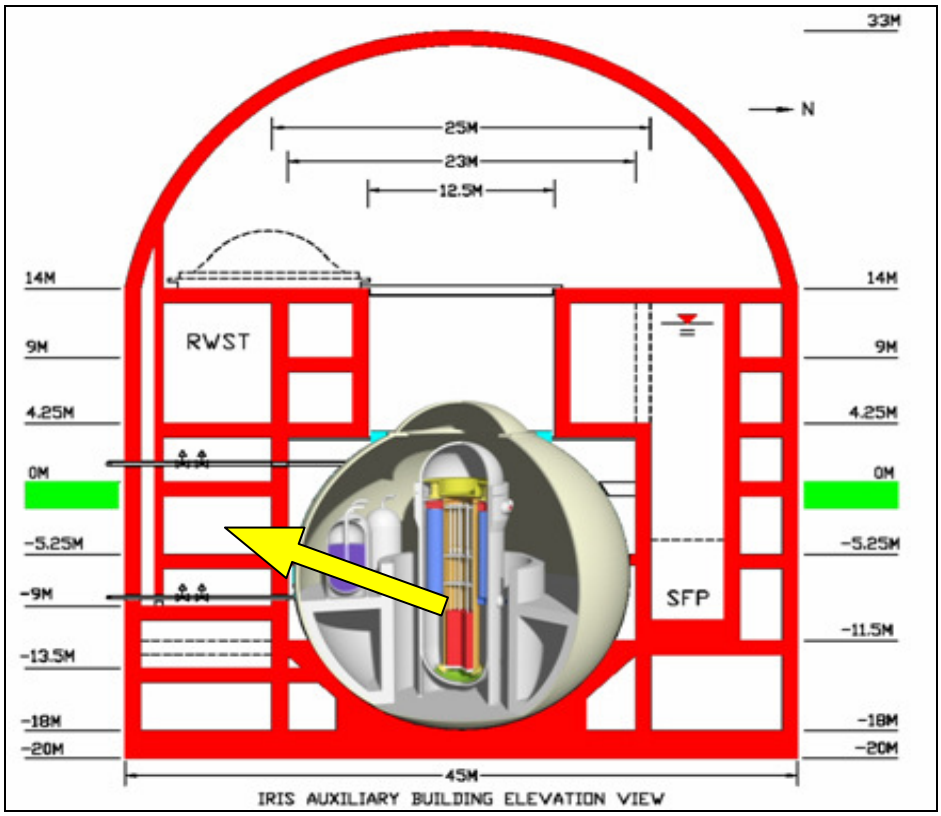

Figure 1: IRIS Reactor Building

In Figure 1, the yellow arrow from the core points to the level and approximate location of the control room. With an aggressive goal of the room dose rate being at the general public level, it is very important to have an accurate activation map of the entire containment vessel.

As briefly mentioned before, there are several components to the IRIS pressure vessel that make these aggressive goals possible. The downcomer size discussed in the introduction is one of the largest contributors to the reduced flux at the pressure vessel boundary. The water is an excellent moderator which slows and attenuates the fast flux leaving the core.

IRIS also has a neutron reflector composed of 90% stainless steel and 10% water. This reflector increases the overall neutron economy and reduces flux at the pressure vessel boundary.

2.2 Concrete Boration

The addition of boron to concrete is done in an attempt to capture neutrons that would otherwise lead to activated material and delayed gammas. The fast flux reaching the concrete walls in the reactor vessel cavity will enter the concrete at which point the water from the pouring process and other constituents will thermalize the neutrons and result in their ultimate absorption potentially generating activated materials.[28] The $^{10}B(n,\alpha)^{7}Li$ reaction is an excellent way to capture neutrons without creating such activation. Alpha particles are easy to shield and boron is widely available.

There has been extensive work done in the area of concrete boration particularly when it comes to the strength of the concrete. There are two ways to borate concrete: it can be added as borogypsum to the aggregate or boric acid in the water. Addition of boron to the aggregate can come from major borogypsum producers like Turkey or fly ash from coal fired power plants.

Boration of shielding materials in nuclear applications is not new. Henrie investigated the economics of boron as an additive to different concrete compositions for neutron shielding. He also investigated iron as an aggregate for the gammas that activated material in the concrete would emit in small research reactors (50 kW). He found that it was most advantageous to add approximately 0.5 wt. % of boron.[25]

More modern investigations have centered on the need to shield neutrons in fusion reactors. The (d,d) reactions between deuterons generates neutrons with an average energy of 2.46 MeV. This is comparable to fast neutrons leaving the pressure vessel. A factor of thirty reduction was found when the walls of the Wendelstein-7-X hall were doped with 700 ppm boron.[26]

The ITER Fusion Reactor also has been analyzed from this aspect. For 0.1 $^{g}/_{cm^3}$ of boron added to the surface layer of concrete, dose rate factors were reduced immediately by 2-3 times.[29] Work on the JT-60 shielding with borated concrete in the B_4C form, found 40% dose rate reduction.[32]

Yarar has completed some work calculating the effectiveness of the addition of colemanite, a boron bearing mineral.[46] The colemanite concrete composition used contained about 1.3 wt. % boron. The results noted that even for very short irradiation, the colemanite concrete would be considered "high level waste," but that it decays rapidly.[45] This would indicate that the long lived troublesome isotopes in the concrete that this thesis attempts to address would be low enough to make the concrete waste a lower level.

However, the addition of boron materials alters strength properties. Erdogan et. al. looked at the strength differences due to borogypsum additives to cement and found some weakening. B_2O_3 was present in concentrations up to 11.25% in the borogypsum. There was 4% borogypsum added to the test sample versus the control which had none. They did note in the conclusion that the elimination of B_2O_3 improves the strength values.[20]

The effect of boric acid sludge containing borogypsum on the properties of cement was also investigated. Compressive strength was the metric. The conclusion was that up to 4% of the boron sludge may be added but that did produce a 90 day compressive strength drop of 65%.[12]

Work done in Japan by Kinno et. al. showed the results of careful selection of the aggregate to eliminate cobalt and europium as well as adding boron in a concentration up to 0.6% by weight. They manufactured various levels of low activation concrete from 1/10 to 1/300 reduction of impurities and found that with the boron, the activation was reduced by 300 to

10000 times respectively. Their recommendation was that low activation concrete be chosen for advanced reactors.[30] Hayashi et. al. created a precise estimation of both the thermal neutron flux with the activation cross section creating a new group-wise cross-section library.[24]

The results of previous work indicate that up to 1% boron by weight in the concrete is an acceptable value. Consideration of the concrete strength with the boron is beyond the scope of this thesis.

2.3 Cross-sections

All the codes used in this analysis were multi-group codes. The library used was based on the Evaluated Nuclear Data File (ENDF/B-VII.0).[10] It was a coupled 27 group neutron and a 19 group gamma library. For all the simulations in this thesis, the gamma portion of the library was not considered.

Activation cross-sections were based on the 200 neutron groups of the ENDF/B-VII.0 library. MAVRIC has the capability of using any set of cross-sections as a response to cross-section codes in SCALE. They are then folded appropriately to work with the cross-section library structure selected for the simulation. The three isotopes considered for this thesis were ^{59}Co, ^{151}Eu, and ^{153}Eu since they have been identified in the previous studies as responsible for the large portion of the activation. The response was based on their (n,γ) reaction, that is the probability that each of those isotopes captures a neutron and releases a gamma and is transmuted into a radioactive isotope. A table listing the values is included in Appendix B.

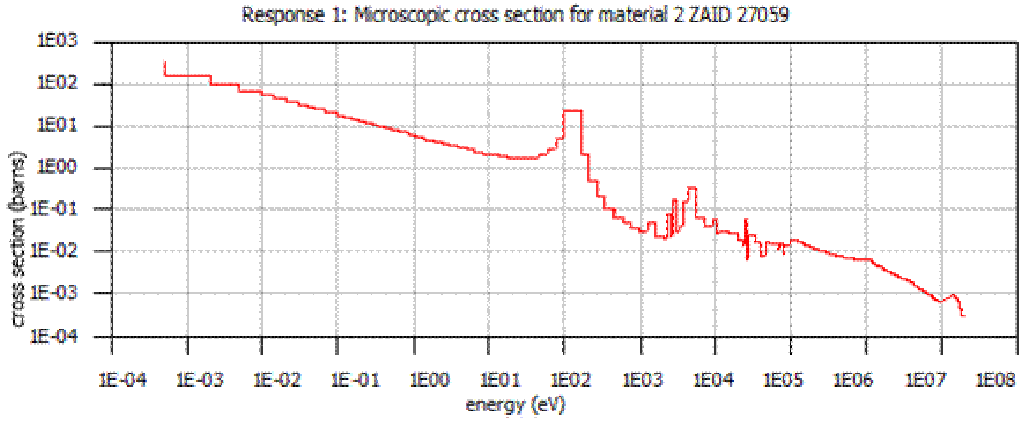

Figure 2: $^{59}Co(n,\gamma)^{60}Co$ cross-sections

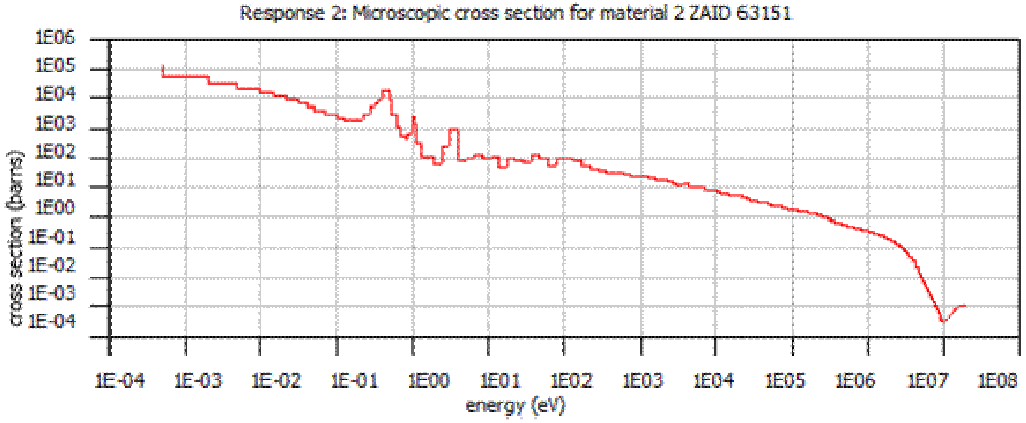

Figure 3: $^{151}Eu(n, \gamma)^{152}Eu$ cross-sections

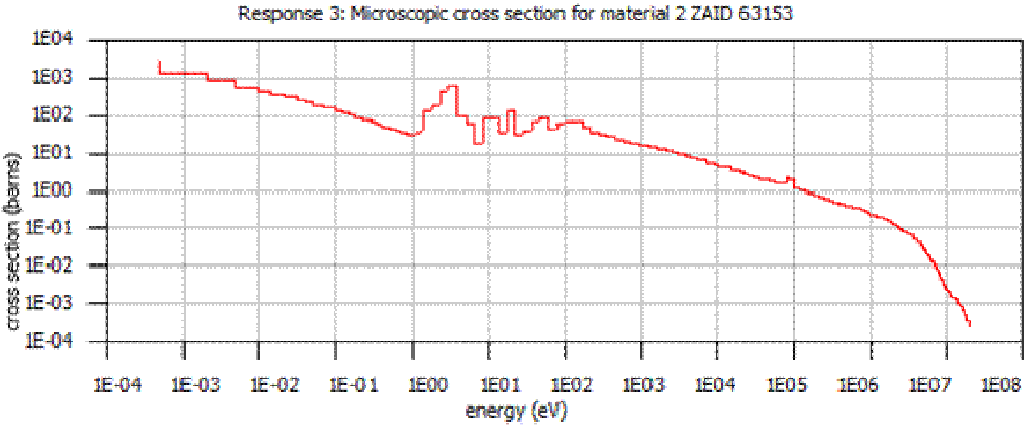

Figure 4: $^{153}Eu(n, \gamma)^{154}Eu$ cross-sections

CHAPTER 3

METHOD

3.1 Monte Carlo

Transport of neutral particles, neutrons and photons, is described by the transport equation:

$$\frac{\partial n}{\partial t} + v\hat{\Omega} \cdot \nabla n + v\Sigma_t n(\vec{\boldsymbol{r}}, E, \hat{\Omega}, t)$$

$$= \int_{4\pi} d\hat{\Omega}' \int_0^{\infty} dE' v'\Sigma_s \left(E' \to E, \hat{\Omega}' \to \hat{\Omega}\right) n\left(\vec{\boldsymbol{r}}, E', \hat{\Omega}', t\right) + s(\vec{\boldsymbol{r}}, E, \hat{\Omega}, t) \quad (1)$$

where $n\left(\vec{\boldsymbol{r}}, E', \hat{\Omega}', t\right)$ is the neutron flux and other terms describe source, inscattering, leakage, streaming, and scattering collision loss within an arbitrary volume. The neutron flux is dependent on seven independent variables: $\boldsymbol{r} = x, y, z$; E; $\hat{\Omega} = \theta, \phi$; and t. Numerical solution of the transport equation is possible by discretizing the phase space, also known as the deterministic approach. The Monte Carlo method instead attempts to solve the problem by simulating histories through an accurate representation of the geometry and the physics of the problem. These histories are tracked throughout the problem phase-space until some specified parameter is met at which time they are killed and their statistical contribution to the total is tallied weighted by other parameters that are user set. Monte Carlo simulations can be likened to solving the integral of an equation using a shotgun; individual shot either falls above or below the line. If the bounds are known, and the number of shot is tallied above and below the line, the integral

can be easily computed. The primary advantage to this method is that complicated problems can be simulated accurately. It is also easily parallelizable. The primary disadvantage is the time required to simulate complex shielding problems like IRIS. There are so many orders of attenuation in the system that without any statistical biasing, it would take thousands of processor-years to generate enough histories that have statistical merit in the areas of interest.

3.2 Variance Reduction

Fortunately, there are methods of biasing that are fair; they preserve the estimated mean, while accelerating variance reduction in the areas of interest at the expense of other areas that are not important for a particular objective. A complete overview is presented in the paper by Haghighat and Wagner.[23] The basic approach is splitting histories (particles) as they move through the system. As this is done, the weight of the history is accordingly reduced. This increases the number of histories as well as preserving the weight. The difficultly with this biasing is how to and where to split. These importance parameters take experience and iterations to generate manually.

3.3 CADIS and FW-CADIS

The Consistent Adjoint Drive Importance Sampling (CADIS) and the Forward Weighted CADIS (FW-CADIS) methods developed by Wagner and Haghighat, and Wagner and Peplow, respectively, are attempts to improve the Monte Carlo method efficiency using estimates of the adjoint and forward fluxes that are calculated deterministically.[39, 40] These methods are based on the classical source-detector problem. The following is a summary of their work.

In CADIS, one considers a classical source-detector problem with a unit source with emission probability distribution function $q(\vec{r}, E)$ and a detector response function $\sigma_d(\vec{r}, E)$. To

determine the total detector response, R, the forward scalar flux, $\varphi(\vec{r}, E)$, must be known. The response is found by integrating the product of the detector response function and the flux over the detector volume, V_D.

$$R = \iint_{E,V_D} \sigma_d(\vec{r}, E)\, \varphi(\vec{r}, E) dV\, dE \tag{2}$$

Wagner showed that using the (approximate) adjoint, the optimum variance reduction parameters (importance and a consistent biased source distribution) for Monte Carlo simulation are given by:

$$\hat{q}(\vec{r}, E) = \frac{1}{R} q(\vec{r}, E)\, \varphi^{+}(\vec{r}, E) \tag{3}$$

where the weight window targets for particle transport would be:

$$\overline{w}(\vec{r}, E) = \frac{R}{\varphi^{+}(\vec{r}, E)}. \tag{4}$$

This minimizes the variance in the forward Monte Carlo simulation to calculate R. When the particle is sampled from the biased source, the weight must be adjusted to preserve the fair game. This is the origin of the consistency of the CADIS method. Source particle histories must begin with a weight that matches the window in the phase-space point that they begin. For example, the center of the core is much less important to the activation of the concrete outside the reactor vessel than the core periphery. This means that the source particles here are born with appropriate weight minimizing the computation that must be expended on their life. This greatly increases the computational efficiency of the method.[37]

FW-CADIS expands on this method by weighting the adjoint source by the inverse of the expected forward flux. This expansion allows the method to effectively minimize the variance of multiple source-detector problems in the same simulation. The benefit to the user is the

availability of mesh tallies for a potentially large area of interest.[39] If the user wanted a detector response, $\sigma_d(\vec{r}, E)$, over the whole mesh tally, then the adjoint source would be:

$$q^+(\vec{r}, E) = \frac{\sigma_d(\vec{r},E)}{\int \varphi(\vec{r},E)\sigma_d(\vec{r},E)dE} \quad (5)$$

where $\varphi(\vec{r}, E)$ is an estimate of the forward flux over that mesh tally.

FW-CADIS attempts to keep the variance, of the Monte Carlo calculation constant, i.e., the variance of the meshes more uniform.

3.4 Monaco

Monaco is a multi-group Monte Carlo code that takes the importance map generated from the adjoint and forward estimates and calculates the biased portion of the simulation.[13] It can tally based on points, regions, or meshes. Monaco can weight tallies with built-in or user-specified responses. Any dose-like response is just the sum over groups of the flux of a particular group times the response function of group. For the interactions of interest, this makes calculating the reaction rate much easier.[38]

3.5 MAVRIC

MAVRIC is the sequence implementing the CADIS and FW-CADIS methods in the SCALE6 package from Oak Ridge National Laboratory (ORNL).[37] The Denovo code is the basis for all deterministic calculations used to generate variance reduction parameters. Denovo calculates both the adjoint estimate and weights it with the forward flux estimate if necessary. MAVRIC takes the user input, converts it to the appropriate format and passes it where it is needed during the run. Since there are multiple codes involved, MAVRIC will convert as required from one code to the other. It also has the ability to stop at intermediate points for the user to investigate the output before continuing. This setup allows Denovo and Monaco to be

fully functioning independent codes that can be utilized anywhere as well as within the CADIS and FW-CADIS methods for deep penetration shielding problems.

CHAPTER 4

MODEL DEVELOPMENT

The majority of the development of the IRIS model was spent in accurately describing the geometry of the building and containment using the SCALE General Geometry Package (SGGP). SGGP is designed to be simple to use with emphasis on fast development. The user has several macrobodies available to help simplify the modeling of complex geometries. Another feature of SGGP is the unit and hole system. Units are wholly defined objects each with their own bodies in any configuration that can be inserted into holes placed in other units. The global unit of the system is the entire universe of the simulation; nothing in the problem can exist outside the global unit. This feature is useful because it allows the user to model the pressure vessel as a unit and then insert it into the containment vessel. If there are any changes to be made, or the user wants to just analyze the pressure vessel, it is very easy to make the changes or set it as the global unit for a simulation. This section will describe the entirety of the model geometry as well as the other assumptions made. There will also be a section describing model validation.

4.1 Core Description

The IRIS core is composed of 89 17x17 XL Westinghouse fuel assemblies. (Figure 5)

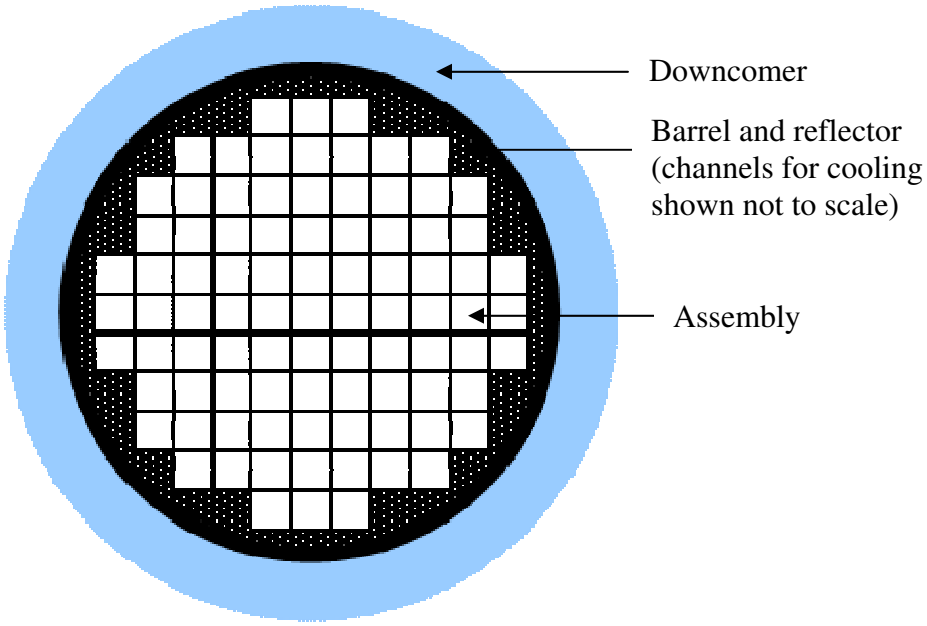

Figure 5: Assembly layout in core

Each assembly has 289 positions: 264 for fuel pins, 24 for control, and one for instrumentation shown in Figure 6.

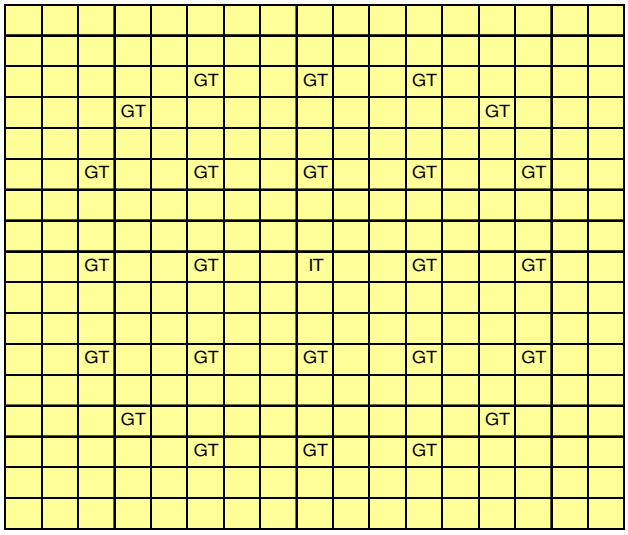

Figure 6: Assembly layout

One of the assumptions made about the fuel assemblies early in the project is that it is unnecessary to model them exactly as they would appear in the reactor core. There are many

small details that make a negligible difference to the shielding analysis. However, the outer dimensions and the locations of the support structures are reasonably well known. As such, it is possible to slice the core along different axial planes and create homogenizations of each zone. The semi-homogenization captures all the material details of the zones but simplifies the model and makes it more manageable. Westinghouse provided a table with a breakdown of the assembly into the semi-homogenous zones.[21] Each zone included an axial dimension with a volume fraction of materials in that zone. With this basis, there were several assumptions made about the assemblies before the homogenization processes began.

All assemblies are assumed to be identical. The most important assumption here is with respect to the ^{235}U enrichment percentage. For a real core, the fuel designer may decide that varying the enrichment could produce better fuel performance. However, for this purely shielding problem, it was assumed that all fuel was 4.95% ^{235}U by weight. It was also assumed that the fuel was completely UO_2; it was fresh from the supplier with no fission products. The uranium in the homogenized core was assumed to be at the theoretical density of UO_2 multiplied by a density correction factor times a volume factor. The density factor of .96 takes into account the inability of the fuel fabricator to sinter the pellets to the theoretical density. The volume factor of .99 accounts for the dishing and chamfering of the fuel pellet in order to relieve thermal stress. This assumed density was 10.4 g cm^{-3}. All pins and guide tubes were assumed to be exactly the same. Dimensions for them quoted no tolerances. Assemblies were modeled at the cold dimension. The assembly pitch is 8.466 in; however, the actual cold size of the assembly is 8.426 in. The extra space was modeled as water at the core water temperature to fill the volume completely.

Fuel pins in the IRIS core were assumed to correspond to the fuel pins in the 17x17 XL Westinghouse assembly. Each fuel pin (Figure 7) is composed of a long cylindrical Zircaloy tube full of uranium pellets and backfilled with helium gas at an elevated pressure to prevent buckling in operation. The active core zone, UO_2 pellets stacked height, is 168 in while the total fuel pin height is 194 in. The extra space is for the upper and lower plena, used for expansion of the fuel and for fission gas capture and the endplugs.

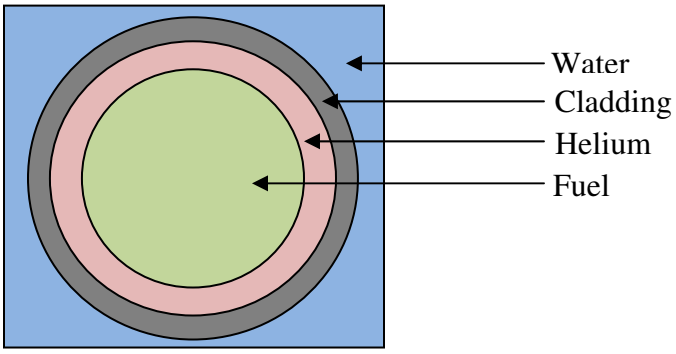

Figure 7: Fuel pin cross section

Each fuel pin has the following dimensions[43]:

Table 1: Fuel pin dimensions

Component	Dimensions (in)
Fuel pellet diameter	0.3225
Fuel rod outside diameter	0.374
Fuel rod clad thickness	0.0225
Lattice pitch	0.496

The guide tubes and the instrumentation tubes were assumed to be the same. (Figure 8)

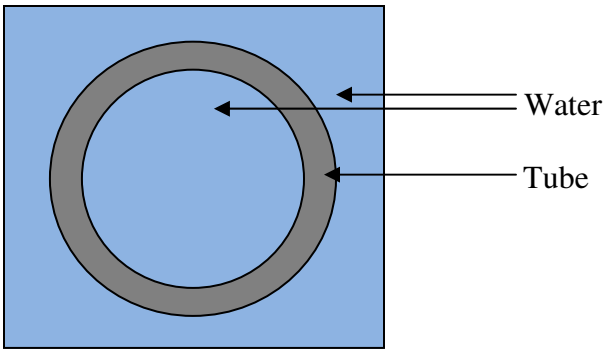

Figure 8: Guide and instrumentation tube cross section

Dimensions for the guide and instrumentation tubes[43]:

Table 2: Guide tube dimensions

Component	Dimensions (in)
Outer diameter	0.482
Inner diameter	0.442
Lattice pitch	0.496

All the water throughout the core was assumed to be 0.74 g cm^{-3}. This includes the water between the assemblies, between the pins and tubes in the assemblies and within the tubes. There was no boron added to the water in the core in the model.

4.2 Homogenization of the core

As previously mentioned, Westinghouse provided general locations and materials for different sections of the assemblies. This along with the core assumptions that make up the active zone was homogenized as follows.

Each zone was homogenized the same way. The goal was to preserve the same mass as the real assembly setup as well as the dimensions of the core. Each axial zone height was multiplied by the cold axial cross sectional area to establish the volume of the zone. For the zones with more than one compound, there was a corresponding volume fraction given. KENO geometry requires a weight percent for user created compositions. To calculate this weight percent for each zone the following equation was used:

$$WTPT_{isotope,compound,zone} = \frac{(V_{zone})(V_{f,compound,zone})(\rho_{compound})\left(wtpt_{isotope,compound}\right)}{m_{zone}} \quad (6)$$

where V_{zone} is the total zone volume, $V_{f,compound,zone}$ is the volume fraction of the specified composition in the zone, $\rho_{compound}$ is the cold density of the composition, and m_{zone} is the total mass of all the compounds in the zone. Then this weight percent for each compound needed to be decomposed into a weight percent by element or isotope depending on the availability of the

cross-section, $wtpt_{isotope,compound}$. The end result is a table of isotopes with a corresponding weight percent by zone.

The results of the fuel assembly homogenization are 16 zones that appear as a set of stacked cuboids with dimensions corresponding to the cold assembly. (Figure 9 and Figure 10)

Table 3: Core homogenization parameters

	Water	Zr-4	SS-304	Inconel	Description	Thickness (in)
8T	1.000	-	-	-	Hold Down Spring	1.000
7T	0.852	-	0.148	-	Top Nozzle Enclosure	3.625
6T	0.549	-	0.451	-	Top Nozzle Adapter Plate	0.680
5T	0.990	0.010	-	-	Gap	1.695
4T	0.660	0.340	-	-	End Plug	1.000
3T	0.585	0.102	0.037	-	Upper Plenum	0.993
2T	0.520	0.102	0.037	0.066	Top Grid in Upper Plenum	0.152
1T	0.585	0.102	0.037	-	Upper Plenum	5.487
Active Core						
1B	0.895	-	0.105	-	Bottom Nozzle Enclosure	1.823
2B	0.332	-	0.678	-	Bottom Nozzle Adapter Plate	0.685
3B	0.660	0.340	-	-	End Plug	1.000
4B	0.532	0.171	-	0.053	Lower Plenum and Grid	0.690
5B	0.585	0.171	-	-	Lower Plenum	2.714
6B	0.516	0.171	-	-	Lower Plenum and Bottom Grid	1.520
7B	0.585	0.171	-	-	Lower Plenum	1.568

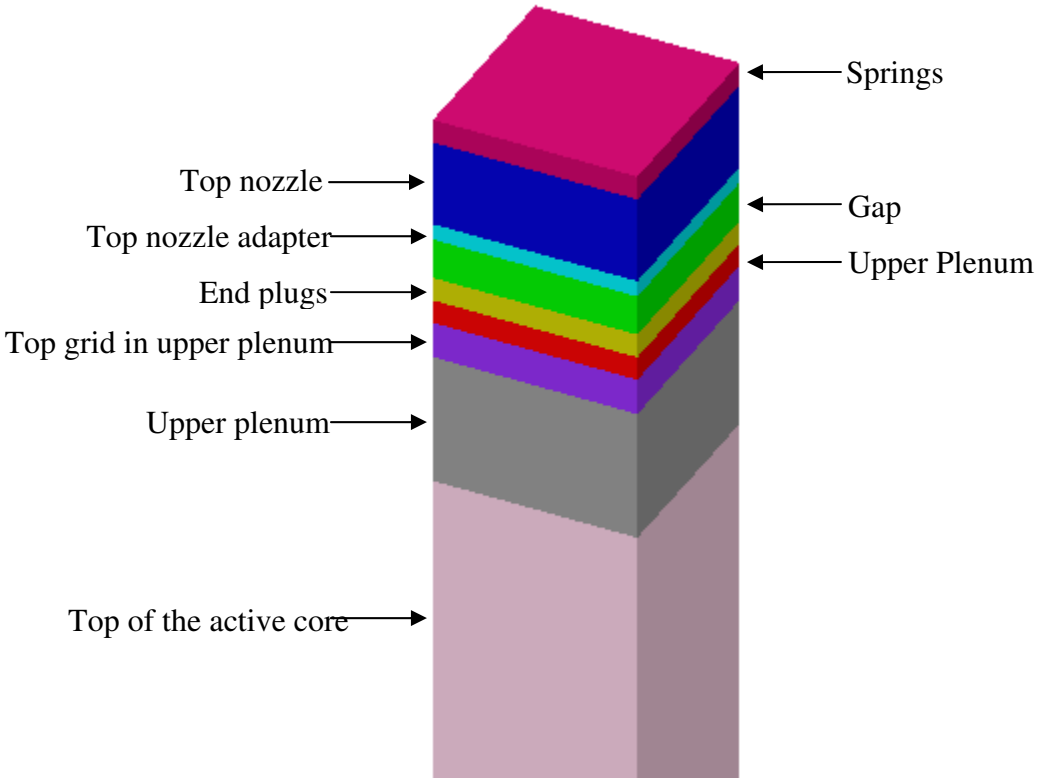

Figure 9: Upper half of the homogenized assembly description

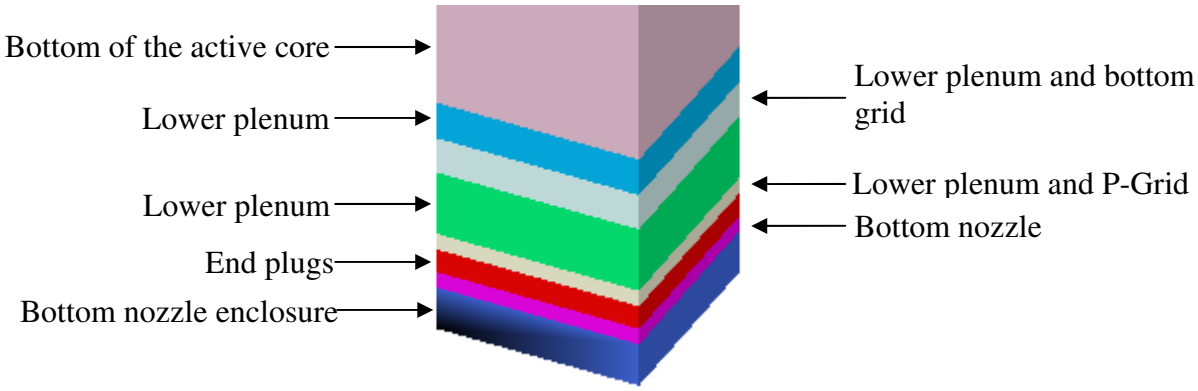

Figure 10: Lower half of the homogenized assembly description

4.3 Reflector

The reflector (Figure 11) is a larger steel component placed just outside the core that is designed to improve neutron economy by reflecting fast and epithermal neutrons back into the core. It is 90% 316L stainless steel and 10% water channels. It was modeled as a homogenous piece when in reality, it would have more channels nearer the core for cooling due the gamma heating while farther away, there would be fewer.

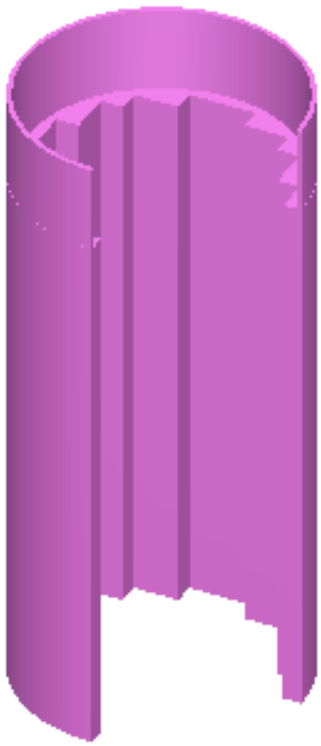

Figure 11: Reflector, ¾ view without the core

The reflector can roughly be described as a six meter tall annulus with a 136 cm outer radius with an inner cutout corresponding to the core cross sectional profile. The cutout extends 518 cm from the bottom of the core. The upper 82 cm has an inner radius of 131 cm.[18]

4.4 Core Barrel

The barrel's (Figure 12) primary function in the pressure vessel is to create the primary loop. It is a 16 m tall annulus, 137.5 cm inner radius and 142.5 outer radius, resting on eight azimuthal supports connected to the pressure vessel.[16]

Figure 12: Barrel with reflector and core

There are a few differences between the barrel in the model and what would be the case in the IRIS pressure vessel. The barrel is actually composed of two separate annuli, one on top of the other. There are some flanges where connections between the two would be; these are removed because they are insignificant to the shielding of the whole system. There also would be several

sets of eight holes at different levels in the barrel. The primary function of these holes would be to establish a natural convection loop in the event of pump failure or primary coolant loss that drops the level of the primary below the pump intakes. Again, they are completely inconsequential to the shielding.

There are two other components that are part of the barrel. First, the bottom plate (Figure 13) is a section of stainless steel that is used to support the core and is part of the barrel. For each assembly position there is a set of four holes that provide primary water flow to be heated by the core. They are all modeled exactly as described.[17] The entire barrel and associated components were modeled as 316L stainless steel.

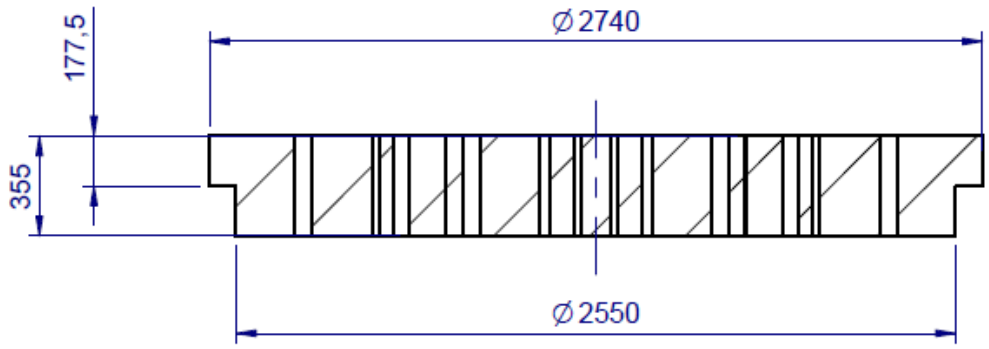

Figure 13: Bottom plate (dimensions in mm) [17]

The other part of the barrel is the lower support ring. It is the attachment point for the barrel itself and the bottom plate. Figure 14 shows the ring in the model without the eight azimuthal supports. The azimuthal supports were not modeled.

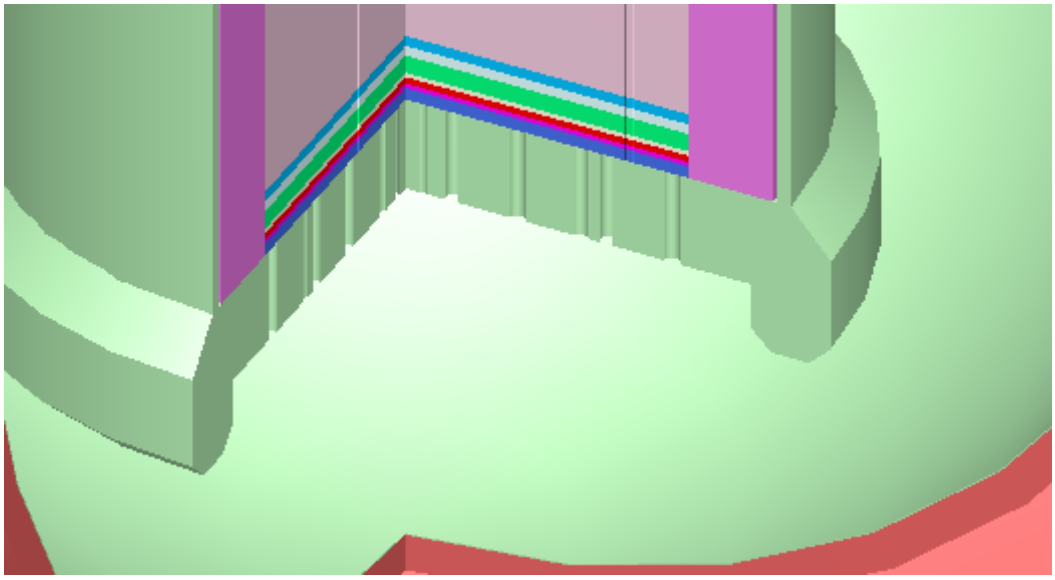

Figure 14: Ring shown with the core, reflector, barrel, bottom plate, and pressure vessel

4.5 Steam generators

The integral steam generators of IRIS are the one of the most technically challenging points in the model because of the support structure and the varying water density. Since the neutron streaming path from the core to the control room approximately passes through the bottom portion of the steam generators, it was important to capture as much of the support as possible to ensure that the model was not adversely affected by the lack thereof. There are three main components to the steam generator subassembly: the steam generator tube bundle, headers, and support structure.

4.5.1 Steam Generator Body

The steam generators are a helical Inconel tube bundle connected to a feedwater header and steam header that are encapsulated with a thin stainless steel annulus with a more robust center annulus support of stainless steel. They are completely supported by the barrel and the

pressure vessel. The tubes are connected only for their own support to the center support annulus.

The steam generator body in the model is homogenized much like the assemblies. Due to the variation of water density throughout the steam generator primary and secondary, it cannot be modeled as a single component in the system. The IRIS team provided data from a RELAP model that covered the entire system. Figure 15 and Table 4 shows the density change throughout the steam generator primary and secondary and how it was homogenized in the model respectively:

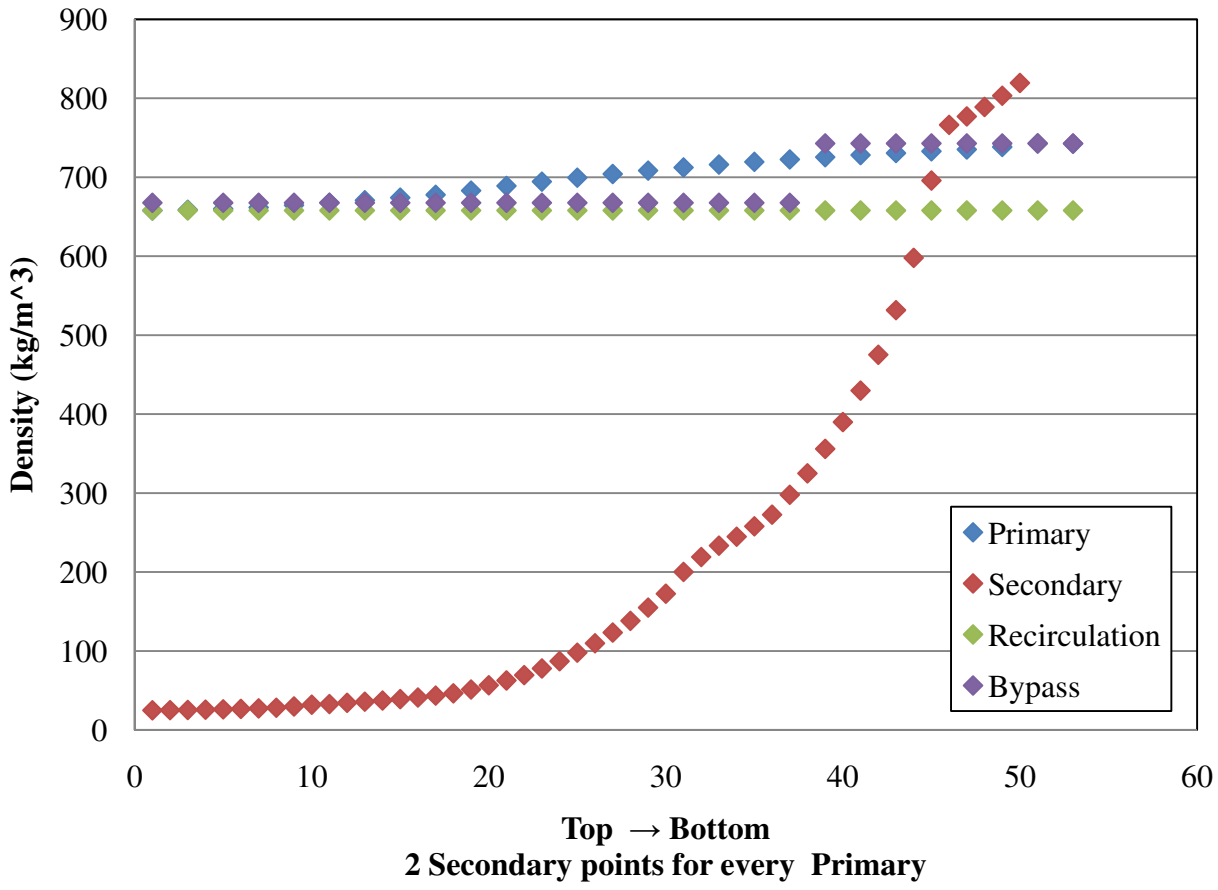

Figure 15: Density change throughout the steam generators [21]

Based on the data, it was more important to capture the changes in the secondary rather than the primary because the change was much more dramatic. However, it was not simply a matter of equal sections. The steam generator was sectioned off to capture as much of the initial change as possible because the secondary density drops off very quickly closest to the core and could provide a streaming path to the control room.

Table 4: Steam generator sections for the model

	Height (cm)	Primary (g cm^{-3})	Secondary (g cm^{-3})
Top (1)	298.8	0.67	0.0345
2	89.64	0.699	0.0842
3	89.64	0.712	0.168
4	89.64	0.722	0.272
5	29.88	0.728	0.373
6	59.76	0.731	0.509
Bottom (7)	89.64	0.738	0.775

Based on this data, the steam generator was modeled as a cylinder with annuli for the outer shroud, the tube bundle, primary and secondary water homogenization, and an annulus for the center support column filled with recirculation water.[3, 4] (Figure 16)

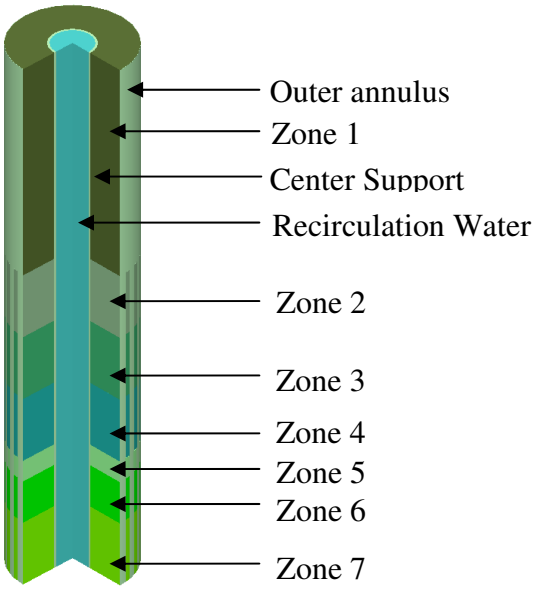

Figure 16: Steam generator

The steam generator is 160 cm in diameter and 679 cm tall. This does not include the height of the headers.

4.5.2 Steam Generator Headers

The steam generator header function is to split or recombine the secondary into one stream that is either fed to or away from the steam generator tube bundle. The steam generator header (Figure 17) is composed of Inconel, the same material as the tubes. It is tied to the central support column and it is part of the structure that is bolted to the pressure vessel wall. Non-conservatively, the headers did not include a provision for the tubes and water that passes into it. Thus, the density for both the feedwater and the steam headers are higher than they would be in the real system. However, this is not necessarily a bad assumption. The steam header at the top of the steam generator is inconsequential to the control room shielding. The feedwater header at the bottom does have some impact in the control room, but the water passing through the header walls is 0.8 g cm^{-3}, compared to the Inconel density of 8.15 g cm^{-3}, is the most dense water in the entire system. Also, the mass of the water within the header walls is very small compared the mass of the header. The water within the header was what would be under operation. The shape of the header was modeled as described in the technical drawings.

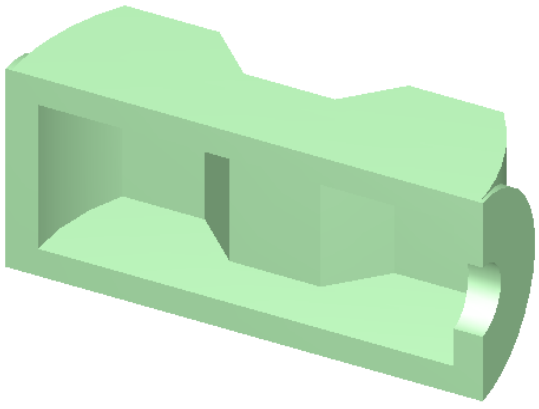

Figure 17: One half of the steam generator header

4.5.3 Steam Generator Support

The steam generator support structure (Figure 18) is a series of I-beams arranged in a way that transfers the load from the steam generator center support down to beams that are resting on flanges on both the barrel and the pressure vessel.[2]

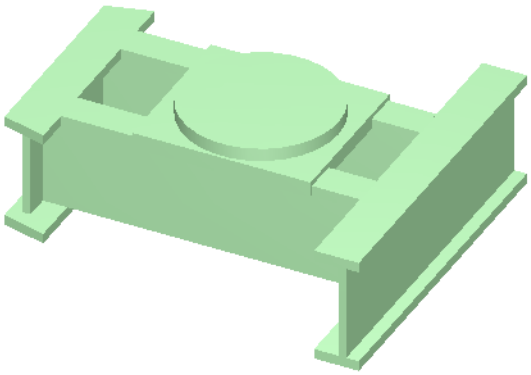

Figure 18: Steam generator support structure

It is composed entirely of stainless steel, type 316. One of the differences between the model and the real system is the lack of the curved beams that are designed to maximize the area of contact on the support flanges and minimize the primary flow restrictions. It was not possible to model these effectively as described so the model was set up to have straight beams. This is a minor difference and more conservative because a straight beam is less massive than the curved one.

4.6 Pressure Vessel

The IRIS pressure vessel (Figure 19) is composed of low carbon steel with a stainless steel liner. It is over 22 m tall with a 339 cm outer radius. There are two spherical sections capping a cylindrical tube. The pressure vessel was modeled with two materials: a low carbon steel body and 316L stainless steel liner.[15, 14, 19] Dimensions are as follows:

Table 5: Pressure vessel major dimensions

	Radius to Stainless Steel (cm)	Radius to Carbon Steel (cm)	Outer Radius (cm)
Upper Hemisphere	310.65	311.15	325.16
Cylinder	310.65	311.15	339.16
Lower Hemisphere	310.65	311.15	327.15

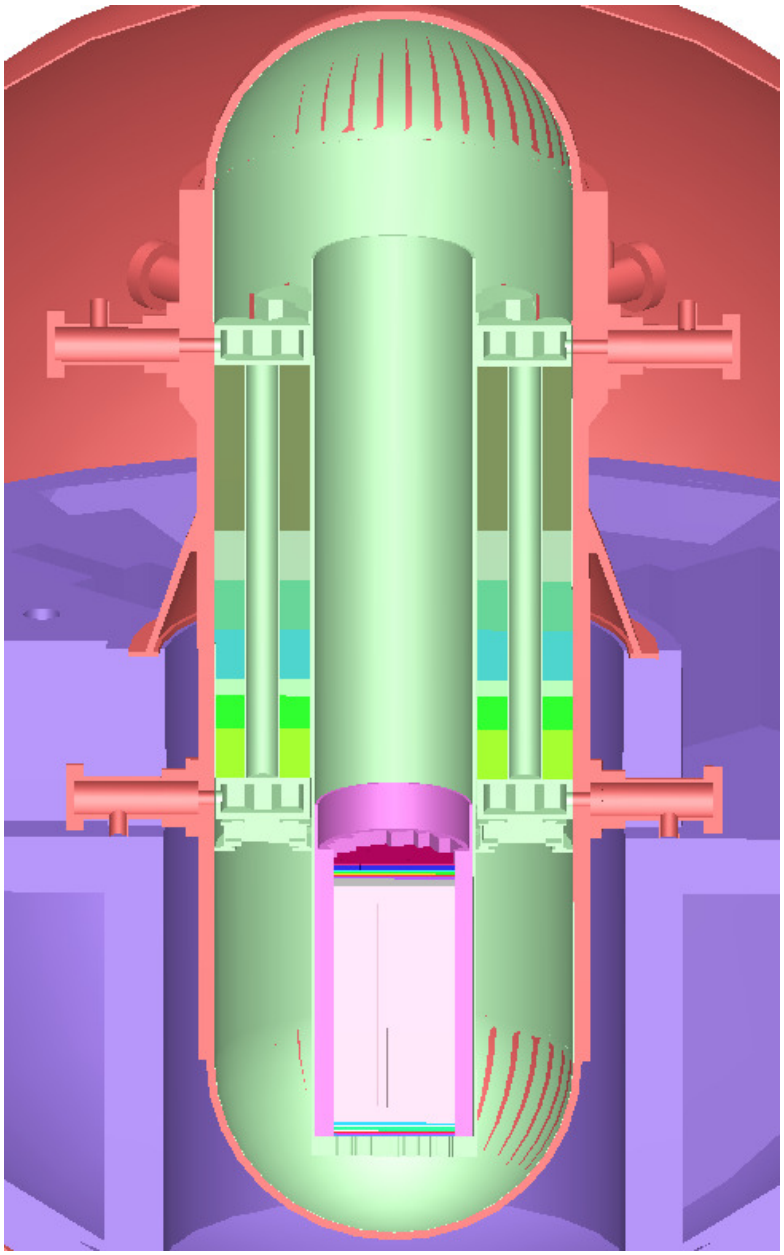

Figure 19: IRIS pressure vessel in containment with all modeled internals

Nozzles (Figure 20) for the pressure vessel are the locations for the penetration through the primary pressure boundary to the steam generators.

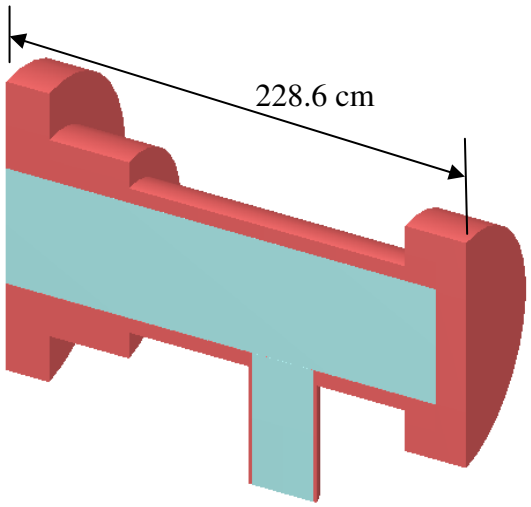

Figure 20: Feedwater nozzle model cutaway view

They are composed of the same material as the pressure vessel. Their modeling was not consistent with the drawing; the design was simplified to a set of concentric cylinders rather than cones for simplicity.[19] This results in a conservative model with less mass than the drawing.

4.7 Containment Vessel

The containment vessel is a 25 m diameter spherical shell made of carbon steel 4.5 cm thick. Its primary function is to mitigate the consequences of and ultimately be the second line of defense in an accident scenario where there is a primary pressure boundary failure.

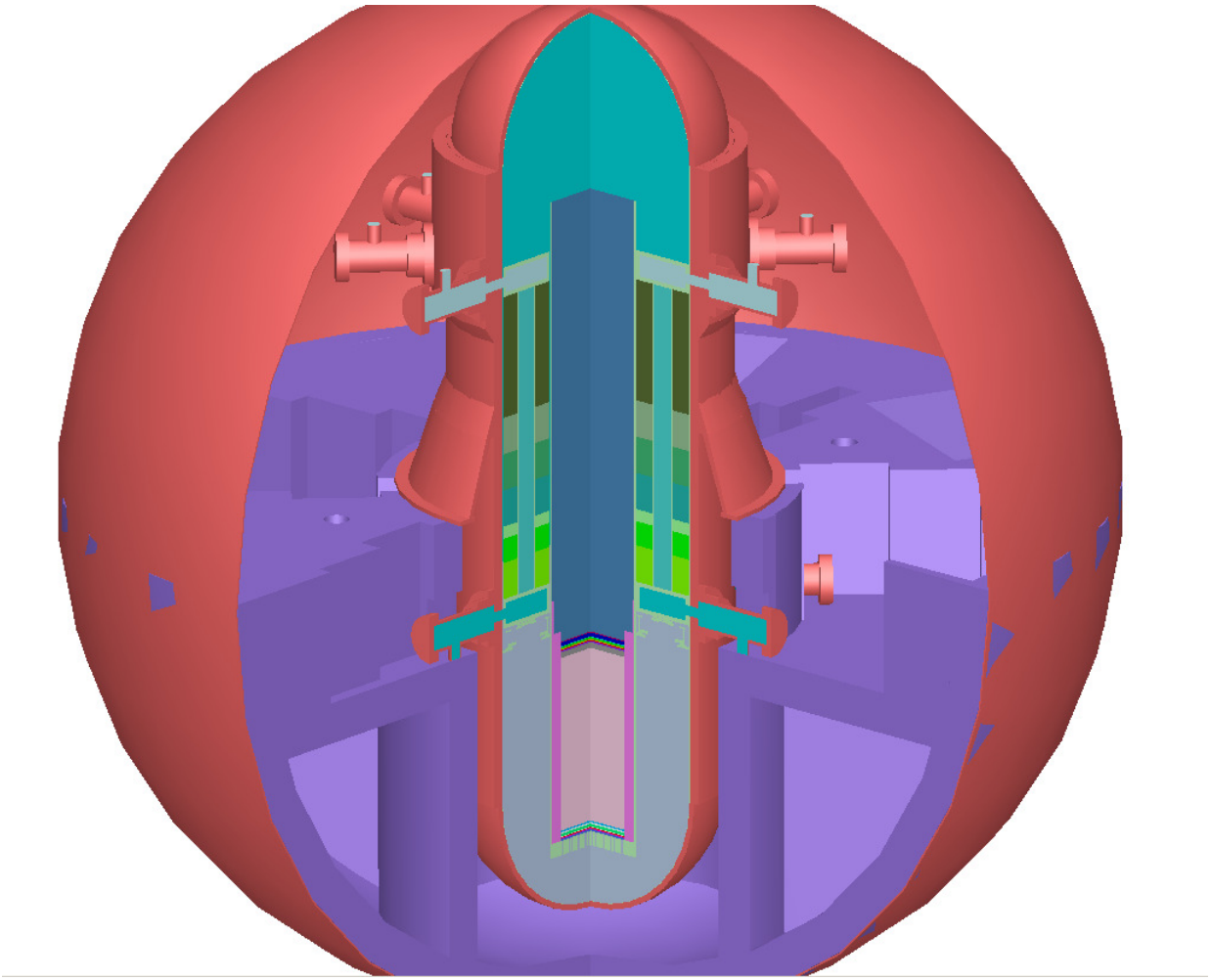

Figure 21: Containment

The containment vessel also has a concrete structure within it designed to support the pressure vessel. It contains highly irregular shapes and cutouts used for feedwater and steam piping and associated tanks for operation. The containment header, a large removable section of the top of the containment vessel tied to the pressure vessel for refueling, was not modeled because it was not relevant to the shielding analysis covered in this thesis. This is more conservative as well.

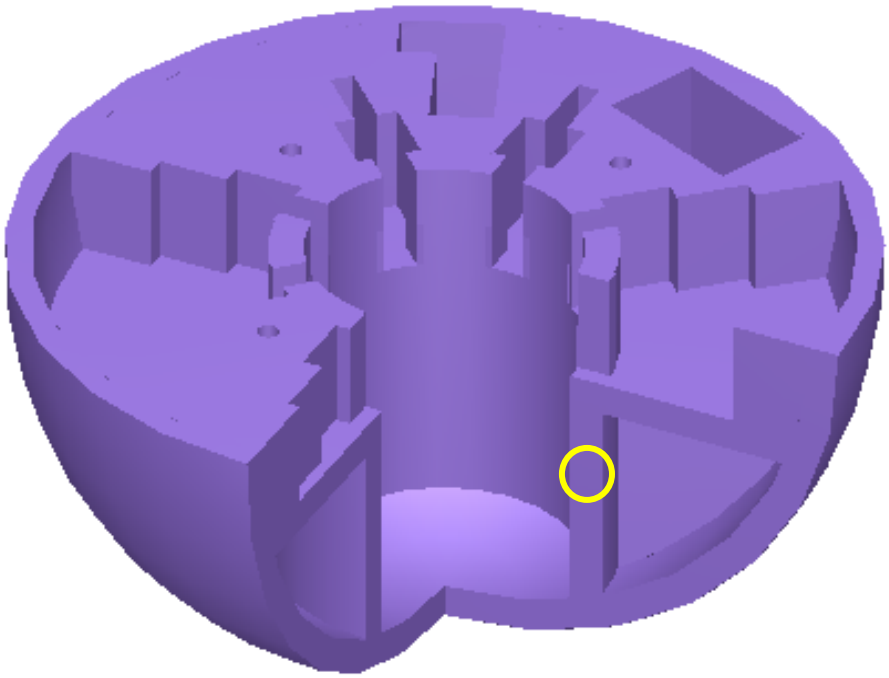

Figure 22: Concrete in containment

As shown in Figure 22, the concrete in the containment is a primary shielding mechanism for the areas beyond the reactor.[41] However, only the vessel cavity wall (highlighted in yellow) where the reactor is supported will be investigated. Previous work has shown that that is the only area of non-negligible concrete activation.[5] This region is separated from the pressure vessel by the containment atmosphere, nitrogen gas at an assumed pressure of 100 kPa.

4.8 Reactor Building

The reactor building is a cylindrically shaped building with the lower 20 m below grade. It is composed of eight floors of varying shape and function to house all the reactor safety and control systems and constructed entirely of concrete.[42] Each floor was modeled individually and then the building was stacked together to form a complete model. Each room is modeled as closely as possible to the IRIS plant technical drawings with each room completely empty. The

reactor building model was developed but not included in any of the analyses in this thesis and was also not validated. The analysis of the building will be completed in future work.

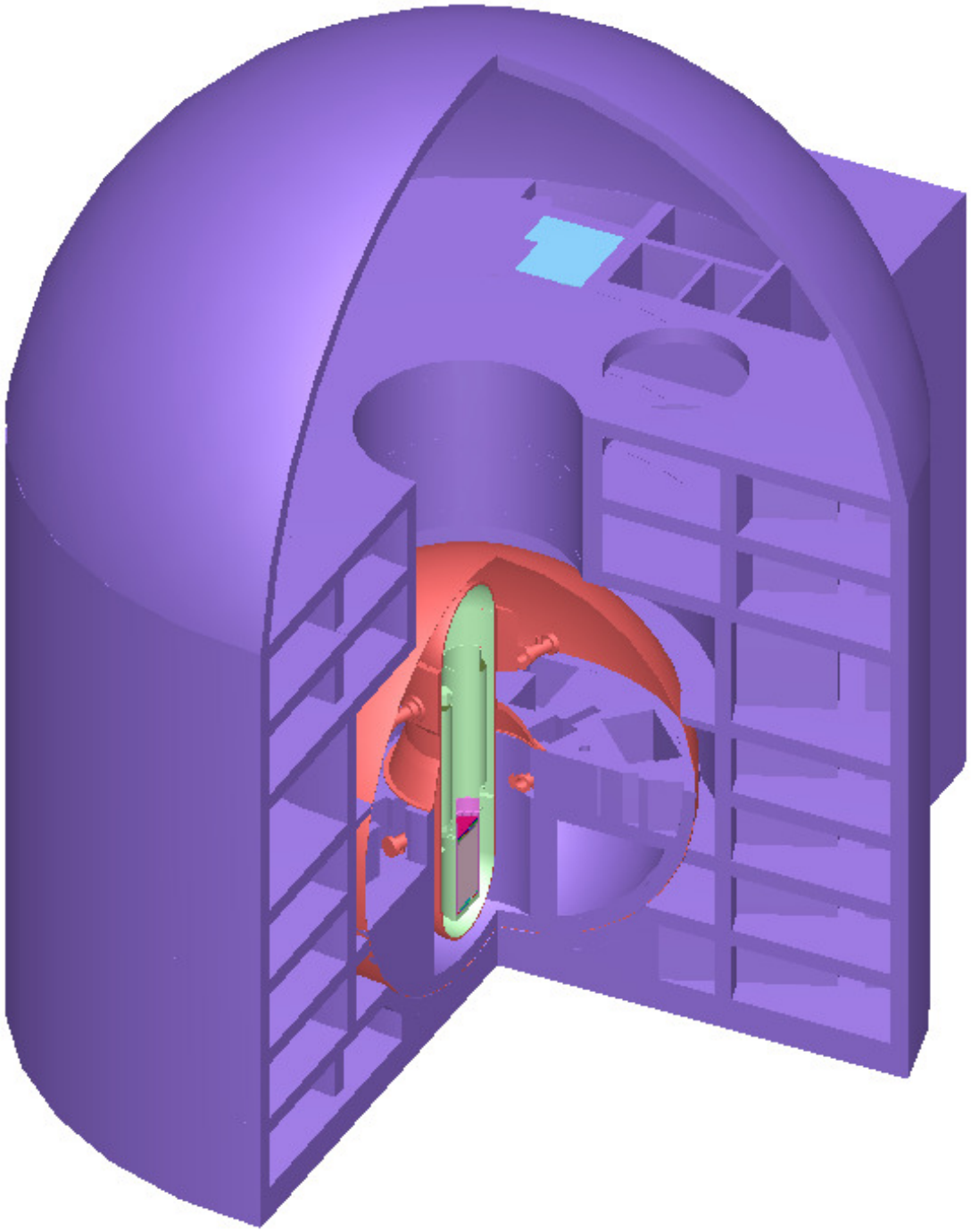

Figure 23: Whole reactor building

4.9 Model Geometry Structure

The SCALE standard geometry requires that a unit is a single universe that can be inserted into other units. This feature, along with the array function, makes the modeling easier because repetitive items only need to be constructed once and then may be inserted as many times as necessary where they need to be. For example, the steam generator body is a unit. That unit is inserted into the pressure vessel in eight different locations as described[14]. There are some limitations: units can not overlap each other and they must be completely encapsulated by the unit in which they are placed. The entire model can be described with the following hierarchical tree:

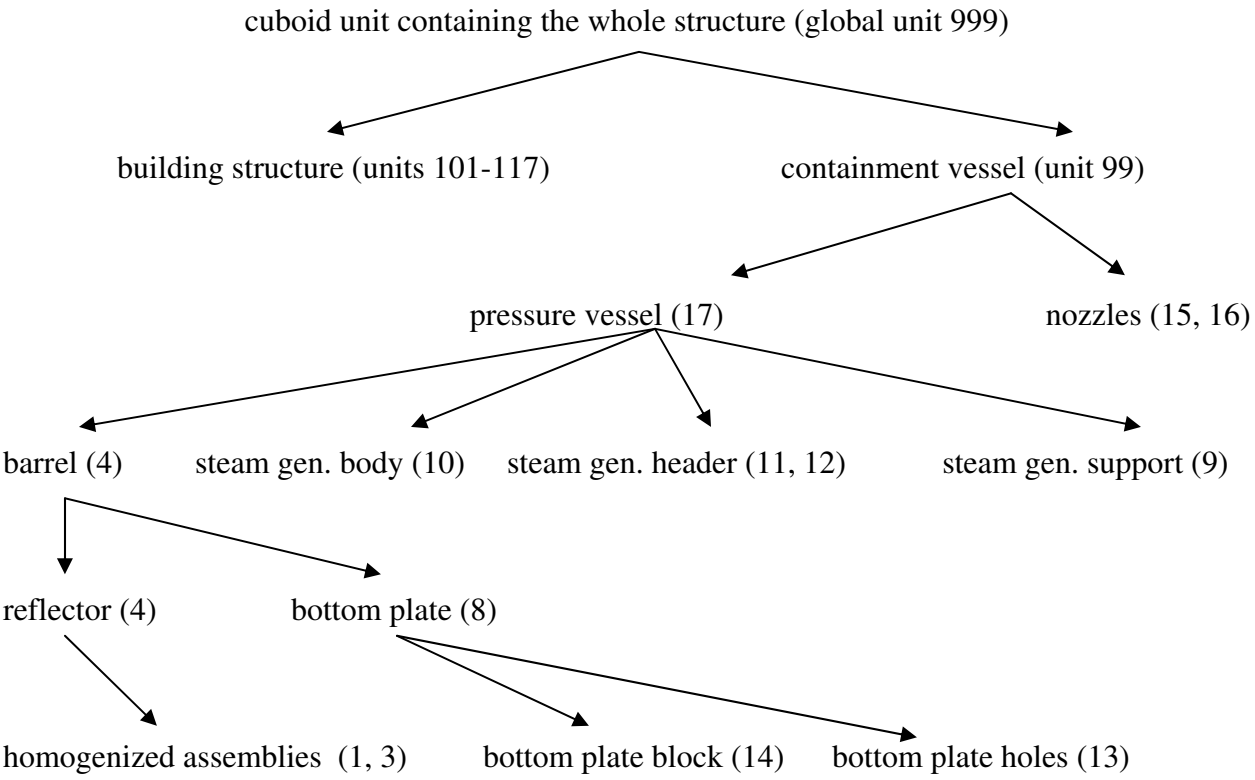

Figure 24: Hierarchal tree diagram of the model

4.10 Temperature profile of the pressure vessel

Figure 4.22 shows a flow chart with the varying temperatures in the pressure vessel.

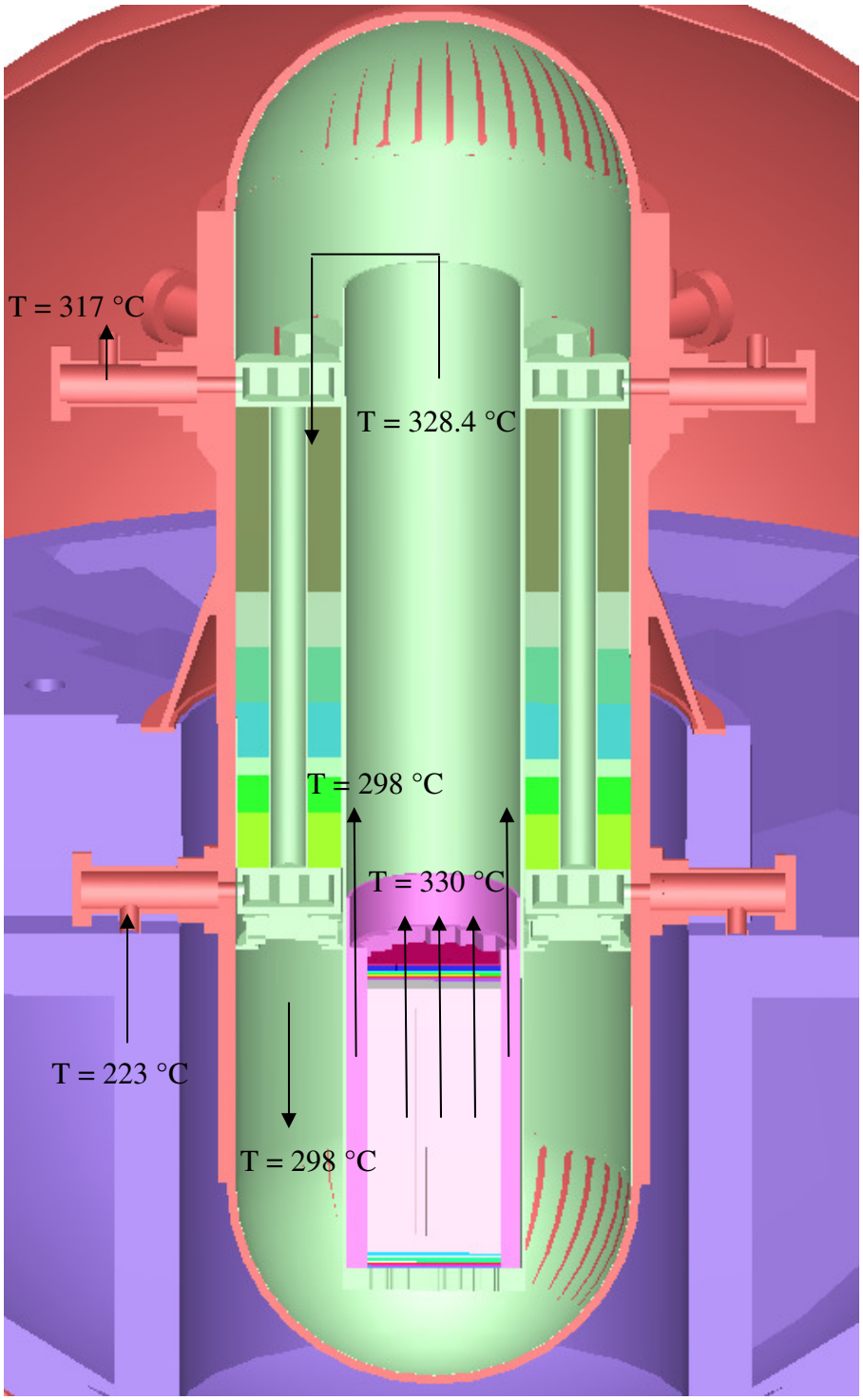

Figure 25: Temperature profile superimposed on the pressure vessel

In the model, the densities were properly accounted, but the temperatures were not used for cross section correction. The entire model was developed with all materials at room temperature. Future work will examine the implications of this assumption.

4.11 Other Model Options

Within the MAVRIC sequence, there are many options to fine tune the simulation. The following will describe the options used for simulations performed.

4.11.1 Response Functions

MAVRIC has the ability for the user to input responses that can be used for the adjoint portion of the simulation or to tally with weight based on the response. For this simulation, there were three responses used: $^{59}Co(n,\gamma)^{60}Co$, $^{151}Eu(n,\gamma)^{152}Eu$, and $^{153}Eu(n,\gamma)^{154}Eu$. These responses make it very easy to calculate the activation which will be discussed in depth in Chapter 6.

4.11.2 Grid Geometries

MAVRIC simulation is based on the geometry of the system with all the user assigned materials for that geometry. Then grids must be overlaid for the forward and adjoint meshes as well as all the tallies. These grid geometries are defined by the user and can be regularly or irregularly spaced. The system is limited to only xyz geometries for the meshes but that allows the discrete ordinate calculations to run in parallel.

SCALE6 includes the capability to view two dimensional slices of the output files using the Meshview viewer. As an example, Figure 26 shows an output with the mesh overlaid on the model geometry and materials assigned.

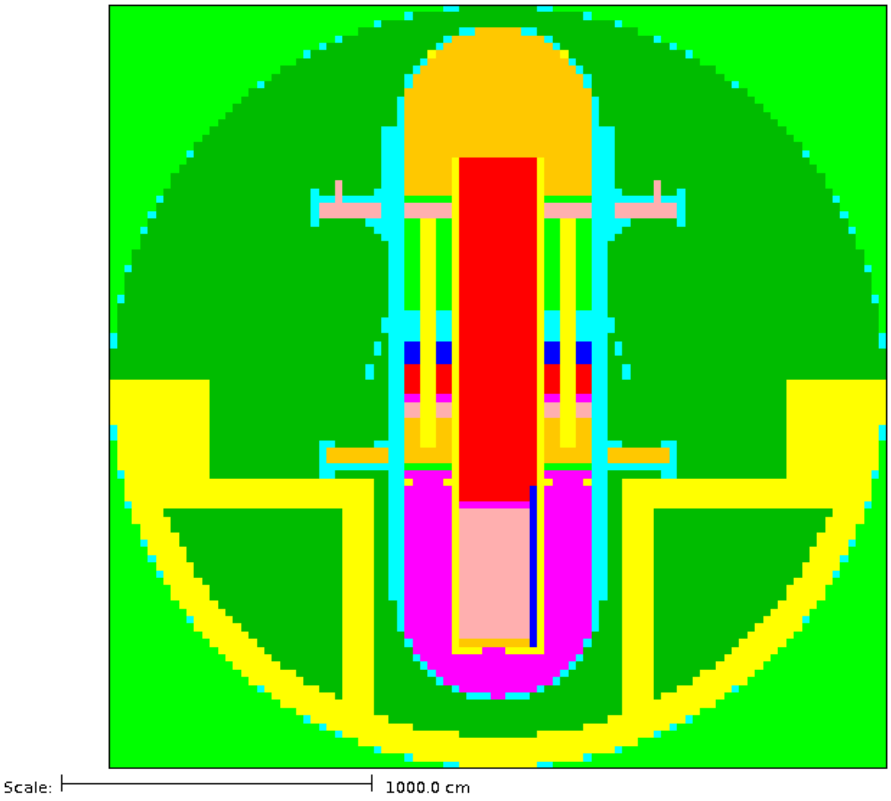

Figure 26: Materials as computed with a 100^3 mesh

This example covers the whole containment volume (1254.44^3 cm^3) with 100^3 meshes. The view shows all the different materials in the system and how they were set up on the mesh. This mesh was used for both the forward and adjoint calculations as well as the tallying mesh. However, different meshes can be used for different portions of the simulation.

4.11.3 Source

The source defined in the simulation was an isotropic Watt fission spectrum for ^{235}U that sampled uniformly from the material in the active core region. The source used was based on the power of 1000 MW_{th}. From this power, the total neutron fission source density was calculated to be 7.89E+19 neutrons s^{-1}. This assumed that the energy per fission was 192.2 MeV and there were 2.43 neutrons per fission released. Fission gammas were not included. Due to a limitation

in the MAVRIC version used for this study, it was modeled as a flat distribution that is sampled uniformly, not a real distribution that accounts for the decreased power at the core periphery. The source density at the core periphery, driving the activation outside the vessel is approximately one half of the calculated average, thus could be represented by the total source of 3.45E+19 neutrons s^{-1}. Using the average everywhere is conservative because the flux was artificially increased at the core edge. Later versions of SCALE will include the capability to insert a real flux distribution, like the one that is available for IRIS, for a more accurate analysis.[22]

4.11.4 MAVRIC Options

The importance block of the input contains the keywords for all the options relating to the generation of the importance map. For most of these, the defaults were used. Non defaults that were selected pertained to the iteration scheme used for the forward and adjoint. GMRES is the default iteration method; it is a rather robust sparse matrix iteration method but there were memory faults when trying to use it with a large number of meshes (> 1M). Smaller number of meshes worked well with GMRES and it was reasonably fast. The iteration method used for the large number of meshes was the Richardson iteration. This method did not cause the memory faults and converged but was slower. Upscattering only used the Richardson iteration method. The options that most affected the runs and were adjusted to improve performance were the S_N and P_L order, and the convergence criteria for the forward and adjoint portions of the simulation. Values for S_N ranged from 3-8, P_L from 1-4, and convergence was either 0.01 initially for speed or 0.001 for better results. The effects of these will be discussed in Chapter 5.

4.12 Materials used

Table 6 shows all the materials used in the model along with their densities and relevant comments where they appear in the model.

Table 6: Materials in the model

Material	Density (g cm^{-3})	Location
Water	0.028-0.84	Throughout the pressure vessel
SS 316L	7.94	Used for pressure vessel internals and liner
Carbon Steel	7.82	Pressure and containment vessels
Inconel 600[1]	8.3	Steam generator components and assembly homogenization
Regulatory Concrete	2.3	All concrete in the reactor building
Dry Air	0.0012	Atmosphere in the building
Nitrogen	0.0012	Atmosphere in containment
Zirconium	6.49	Component in assembly homogenization
Helium	0.00223	Component in assembly homogenization
UO_2	10.416	Fuel at 4.95% ^{235}U in the assembly homogenization

[1] Note that Inconel 600 was the material used in the model. IRIS will use Inconel 690 for all materials requiring Inconel.

CHAPTER 5

IRIS MODEL VERIFICATION AND VALIDATION

It is necessary and prudent to verify and validate the model before performing analyses. The verification confirms that the code works correctly as intended. The validation demonstrates that for the application of interest accurate results are obtained. This coupled with good engineering judgment and sound assumptions enable the user to obtain results that can be trusted. The verification of this model will be discussed in detail in this section.

5.1 Geometry verification by model "flooding"

The first verification test was performed on the model to ensure that the geometry was correct and that during the Monte Carlo portion of the code, no particles would be lost due to ill configured geometries. Personally, the author had no previous experience with the SCALE General Geometry Package (SGGP), so this test was extremely helpful.

The model, as previously mentioned, is based on SGGP which itself is a system similar to a Matryoshka doll. Users define units which can be inserted into other units to grow the system, minimizing the time required to model repetitive units. As the model grew in size, units were checked using a particle flooding procedure. Histories were sampled over the entire unit in great quantities. If any of those histories were lost, an error was recorded, the geometry issue was fixed, and the procedure repeated until there were no more problems. As this thesis only covers

the concrete in the containment, two units received the flooding treatment: the pressure vessel and the containment vessel.

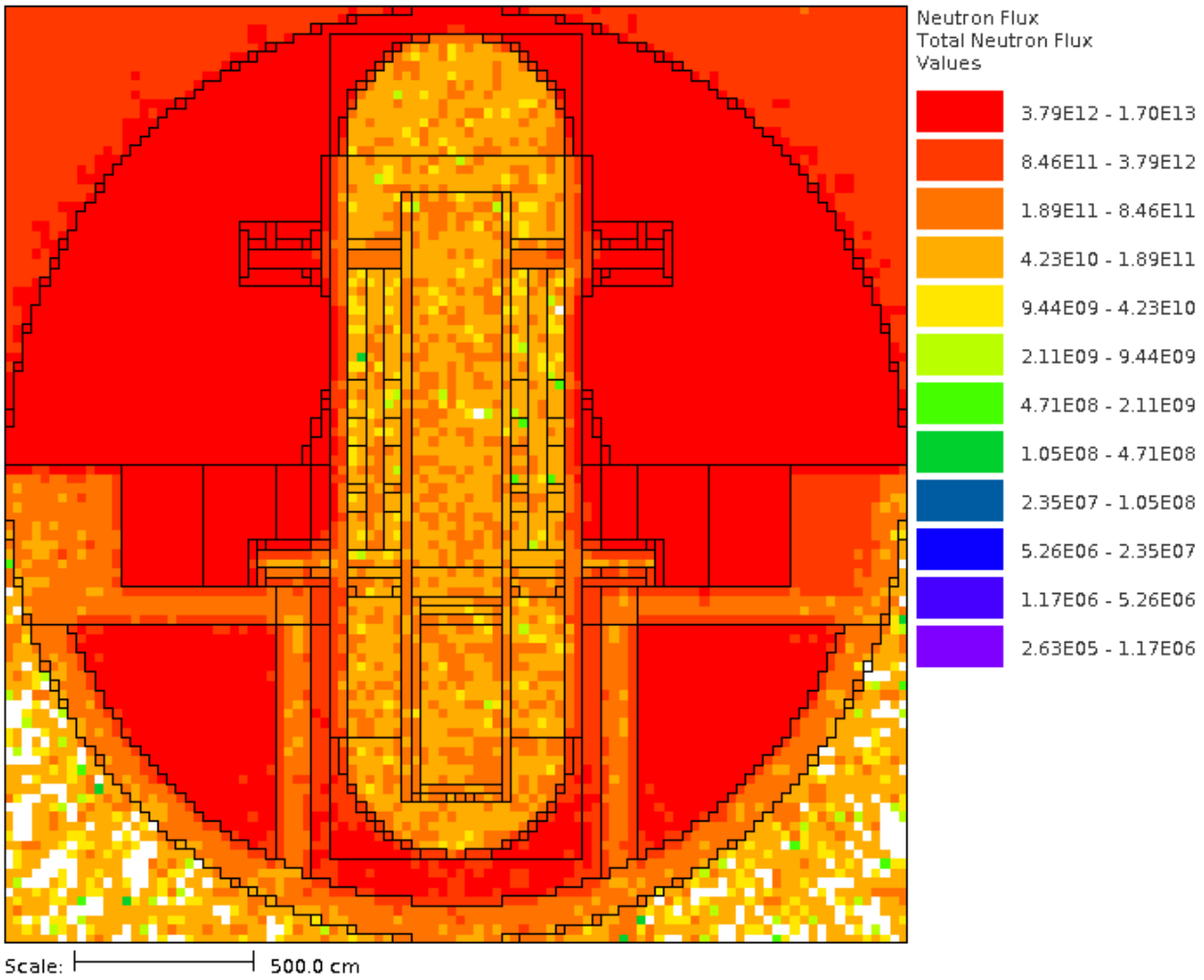

Figure 27: Pressure and containment vessel flood

Figure 27 shows the results of flooding the containment with particles from a unit source over the entire containment volume. The containment volume is defined as mentioned previously in section 4. 7 as a 25 m diameter steel sphere so some white areas under the sphere, indicating no data for that voxel, are acceptable. It is also important to note that with a uniform unit source everywhere, the density will have an influence on the voxel tally. Areas in red are the areas of containment that are at containment atmosphere inside the sphere or reactor building atmosphere

if outside. Lower results recorded in the higher density regions, such as the core and the concrete are expected. The containment atmosphere was assumed to be just slightly less than the reactor building atmosphere with a density approximately 0.0012 g cm^{-3} while the concrete was 2.3 g cm^{-3}. Not surprisingly, the results in the concrete are about two to three orders lower than in the containment atmosphere. Satisfactory coverage of all the containment volume was achieved making it unlikely that geometry errors were left unidentified.

5.2 Verification of the overall variance reduction procedure functionality

Another test was a run simulating the fast flux throughout the containment from the correct source location using the FW-CADIS method. In this case, the source response was based on a unit group-wise response covering the top six groups of the 27n19g ENDF VII library. This simulated all neutrons above .9 MeV. The mesh for the forward portion was 100^3 voxels covering a cube that was 2510^3 cm^3 with a resultant mesh size of 25.1^3 cm^3. This is not necessarily bad for the fast flux in this verification run. The source was sampled from the core location using the biased source developed during the simulation. For speed, P_L=1, S_N=4, and a convergence value of 0.001 were used.

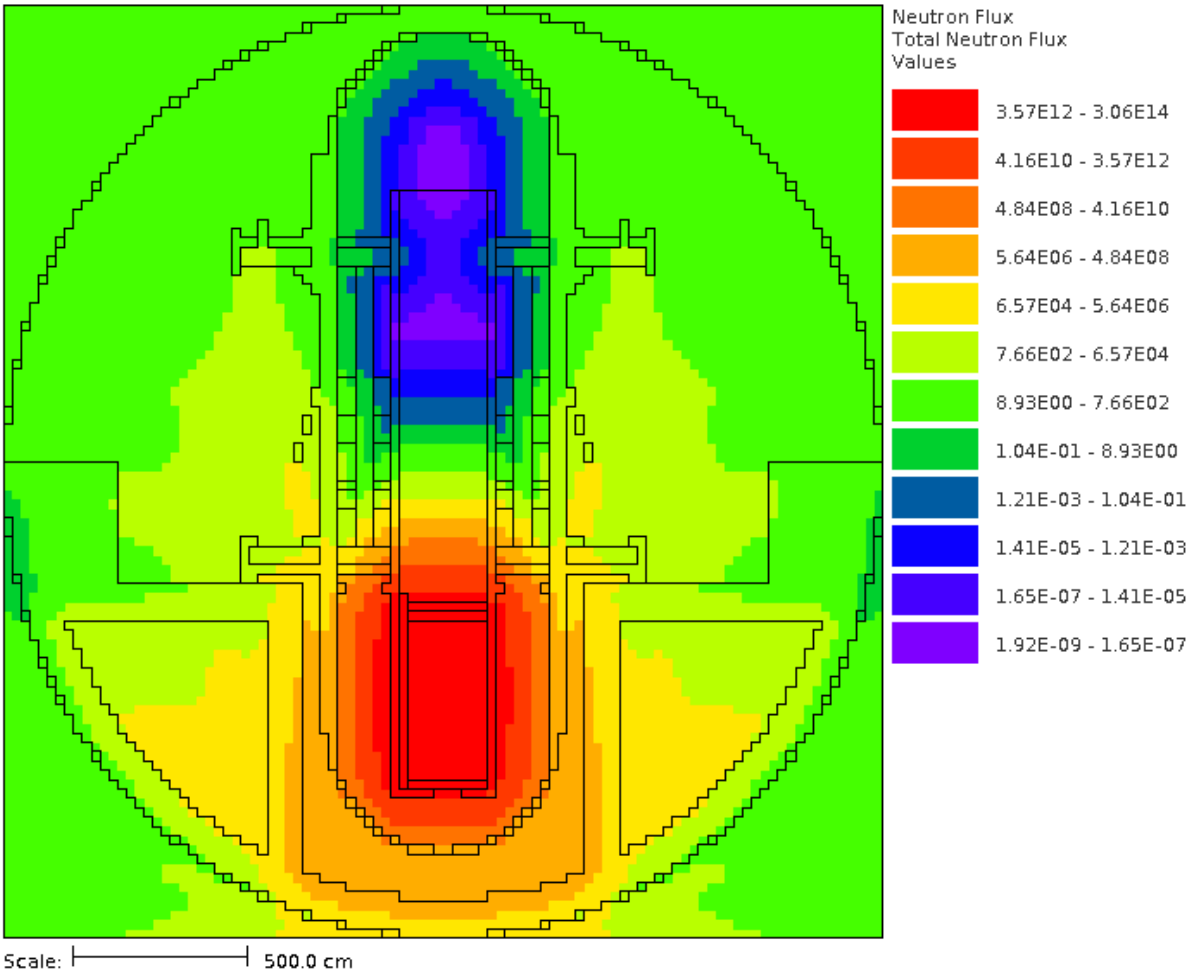

Figure 28: Forward deterministic estimate

In Figure 28, the forward deterministic estimate of the fast neutron flux is shown. It is the first result from the FW-CADIS sequence. Impressively enough, there are over 19 orders of magnitude represented in this figure. The prediction of this reduction by the forward deterministic calculation will be used to weight the adjoint shown in Figure 29.

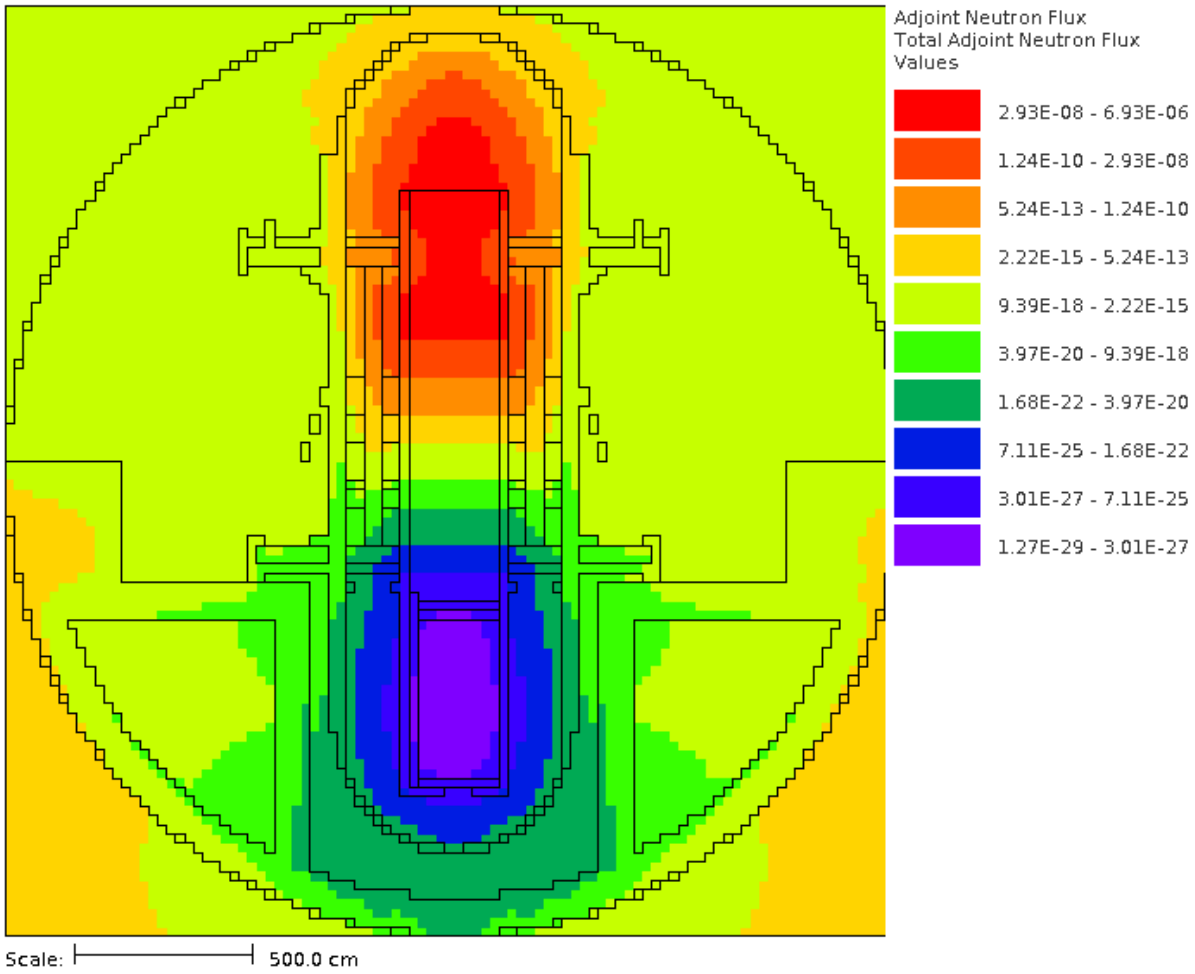

Figure 29: Fast flux adjoint estimate

The area predicted to be most difficult for this simulation was directly above the core near what would be the pump location. This makes sense with the amount of shielding that ten meters of water would provide. The actual flux is estimated to be the lowest and thus it needs the most importance to guarantee that the relative uncertainty will be the same as elsewhere.

From the adjoint and the forward, the importance map is created shown in Figure 30.

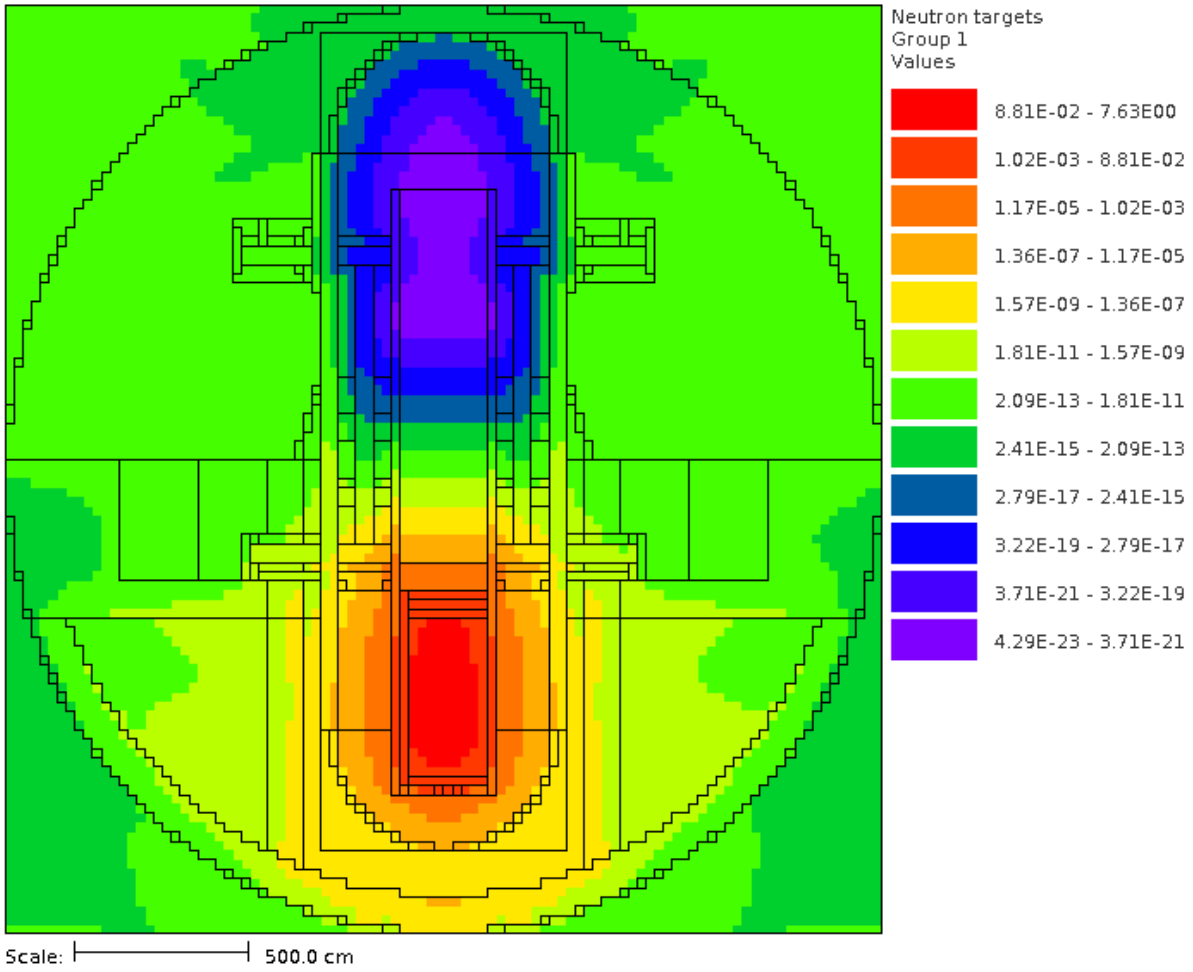

Figure 30: Fast flux importance map for neutron group 1

The importance map is in terms of the neutron target weight which is the inverse of the importance. Based on Equation 3, the weight window in space and energy (group-wise in this case) is calculated from the response over the expected flux. It is very similar to the adjoint estimate shown above. However, the importance map works with the consistent biased source to decrease the computational time. By itself (without the consistent source biasing) particles would be generated in the source voxels only with the incorrect weight. This would waste needless time tracking particles with negligible contributions to the tallies in the area of interest.

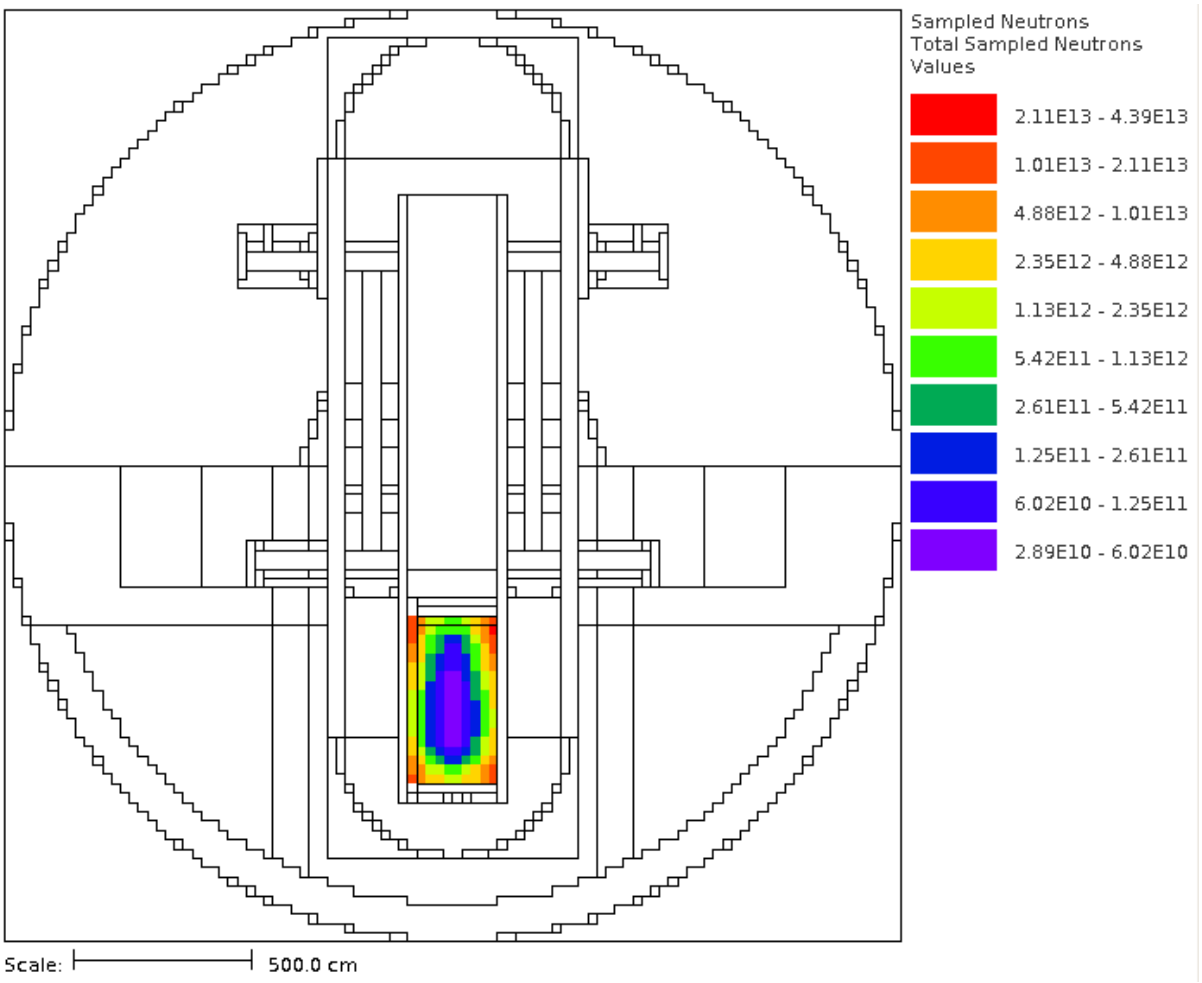

Figure 31: Consistent-biased source for the fast flux verification

The consistent-biased mesh source is created from estimate of the forward and adjoint flux. As shown in Figure 31, MAVRIC is already beginning to compensate to attempt to generate uniform variance throughout by determining what source area are more important to the results rather than wasting time on all source particles equally.

The final portion is the Monte Carlo results. For this simulation 200 batches with 10,000 particles per batch were used. Figure 32 shows the total flux from all groups by voxel and Figure 33 shows the associated variance by voxel.

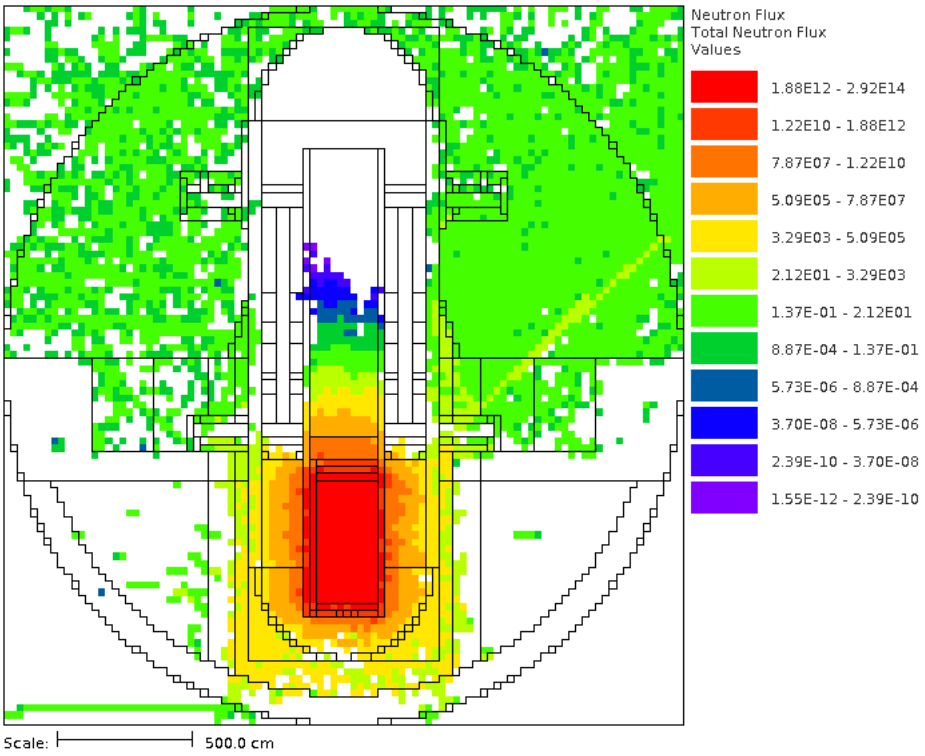

Figure 32: Fast flux Monte Carlo results

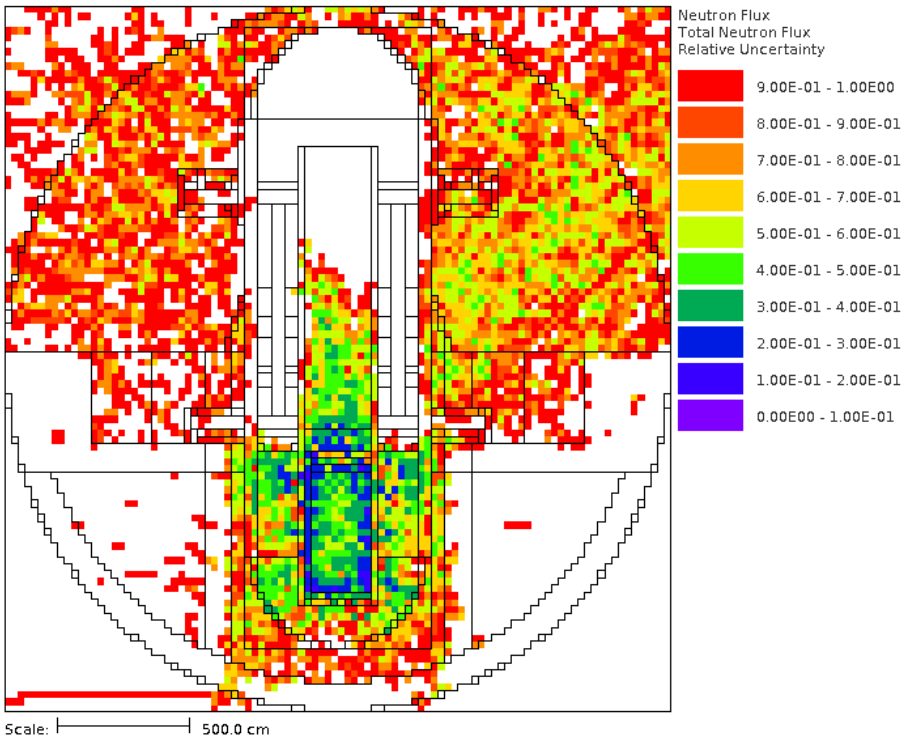

Figure 33: Relative uncertainty for Figure 32

The results were generated using a single core of an Intel Xeon X5355 at 2.66 GHz with 16 GB of RAM. CPU time used for individual steps in the MAVRIC sequence is shown in Table 7.

Table 7: CPU times for the fast flux calculations

Calculation	Time (minutes)
Forward	81
Adjoint	6
Monte Carlo	138
Total	225

For such a large geometry and so few histories, it is impressive to see that in only about two and an half hours of Monte Carlo time, there can be results generated that are over 20 orders of magnitude lower than the core.

Extending this verification run involved reusing the same mesh source and importance map re-running the Monte Carlo portion for enough histories to get about an order of magnitude longer running time. This run used 48 million histories as opposed to the 2 million for a run time of 22.8 hours. This should show more results and a decreased variance in the voxels that had results from the run shown in Figure 33. Figure 34 contains the results from running for 22.8 hours. Figure 35 shows the relative uncertainty for Figure 34.

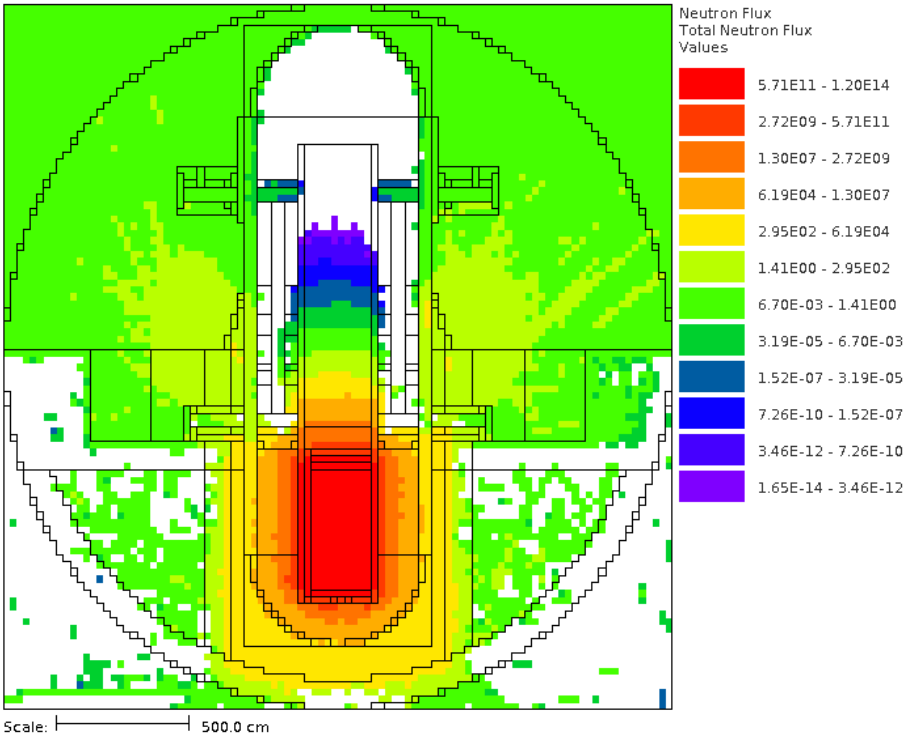

Figure 34: Fast flux for 20 times more histories

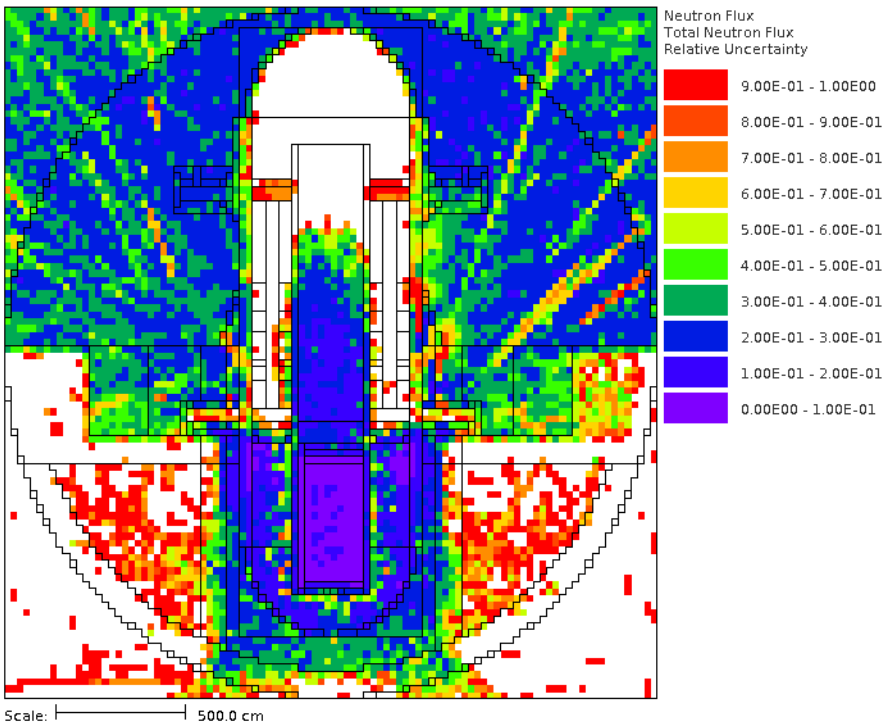

Figure 35: Relative uncertainty for Figure 34

As shown, the results for the increased time are much better both in quantity and quality. There are still areas with larger uncertainties, notably the concrete wall around the core but that is due to the large mesh size used for deterministic calculations resulting in a not very accurate variance reduction parameters, and consequently variation in the statistical uncertainty. The results of these two verification runs indicate that the geometry is correct and that the code is running as expected.

5.3 Validation

There are two concurrent models that are being developed in the IRIS Shielding Working Group. One is an MCNPX model based on Burn's DSA method; the other is a deterministic calculation using TORT from the Doors3.2a package.[6, 35] Based on these two models, a comparison can be made to the MAVRIC model as a check to see if the results are consistent. Each model is making somewhat different assumptions and the capabilities of each code package are different. For example, both the MCNPX and TORT codes have the ability to input a space-dependent source distribution. It is then expected to have some differences in the results.

5.3.1 MCNPX Comparison

A detailed MCNP5/MCNPX model of the IRIS reactor building was developed by K. Burn at ENEA/Bologna, Italy.[5] In the MCNPX model, there were different tallies created in the concrete region to check the flux levels, as shown by the superimposed white numbers in Figure 36.

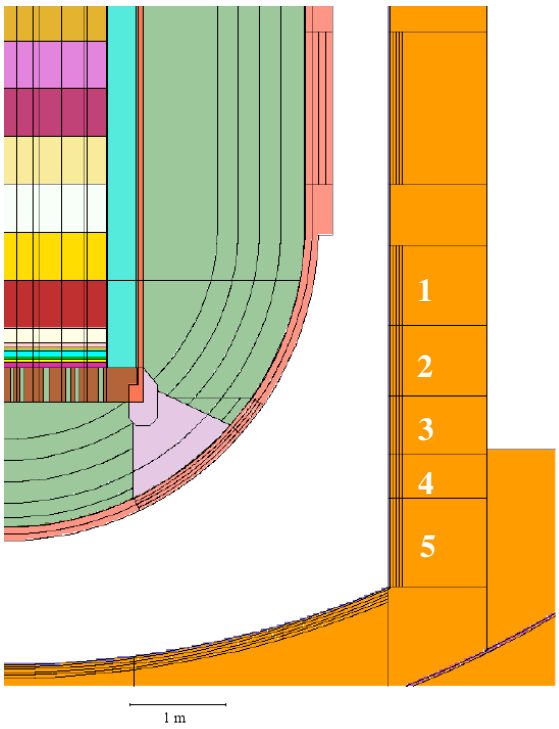

Figure 36: MCNPX model showing locations of tallies for comparison [5]

The MAVRIC model was altered to include a tally at the same locations. Burn reported his values as reaction rates. Table 8 shows the comparison between the MCNPX model and the MAVRIC model. The values shown are for the $^{59}Co(n,\gamma)^{60}Co$ reaction per gram per second taking place in the concrete assuming a concentration of 10 ppm by weight.

Table 8: Comparing the values of the MAVRIC and MCNPX Models

	MCNPX	MAVRIC	
	Reaction Rate	Reaction Rate	Relative Uncertainty (1σ)
1	0.015	0.018	0.0015
2	0.02	0.019	0.0016
3	0.023	0.022	0.0017

The MVARIC results shown in Table 8 are for four symmetric locations in the concrete at *x* and *y* axes averaged together. The MCNPX results are integrated around the entire cavity wall tally

volume. The obtained values are very close to the MCNPX model by Burn, i.e. consistent with the statistical uncertainty of the results and before any safety factors are applied.

5.3.2 TORT Comparison

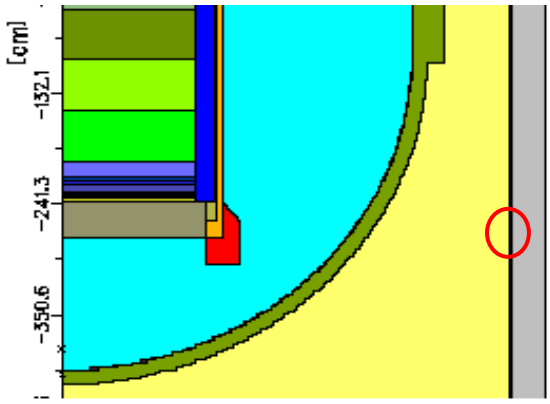

Figure 37: Location of maximum flux in the TORT model [11]

A 3-D TORT model of the IRIS containment was developed by M. Sarotto, M. Ciotti and R. Orsi at ENEA/Frascati, Italy.[11] For the TORT model, the comparison was straightforward. Results for the TORT model are displayed as flux maps. As a basis for the comparison, the maximum neutron flux in the cavity concrete wall found in the TORT model was compared to that same location in the MAVRIC model. [11]

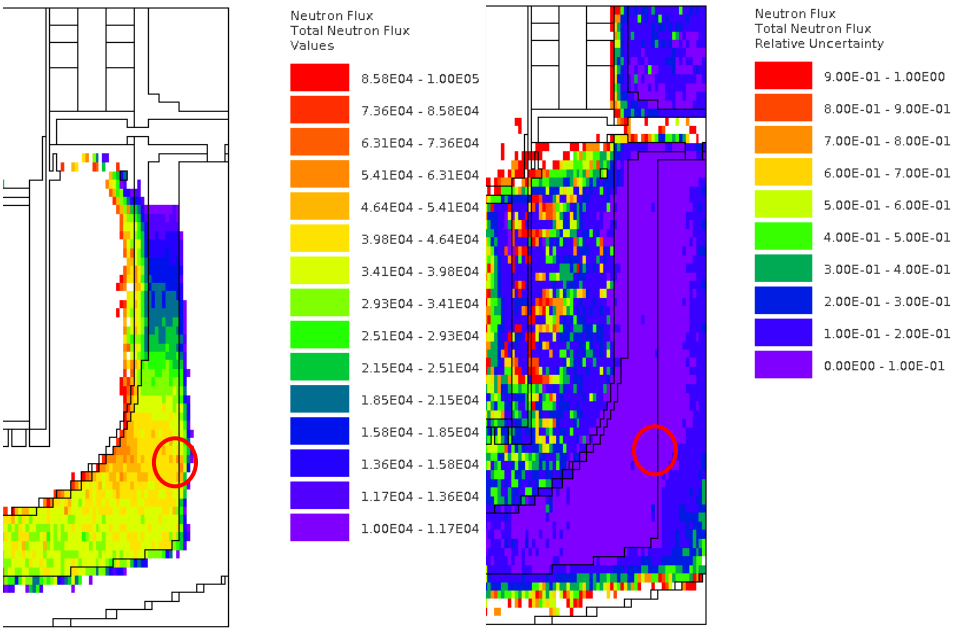

Figure 38: Comparing the MAVRIC model to TORT

Table 9: Comparing the flux values of the MAVRIC and TORT Models

	Flux (n cm^{-2} s^{-1})	Relative Uncertainty
MAVRIC	4.45x10^4	6.30%
TORT	2.75x10^4	-

This agreement is within a factor of two which is acceptable considering the differences in the models. The relative uncertainty for the MAVRIC model is well within reason to allow making a meaningful comparison.

5.3.3 Discussion

For both comparisons, the agreement is acceptable once the assumptions are considered. For the MAVRIC model, there is no spatial source distribution dependence, which was compensated by artificially decreasing the total source. Based on the concurrent work and results, the MAVRIC model appears to be valid.

CHAPTER 6

ANALYSIS OF CONCRETE ACTIVATION IN THE IRIS REACTOR VESSEL CAVITY

This Chapter presents results of analyses performed to assess activation of the concrete wall in the IRIS reactor vessel cavity.

6.1 Model Features and Options Used in Analysis

For the all results in this section, the model used was the same. Since only the reactor vessel cavity was considered the model was reduced in size from the full containment to the outer extent of the cavity wall. This resulted in a size where x=y=1000 cm and z=1270 cm. There were 143 meshes in the x and y direction and 72 in the z direction for a total of 1472328 meshes with a size of 862 cm^3 each. The mesh size in x and y was 7 cm and in z it was 17.6 cm. This mesh was used throughout the analysis, both for deterministic calculations and Monte Carlo tallying. Figure 39 shows the materials and geometry used. The concrete (region of interest) is shown in dark green.

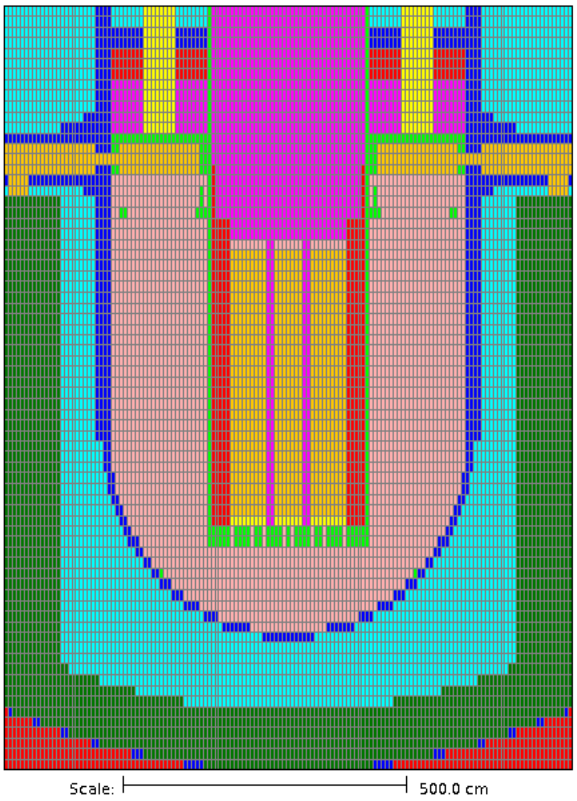

Figure 39: Mesh and geometry used for results

This was the best compromise based on the computational resources limitations, with the sequential deterministic and Monte Carlo codes limiting the use to a single processor. It is important to remember that the deterministic mesh is used for creating the importance map, not the results. If due to a coarse mesh the map is not perfect for the geometry, materials, and mesh tallies, it will take longer in Monte Carlo to converge to low uncertainty, but the results will nevertheless be unbiased, and very likely computationally still more efficient than if using a manual variance reduction.

Options for the deterministic portion of the simulation were P_L=3, S_N=8, and a convergence criterion of 0.001. The deterministic calculations took 560 and 327 minutes for forward and adjoint respectively. For the results, all the neutron groups were simulated but for

creating the importance map, upscattering was neglected. Using upscattering during the deterministic portion of the run was tested, but it increased the time by an order of magnitude and was deemed not practical. Instead of spending that time in accounting for upscattering in forward and adjoint deterministic calculations for the importance map, that time was made available to the Monte Carlo portion which produced a better overall efficiency.

The adjoint was set up to drive particles to the cavity concrete wall material at the expense of other regions. There were three adjoint responses corresponding to capture cross sections of the three reactions of interest.

Table 10: Isotopes of interest

Isotope	Reaction	Product	Half Life (y)	2200 m/s cross section (b)
^{59}Co	(n,γ)	^{60}Co	5.2714	38
^{151}Eu	(n,γ)	^{152}Eu	13.516	8000
^{153}Eu	(n,γ)	^{154}Eu	8.593	200

These reactions are primarily responsible for concrete activation. Since the energy dependence is similar, but the magnitude is significantly different, they were merged into a single simulation, scaling their importance based on the inverse of the maximum cross section as follows:

Table 11: Response weights

Response	Weight
^{59}Co(n,γ)^{60}Co	500
^{151}Eu(n,γ)^{152}Eu	1
^{153}Eu(n,γ)^{154}Eu	50

The impurities in the cavity concrete wall were assumed to not self-shield because of their low assumed concentrations, less than 10 ppm, and as such, were assumed to be linearly activated.

For the Monte Carlo portion, there were 800 batches with 10,000 particles per batch. The source used was the one listed in Section 4.11.3. All boration done was with natural boron added directly to the concrete at approximately 0.7 wt. %. (1E+21 atoms nat. B cm^{-3})

6.2 Activation Response

To determine the number of atoms per cubic centimeter, the following equation was used to convert each constituent into an atomic number density per cubic centimeter

$$\text{Number density} = N_i = \frac{\rho_i N_A}{M_i} \quad \frac{\left[\text{g (cm concrete)}^{-3}\right]\left[\text{atoms mol}^{-1}\right]}{\left[\text{g mol}^{-1}\right]} \tag{7}$$

where N_i is the number density of the element, ρ_i is the density of the isotope, N_A is Avogadro's number, and M_i is the molar mass of each element. The impurity level is listed as a ppm level by weight of concrete. Assuming that they contribute negligibly to the weight of the concrete, Table 12 lists the atomic density per isotope of impurity

Table 12: Impurities of interest assumed in concrete

Isotope	Level (ppm wt)	Density (g cm^{-3})	Percent abundance	Molar Mass (g mol^{-1})	Number Density
Co-59	10	8.9	100%	59.93	2.31E+17
Eu-151	1	5.264	47.8%	151.96	4.36E+15
Eu-153	1	5.264	52.2%	151.96	4.76E+15

The basic reaction rate equation is:

$$\text{Rate} = \sigma I N \quad \left[10^{-24}\ \text{cm}^2\right]\left[\text{cm}^{-2}\text{s}^{-1}\right]\left[\text{cm}^{-2}\right] \tag{8}$$

where σ is the microscopic cross-section (barns, b), I is the incident beam intensity (neutrons cm^{-2} s^{-1}), and N is the number of target atoms (atoms cm^{-2}).

The total activity rate for radioisotopes in any material is based on both the creation and disintegration.

$$\frac{dN(t)}{dt} = \sigma I N - \lambda N(t) \tag{9}$$

For all the reactions of interest, it is assumed that they are in saturation, meaning that the time rate of change of the activated material is zero, or:

$$\sigma I N = \lambda N(t) \tag{10}$$

This means that the activity of the activated material is equal to the reaction rate of creation. For all the isotopes of interest, the IAEA limit is 0.1 Bq g^{-1}. (Note these are grams of concrete) Since the density for the concrete is 2.3 g cm^{-3}, we can conclude that the free release limit is 0.23 Bq cm^{-3}. This satisfies the $\lambda N(t)$ term.

On the LHS of Equation 10, in reality we have an integral over the energy range (i.e., a summation in the multigroup case), rather than a single flux value and cross section, represented by the flux weighted response, which in this case was the (n,γ) microscopic cross section for the reactions of interest. This response weighted flux then becomes the σI term in Equation 6.4. N in this case is just the number density of the isotope of interest.

For example, to find the flux in the concrete that corresponds to 100% of the free release limit of 10 ppm ^{60}Co in concrete requires rewriting Equation 4 as follows:

$$\sigma I = \frac{0.23}{(2.31\text{E+17})}(10^{24}) \tag{11}$$

The result of Equation 11 is that *the threshold level for the flux weighted response* is 9.7E+5. The units from for Equation 11 are a combination of Equation 8 and the activity ([s^{-1} cm^{-3}]) which results in s^{-1}. The maximum value over all voxels in the mesh tally for the flux weighted response in IRIS in the concrete is 1.04E+6 ± 23.4% at (188.08, 0, -1157.1) meaning that the activity here is 7% higher than the IAEA limit, well within the expected borating capacity.

6.3 Baseline Results with "standard" (unborated) concrete

To establish a baseline of the activation within the concrete, a simulation was run without any boron in the concrete. The Monaco simulation time was 43.6 hours.

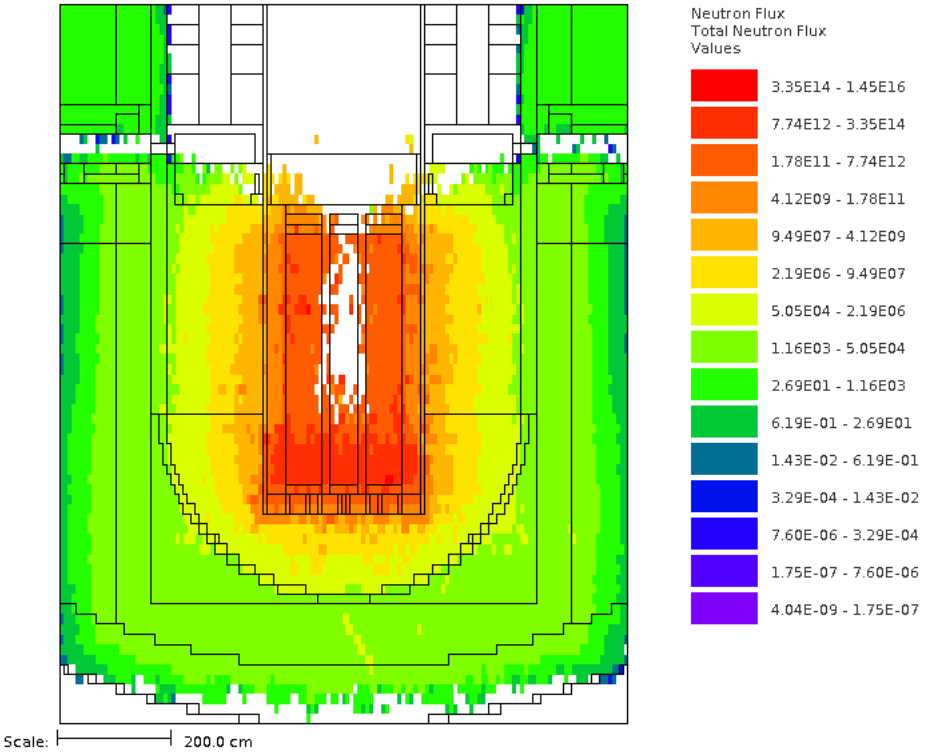

Figure 40: Total flux with no boron

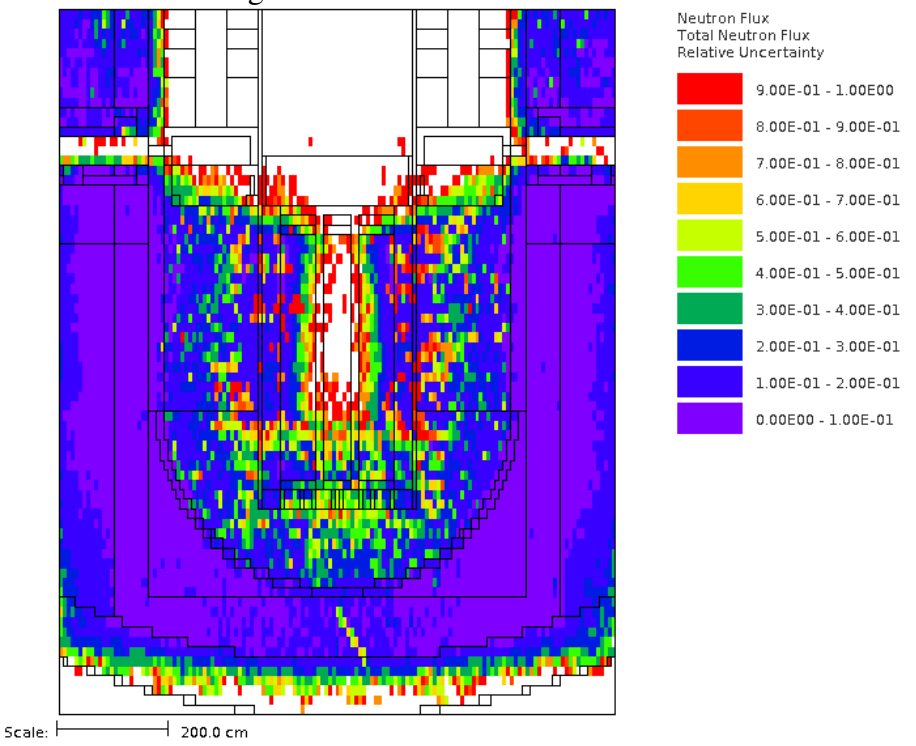

Figure 41: Relative uncertainty for Figure 40

As shown in Figure 40 and Figure 41, the total flux results are very good. The code successfully optimized Monte Carlo simulations for the concrete at the expense of other regions. Uncertainties in the first layer of concrete throughout the pressure vessel cavity are all under 10%, in spite of at least ten orders of magnitude attenuation.

However, the total flux does not tell the whole story. The flux weighted response, discussed in Section 6.2, is the more important value to determine if the concrete will be activated over the IAEA limit. For the $^{59}Co(n,\gamma)^{60}Co$ reaction, at 10 ppm, the level would be exceeded if the flux weighted response in concrete was greater than 9.7E+5 interactions s^{-1}. Figure 42 shows the total response, Figure 43 shows the relative uncertainty of the response, and Figure 44 shows the response with a lower cutoff equal to exceeding the free release limit. Only the distribution within the cavity wall is meaningful.

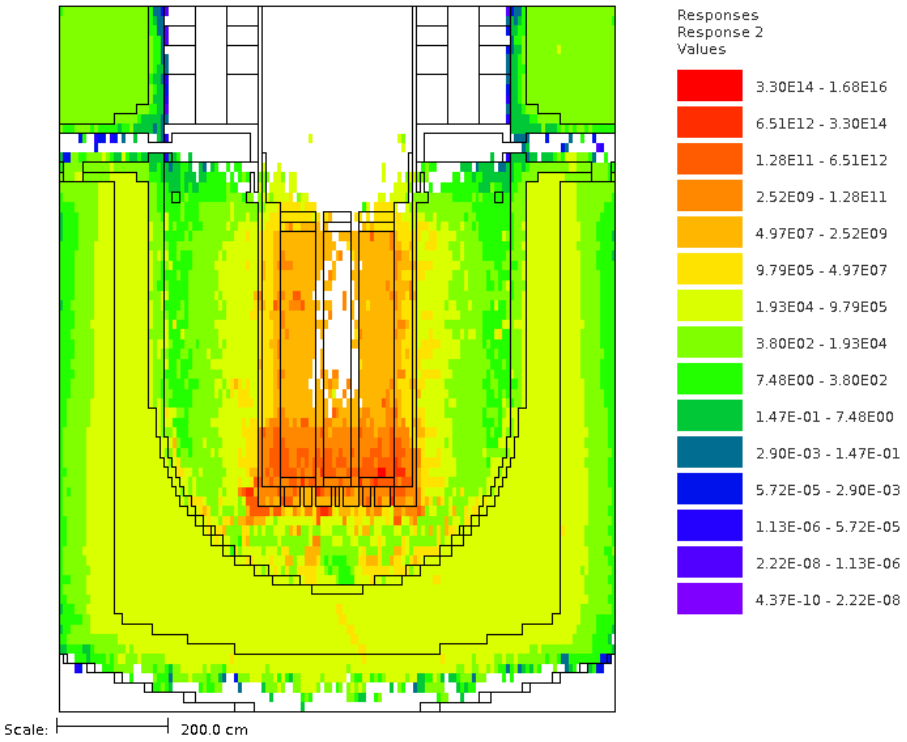

Figure 42: ^{60}Co response

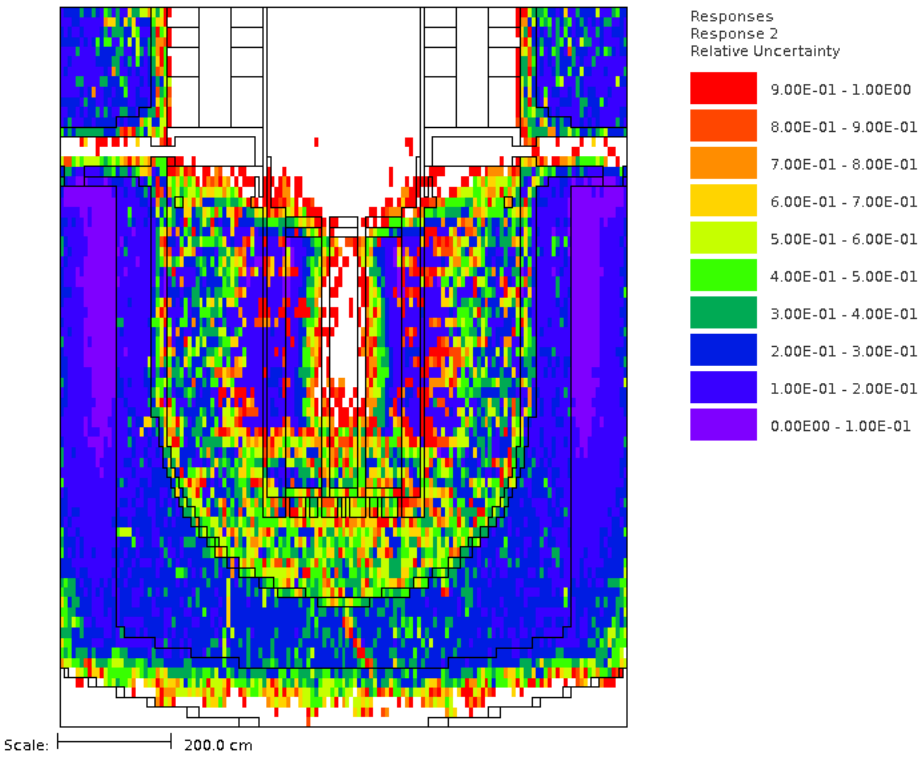

Figure 43: Relative uncertainty for Figure 42

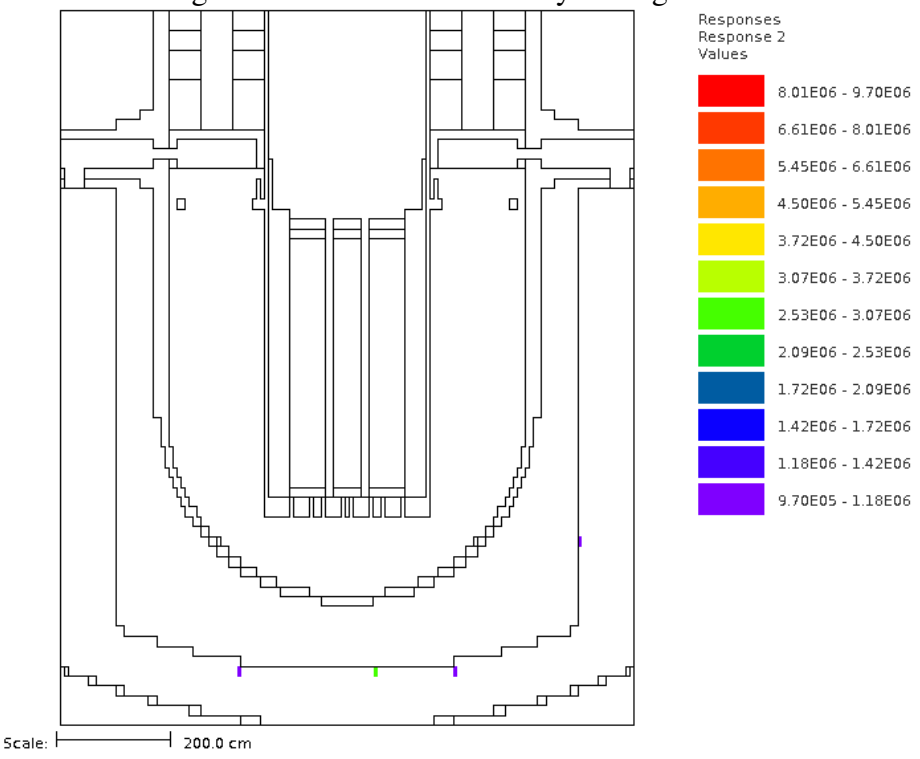

Figure 44: ^{60}Co response above the IAEA clearance

Figure 44 shows that with no boron at 10 ppm ^{59}Co in the concrete under full power, there will be some concrete that is activated above the free release limit. It is primarily contained to the lower cavity where the pressure vessel wall thickness is reduced by one-half. These results are in line with the validation with Burn's model showing that the ^{60}Co activity would be below the limit.[5]

While the results may be within the other models, it is prudent to include a safety factor and present the results. The factor selected was three. Figure 45 shows the results if threshold limit discussed in Section 6.2 was reduced by a factor of three. This could be achieved in a real world scenario by a one-third reduction in the clearance limit or an increase in the flux or impurity content by a factor of three, or may be needed to account for uncertainties in material dimensions and densities, or cross sections.

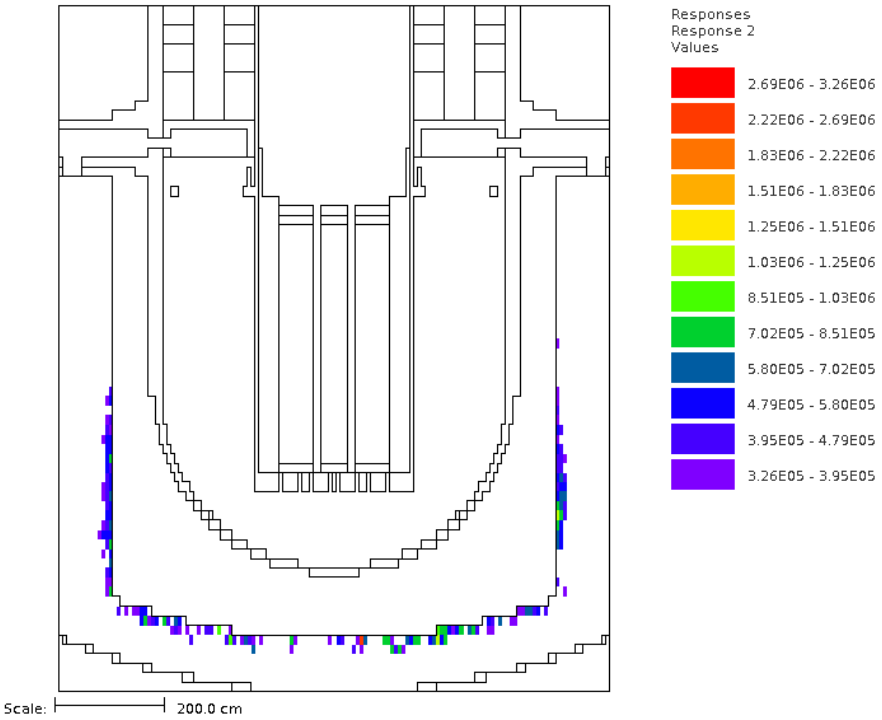

Figure 45: ^{60}Co response above IAEA clearance limit with applied safety factor

Even with the safety factor applied, the total mass of concrete activated is relatively low. It falls in line with expectations; only the fast flux leaving the core is important, and as it strikes the face of the cavity, it is thermalized and captured.

For both europium isotopes, the level assumed in the concrete was 1 ppm of natural europium. This corresponds to a flux weighted response level of 5.2E+7 interactions s^{-1} for ^{152}Eu and 4.8E+7 interactions s^{-1} for ^{154}Eu and the natural europium content is 47.8 at. % ^{151}Eu with the balance ^{153}Eu.

For ^{152}Eu, Figure 46, Figure 47, and Figure 48 show the total response, the response above the clearance, and the response above the clearance with a safety factor of three.

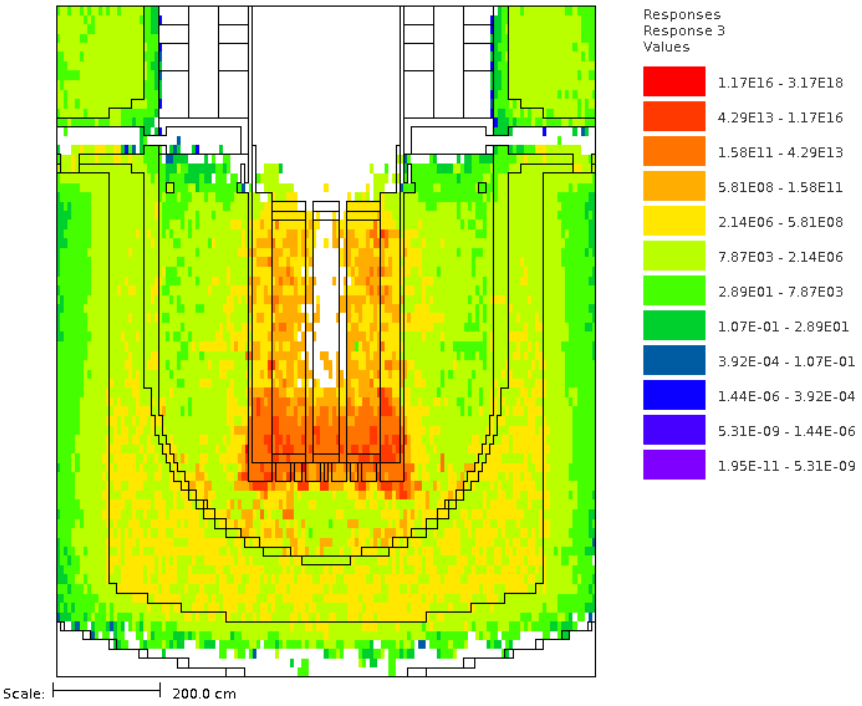

Figure 46: Total ^{152}Eu response with no boron

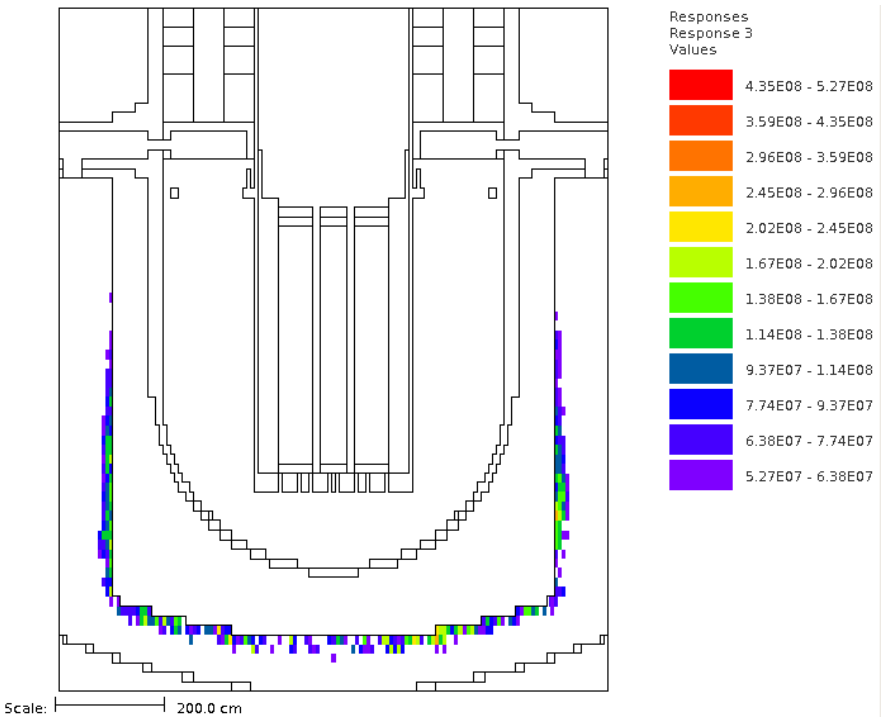

Figure 47: ^{152}Eu response above the IAEA clearance (no boron)

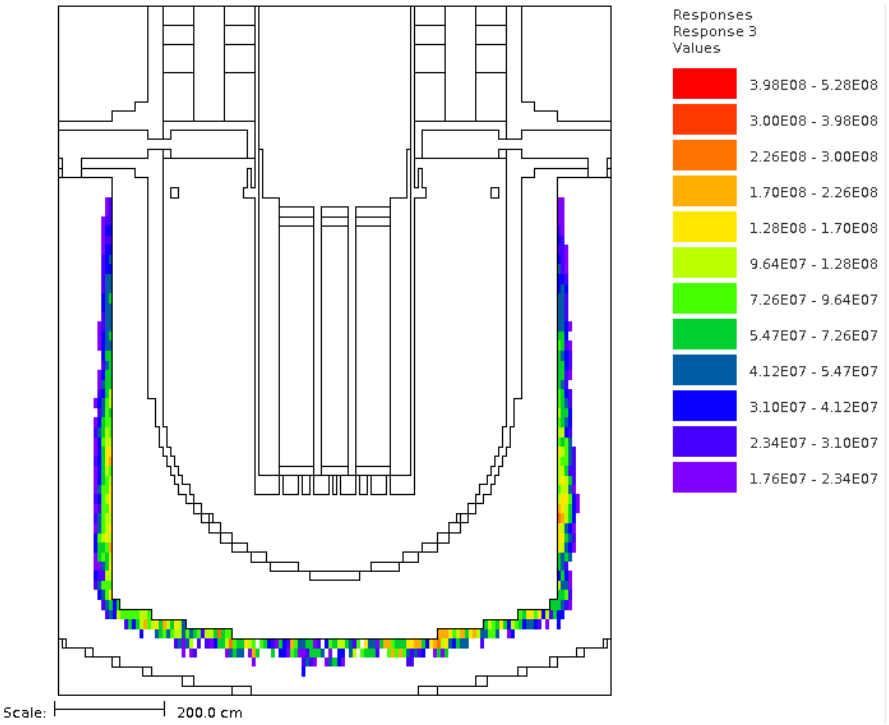

Figure 48: ^{152}Eu response above the clearance with the safety factor (no boron)

^{152}Eu shows more activation than ^{60}Co as expected given that the cross sections for ^{152}Eu are higher and the maximum occurs in a lower energy group. With the safety factor applied, there is a larger volume of activated material.

Figure 49, Figure 50, and Figure 51 show the total response, the response above the clearance, and the response above the clearance with a safety factor of three for ^{154}Eu.

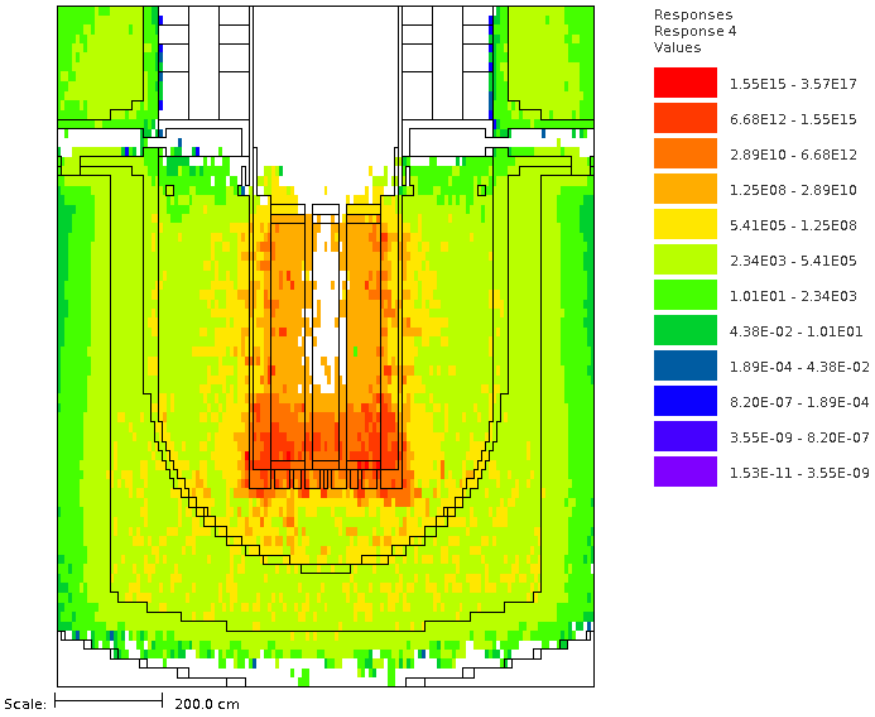

Figure 49: Total ^{154}Eu response with no boron

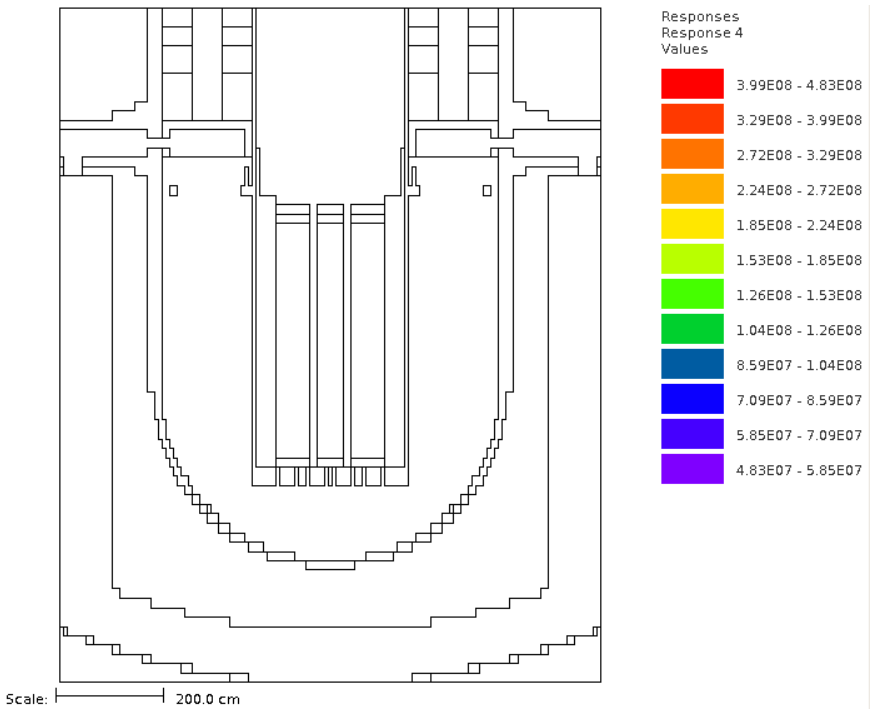

Figure 50: ^{154}Eu response above the IAEA clearance

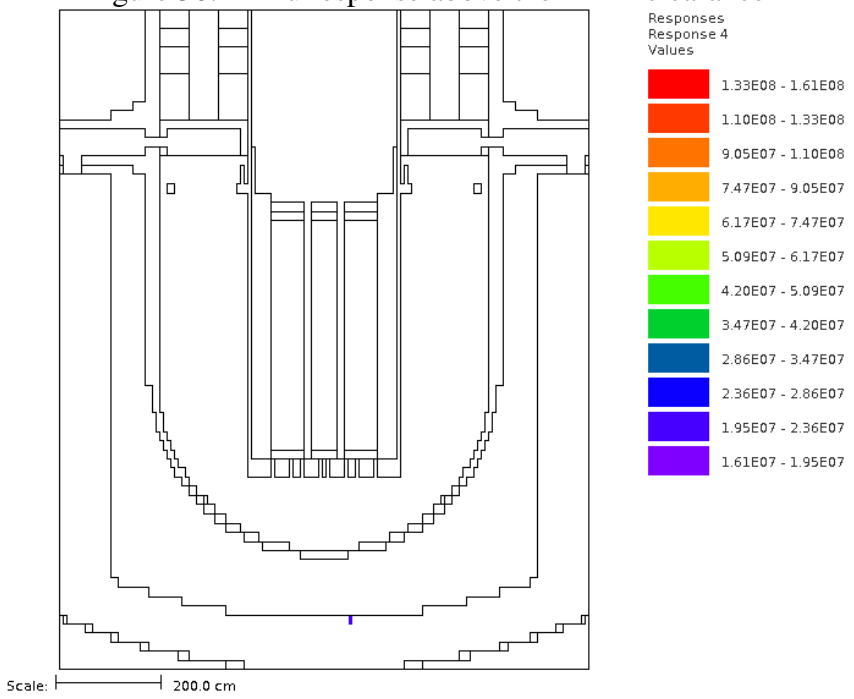

Figure 51: ^{154}Eu response above the clearance with the safety factor (no boron)

As shown, ^{154}Eu is negligible including the safety factor. The single voxel displayed at the bottom is the only indicated activation but with over 70% relative uncertainty it is most likely non-activated as its neighbors which have relative uncertainties under 20%.

6.4 Results with boration

The next simulation performed included boron in the concrete to a level of 0.7 wt. %. This amount of boron was identified as a reasonable level.[30] This level of boron is equivalent to 1E+21 atoms nat. B cm^{-3}. The only change in the model input file was the addition of boron. Figure 6.14 and 6.15 show the total neutron flux within the same volume as before.

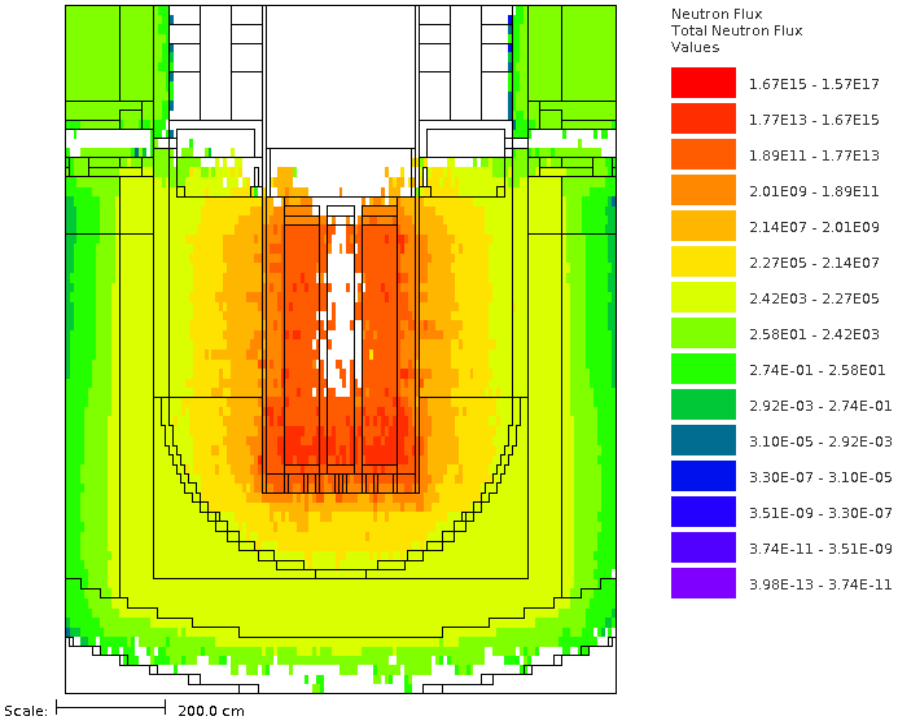

Figure 52: Total flux with boron

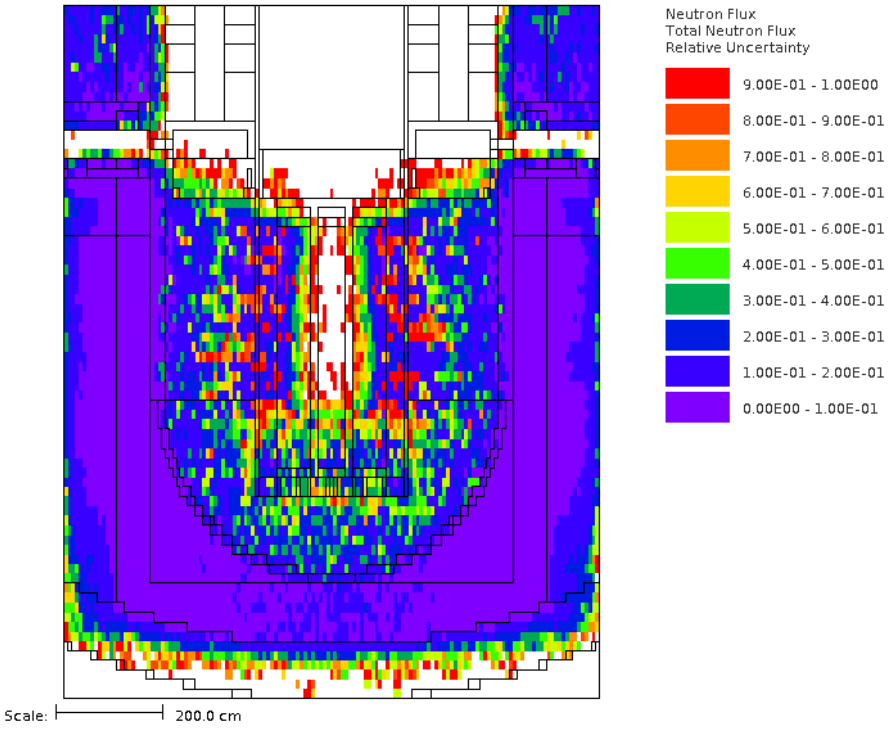

Figure 53: Relative uncertainty for Figure 52

As compared to the simulation with no boron, the simulation with boron already has lower flux in the concrete areas. Figure 54, Figure 55, and Figure 56 show for ^{60}Co the total response, the response above the IAEA clearance and the response above the clearance with a safety factor of three.

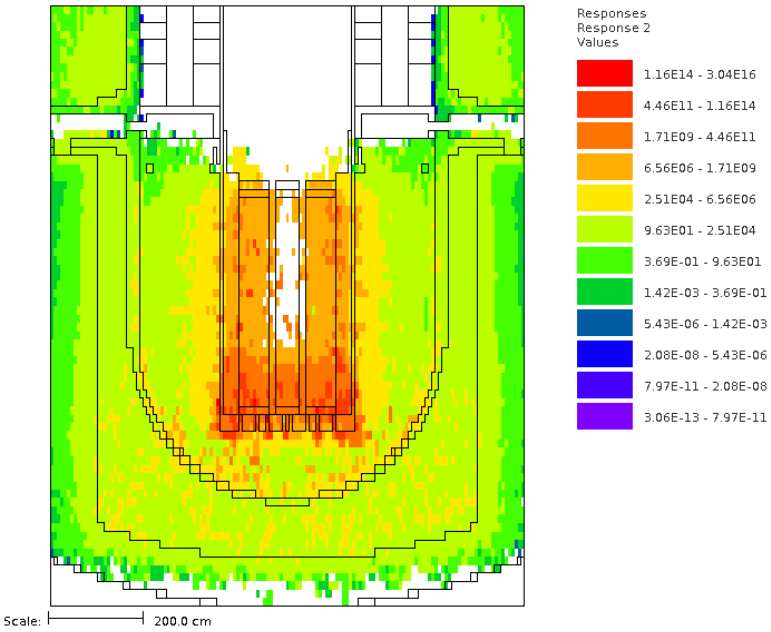

Figure 54: Total ^{60}Co response with boron

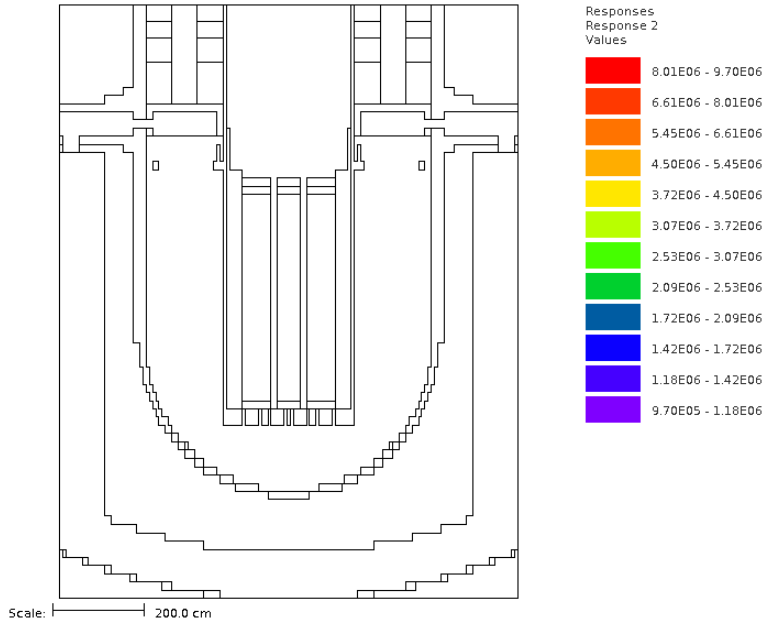

Figure 55: ^{60}Co response above the IAEA clearance with boron

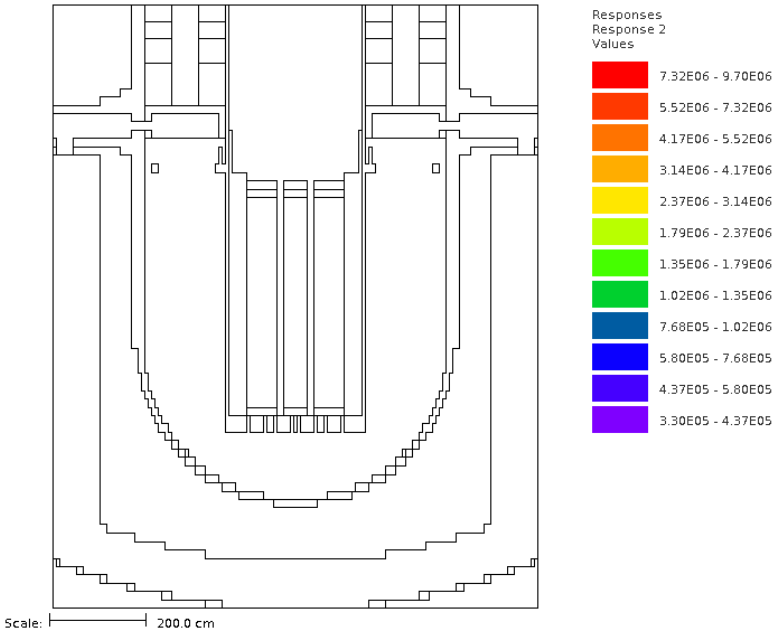

Figure 56: ^{60}Co response above the IAEA clearance with boron and safety factor

The same figures shown for ^{60}Co will be shown for ^{152}Eu. ^{154}Eu will not be shown because as discussed in Section 6.3, its contribution and activation are significantly smaller.

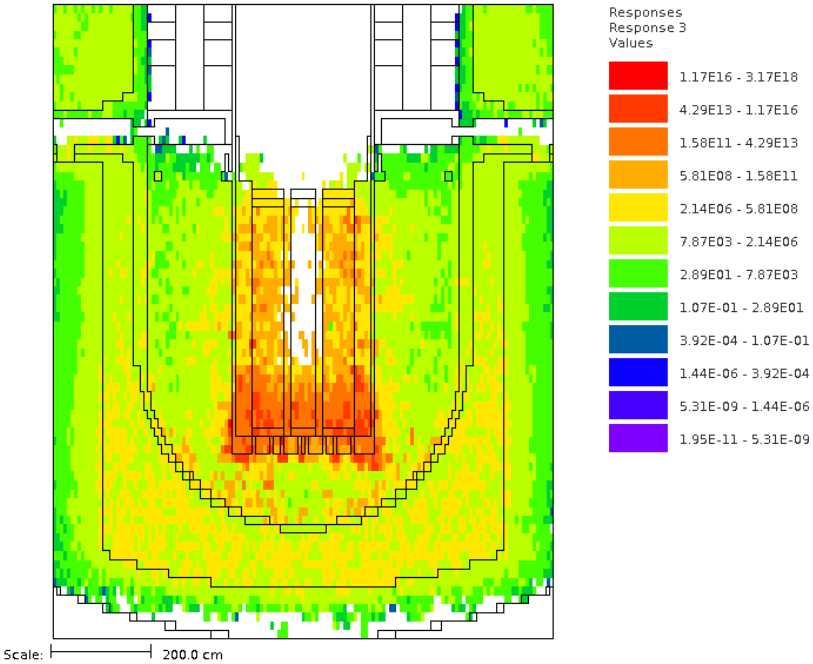

Figure 57: Total ^{152}Eu response

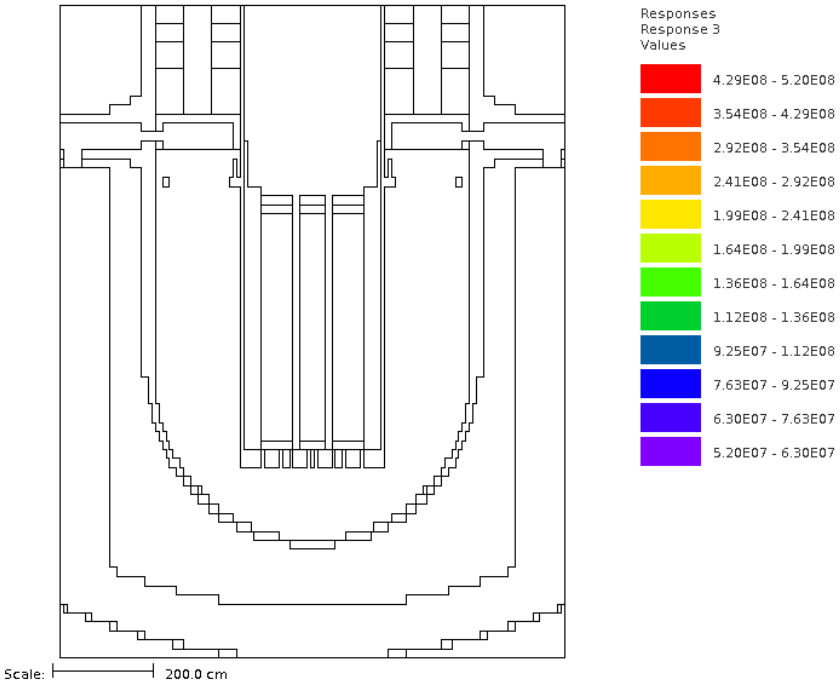

Figure 58: ^{152}Eu response above the IAEA clearance with boron

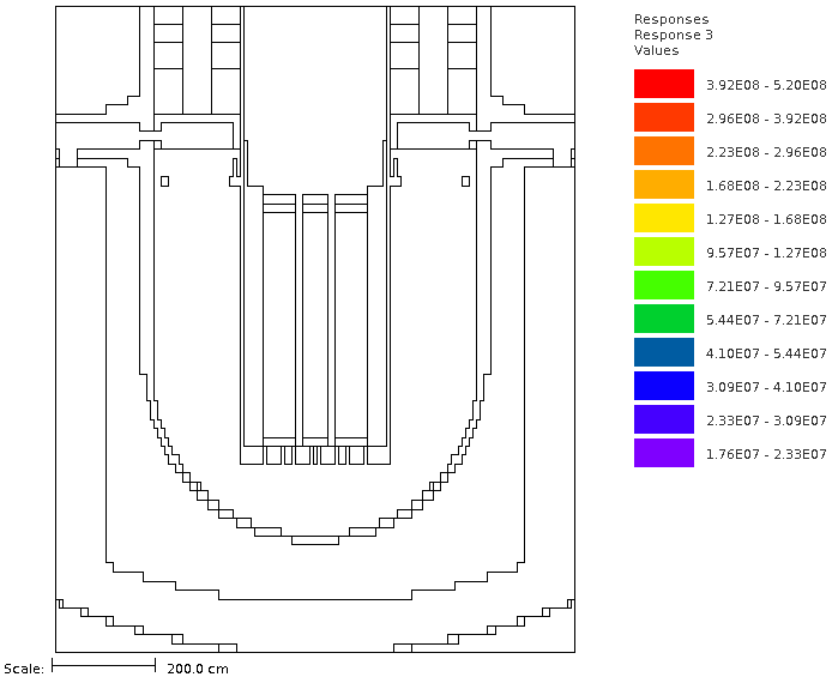

Figure 59: ^{152}Eu response above the IAEA clearance with safety factor and boron

The previous figures show that with an addition of an acceptable amount of natural boron, there is a significant decrease in the activated materials. None of the isotopes of interest are activated above the IAEA clearance limit. But, a figure with no levels does not convey the whole story. Table 13 lists several points around the cavity wall with their location and responses for the different isotopes.

Table 13: List of several points and responses

Isotope	Location	Response without boron	Response with boron	Response limit with safety factor
^{60}Co	Core midplane	2.71E+05	1.94E+04	3.26E+05
	Cavity maximum	8.40E+05	2.54E+04	3.26E+05
	Directly under PV	3.20E+05	1.90E+04	3.26E+05
^{152}Eu	Core midplane	1.80E+08	2.53E+06	1.76E+07
	Cavity maximum	1.93E+08	1.10E+06	1.76E+07
	Directly under PV	6.68E+07	2.83E+06	1.76E+07

From Table 13, the values are not zero; they are just below the response when natural boron is added even with the extra safety factor included.

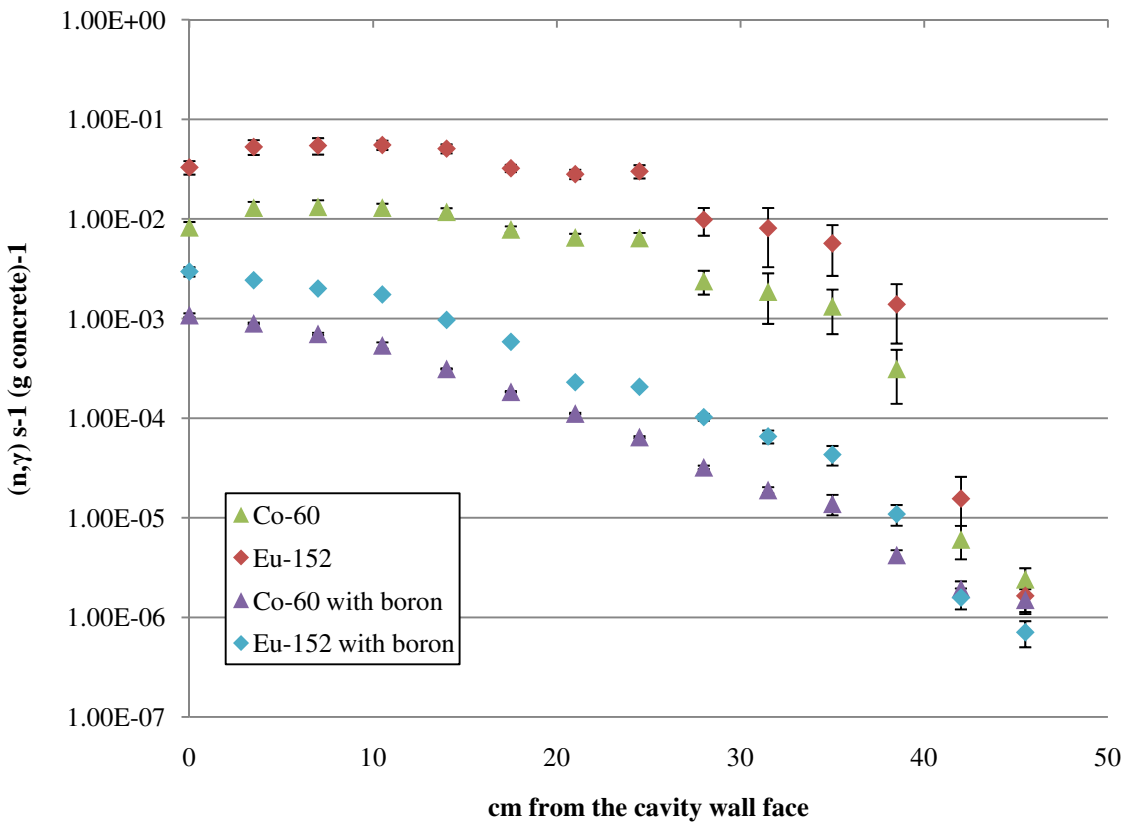

Figure 60: Activation by depth

Figure 60 shows the reaction rates of activation by depth for the core mid-plane of the cavity wall. The reaction rate parameters are based on the individual (n, γ) reaction for each isotope with the result shown in the legend. The reaction rates are per gram of concrete per second. Comparison of results with and without boron shows the expected decrease in impurity activation with boron in the cavity wall. Error bars shown are for 1σ. Results are shown every 3.5 cm from the cavity wall face mesh up to 45.5 cm deep. Results beyond 28 cm have much higher errors and are shown for the trends, not necessarily their absolute values. The results shown in Figure 60 are consistent with those reported in Reference 5 with a maximum moving from inside the wall without the boron to the face of the cavity with the boron.

CHAPTER 7

CONCLUSIONS

A detailed shielding analysis of the IRIS reactor was performed. The purpose of this work was to determine if the activation of the reactor vessel cavity concrete wall could be reduced below the free release threshold for the benefit of lowered decommission costs and reduction of dose. Minimizing the quantity of activated materials reduces the cost of disposal. Guided by the IAEA free release limits ("clearance limits"), the upper limit of activation based on assumed impurity content is known of certain isotopes. A carefully constructed model of the IRIS reactor was developed to analyze the activation of the structural concrete using the MAVRIC sequence within the SCALE package. This software greatly simplified obtaining results by generating automatic variance reduction parameters using the CADIS/FW-CADIS method which in turn sped up the simulation. The (n,γ) reaction cross sections were used to make an accurate assessment of the activated materials. The baseline was established for the cavity concrete wall constructed of ordinary concrete. In this case, some fraction of the concrete would be activated above the clearance limit. Next, the analysis examined the impact of borating the cavity concrete wall immediately surrounding the reactor vessel. A known quantity of natural boron was added to the concrete in a homogenous fashion and the simulation rerun to determine the net effects of the boron capturing the thermal neutrons in an (n,α) reaction, rather than the

isotopes of ^{59}Co, ^{151}Eu, and ^{153}Eu capturing them and forming radioactive gamma-emitting isotopes.

Based on the results in chapter six, it is clear that boration makes a considerable difference (reduction) in the activation level of the concrete in the vessel cavity. One particularly important point is that this was with natural boron directly added to the concrete. Normally, boron would be added as boric acid in water, or borogypsum or colemanite as discussed in chapter two. Boron added in that manner would be the preferred way.

The primary issue with adding boron would be the amount required to completely and uniformly borate the entire cavity wall. At 0.7 wt. % it would be over six metric tons of boron. If the boration would be achieved by using borated aggregate, there could be very high shipping costs associated with bringing in the aggregate rather than using local materials, and direct addition of boron would be preferred in that case.

Another issue is where to borate within the cavity. Based on the results in chapter 6, only a small fraction of the concrete mass, the face of the cavity, needs to be borated as that is the location of the maximum thermal flux. However, this can be problematic especially if a continuous pour is required for construction.

The most economical choice would be to analyze the local building materials adding boron as required to offset the impurities within the local aggregate. This will allow IRIS to remain below the clearance levels while minimizing the costs associated with the construction. The cost to decommission the concrete if not borated would be approximately 1000 times greater if it is above the clearance limit than if it is below the limit. As shown, none of the isotopes investigated exceed the clearance limit if the concrete is borated.

It is meaningful to determine what the maximum impurity content would need to be to exceed the limit with the boration quantity assumed. Using the location for the maximum response, it is not difficult to work out the maximum concentration for any of the isotopes that are main contributors to activity. The critical impurity level for each one individually (i.e., producing 100% of the IAEA limit by itself) is listed in Table 14.

Table 14: Maximum impurity content resulting in activation still below clearance limit

Isotope	Maximum (ppm wt)
Co-59	31
Eu-151	5
Eu-153	88

There is quite a margin for ^{153}Eu, and a factor of five increase would be allowable for ^{151}Eu. Since both of these europium isotopes are naturally occurring and about half each, the maximum for natural europium would be a maximum of 10 ppm by weight or a factor of 10 higher than was considered for this analysis. However, for ^{59}Co, there is only a factor of three margin. Most of the cobalt in concrete would be due to the rebar, not in the aggregate or cement. For europium, the case could almost be closed; the CRC Handbook lists its natural crustal abundance as only 2 ppm. For cobalt, the natural crustal abundance is 25 ppm.[31] Given that these values can vary widely depending on the location, they cannot be taken as absolutes but more of a guide that cobalt will most likely be the driver of the activation. These impurity levels are based on best-estimate results. It is prudent to additionally include a factor (margin) that accounts for cross section uncertainties and uncertainties in the model itself (tolerances, exact vs. as-build dimensions, densities, etc.) This was the primary impetus for the additional figures with the safety factor in chapter 6.

One important point to consider in this analysis is that the assumption throughout was that the activation level used was the level that would occur immediately after shutdown running for 60 years a full power. Decommissioning is not a fast processes and most likely there would be a period of years before work started on the plant dismantling. This is to the advantage of the reactor owner. The half-life for ^{60}Co is 5.27 years. An additional factor of two can be gained just by waiting for one half-life meaning that the ^{59}Co content with boration could be as high as 60 ppm in the aggregate and cement.

For the IRIS reactor, given its unique design features, borating the cavity concrete is recommended for the ability to reduce the overall activation of materials (in particular the cavity concrete wall) below the free release limit. This fulfills the goal of improving the plant characteristics compared to the currently operating fleet with respect to activation, dose, and decommissioning cost.

CHAPTER 8

FUTURE WORK

Future work beyond the scope of this thesis would include considering the entire building and all the possible activation beyond the pressure vessel cavity as a way to minimize the dose to the control room and other accessible areas both in operation and during maintenance. Also, it would extend the analysis to coupled neutron-gamma analysis. The analysis may be also extended to decommissioning activities and the related dose reduction. Finally, the full building model will enable performing the severe accident analysis based on the appropriately assumed source term.

Such analyses will be facilitated by the next version of the MAVRIC code, which is expected to contain the ability to read a space-dependent source distribution rather than the uniform one used here. That would contribute to reducing some of the approximations and resulting inaccuracies in the calculations, bringing them more in line with other work performed on IRIS.[5, 11] Parallel versions of the deterministic (Denovo) and Monte Carlo (Monaco) codes would also allow one to generate better acceleration parameters and then faster (in real time) perform Monte Carlo simulations. The new versions will make analyzing the entire building with a fine deterministic mesh possible to evaluate the dose everywhere.

An investigation into the concrete including the rebar material would be needed to be done. The rebar is normally plain steel that would contain levels of ^{59}Co in the hundreds of ppm

range by weight. This could be a significant source of activation if the rebar is close to the surface of the cavity wall which would reduce the amount of concrete to thermalize the flux and boron to capture the neutrons.

APPENDIX A: IAEA Data

The following data is taken from the IAEA Safety Standards Series: Applications of the Concepts of Exclusion, Exemption and Clearance used to determine if material can be discarded as free release material that is if the weighted activity per isotope is below the level. The limit is determined by the following equation:

$$\sum_{i=1}^{n} \frac{C_i}{(\text{activity concentration})_i} \leq 1 \qquad \text{(A.1)}$$

where C_i is the concentration in Bq g^{-1} of the ith radionuclide, $(\text{activity concentration})_i$ is the value of the activity concentration for the ith radionuclide and n is the number of radionuclides present. This means that if one radionuclide is at 50% of the clearance limit, there could be another radionuclide at 50% before the material is considered non free release.[27] Table A.1 from the IAEA guidelines shows the maximum bulk activity limits. Isotopes considered in this thesis are highlighted in red.

Table A.1: Values of Activity Concentration for Radionuclides of Artificial Origin in Bulk

Radio-nuclide	Activity concen-tration (Bq/g)		Radio-nuclide	Activity concen-tration (Bq/g)		Radio-nuclide	Activity concen-tration (Bq/g)	
H-3	100		Mn-56	10	*	Se-75	1	
Be-7	10		Fe-52	10	*	Br-82	1	
C-14	1		Fe-55	1000		Rb-86	100	
F-18	10	*	Fe-59	1		Sr-85	1	
Na-22	0.1		Co-55	10	*	Sr-85m	100	*
Na-24	1	*	Co-56	0.1		Sr-87m	100	*
Si-31	1000	*	Co-57	1		Sr-89	1000	
P-32	1000		Co-58	1		Sr-90	1	
P-33	1000		Co-58m	10000	*	Sr-91	10	*
S-35	100		Co-60	0.1		Sr-92	10	*
Cl-36	1		Co-60m	1000	*	Y-90	1000	
Cl-38	10	*	Co-61	100	*	Y-91	100	
K-42	100		Co-62m	10	*	Y-91m	100	*
K-43	10	*	Ni-59	100		Y-92	100	*
Ca-45	100		Ni-63	100		Y-93	100	*
Ca-47	10		Ni-65	10	*	Zr-93	10	*
Sc-46	0.1		Cu-64	100	*	Zr-95	1	
Sc-47	100		Zn-65	0.1		Zr-97	10	*
Sc-48	1		Zn-69	1000	*	Nb-93m	10	
V-48	1		Zn-69m	10	*	Nb-94	0.1	
Cr-51	100		Ga-72	10	*	Nb-95	1	
Mn-51	10	*	Ge-71	10000		Nb-97	10	*
Mn-52	1		As-73	1000		Nb-98	10	*
Mn-52m	10	*	As-74	10	*	Mo-90	10	*
Mn-53	100		As-76	10	*	Mo-93	10	
Mn-54	0.1		As-77	1000		Mo-99	10	

Table A.1 Continued

Radio-nuclide	Activity concen-tration (Bq/g)		Radio-nuclide	Activity concen-tration (Bq/g)		Radio-nuclide	Activity concen-tration (Bq/g)	
Mo-101	10	*	Sn-125	10		Cs-129	10	
Tc-96	1		Sb-122	10		Cs-131	1000	
Tc-96m	1000	*	Sb-124	1		Cs-132	10	
Tc-97	10		Sb-125	0.1		Cs-134	0.1	
Tc-97m	100		Te-123m	1		Cs-134m	1000	*
Tc-99	1		Te-125m	1000		Cs-135	100	
Tc-99m	100	*	Te-127	1000		Cs-136	1	
Ru-97	10		Te-127m	10		Cs-137	0.1	
Ru-103	1		Te-129	100	*	Cs-138	10	*
Ru-105	10	*	Te-129m	10		Ba-131	10	
Ru-106	0.1		Te-131	100	*	Ba-140	1	
Rh-103m	10000	*	Te-131m	10		La-140	1	
Rh-105	100		Te-132	1		Ce-139	1	
Pd-103	1000		Te-133	10	*	Ce-141	100	
Pd-109	100		Te-133m	10	*	Ce-143	10	
Ag-105	1		Te-134	10	*	Ce-144	10	
Ag-110m	0.1		I-123	100		Pr-142	100	*
Ag-111	100		I-125	100		Pr-143	1000	
Cd-109	1		I-126	10		Nd-147	100	
Cd-115	10		I-129	0.01		Nd-149	100	*
Cd-115m	100		I-130	10	*	Pm-147	1000	
In-111	10		I-131	10		Pm-149	1000	
In-113m	100	*	I-132	10	*	Sm-151	1000	
In-114m	10		I-133	10	*	Sm-153	100	
In-115m	100	*	I-134	10	*	Eu-152	0.1	
Sn-113	1		I-135	10	*	Eu-152m	100	*

Table A.1 Continued

Radio-nuclide	Activity concen-tration (Bq/g)		Radio-nuclide	Activity concen-tration (Bq/g)		Radio-nuclide	Activity concen-tration (Bq/g)	
Eu-154	0.1		Ir-192	1		Pa-230	10	
Eu-155	1		Ir-194	100	*	Pa-233	10	
Gd-153	10		Pt-191	10		U-230	10	
Gd-159	100	*	Pt-193m	1000		U-231	100	
Tb-160	1		Pt-197	1000	*	U-232	0.1	
Dy-165	1000	*	Pt-197m	100	*	U-233	1	
Dy-166	100		Au-198	10		U-236	10	
Ho-166	100		Au-199	100		U-237	100	
Er-169	1000		Hg-197	100		U-239	100	*
Er-171	100	*	Hg-197m	100		U-240	100	*
Tm-170	100		Hg-203	10		Np-237	1	
Tm-171	1000		Tl-200	10		Np-239	100	
Yb-175	100		Tl-201	100		Np-240	10	*
Lu-177	100		Tl-202	10		Pu-234	100	*
Hf-181	1		Tl-204	1		Pu-235	100	*
Ta-182	0.1		Pb-203	10		Pu-236	1	
W-181	10		Bi-206	1		Pu-237	100	
W-185	1000		Bi-207	0.1		Pu-238	0.1	
W-187	10		Po-203	10	*	Pu-239	0.1	
Re-186	1000		Po-205	10	*	Pu-240	0.1	
Re-188	100	*	Po-207	10	*	Pu-241	10	
Os-185	1		At-211	1000		Pu-242	0.1	
Os-191	100		Ra-225	10		Pu-243	1000	*
Os-191m	1000	*	Ra-227	100		Pu-244	0.1	
Os-193	100		Th-226	1000		Am-241	0.1	
Ir-190	1		Th-229	0.1		Am-242	1000	*

APPENDIX B: Activation Cross-Sections

Table B.1: List of microscopic cross sections used for activation

Neutron energy upper bound (eV)	^{59}Co (n,γ)^{60}Co (b)	^{151}Eu (n,γ)^{152}Eu (b)	^{153}Eu(n,γ)^{154}Eu (b)
2.00E+07	2.55E-04	1.09E-03	2.14E-04
1.96E+07	3.01E-04	1.05E-03	3.23E-04
1.73E+07	4.33E-04	1.01E-03	4.63E-04
1.69E+07	5.11E-04	1.00E-03	5.27E-04
1.65E+07	6.33E-04	9.79E-04	6.31E-04
1.57E+07	7.90E-04	9.06E-04	7.94E-04
1.49E+07	8.63E-04	8.44E-04	9.11E-04
1.46E+07	8.81E-04	8.04E-04	9.83E-04
1.42E+07	8.96E-04	7.61E-04	1.05E-03
1.38E+07	8.83E-04	7.08E-04	1.13E-03
1.35E+07	8.57E-04	6.28E-04	1.23E-03
1.28E+07	8.18E-04	5.48E-04	1.33E-03
1.25E+07	7.87E-04	5.00E-04	1.38E-03
1.22E+07	7.45E-04	4.37E-04	1.46E-03
1.16E+07	7.00E-04	3.68E-04	1.60E-03
1.11E+07	6.59E-04	3.28E-04	1.86E-03
1.05E+07	6.19E-04	3.10E-04	2.18E-03
1.00E+07	6.13E-04	3.15E-04	2.55E-03
9.51E+06	6.37E-04	3.40E-04	2.98E-03
9.05E+06	6.59E-04	4.19E-04	3.49E-03
8.61E+06	6.81E-04	5.78E-04	4.13E-03
8.19E+06	7.09E-04	7.57E-04	4.99E-03
7.79E+06	7.72E-04	1.02E-03	6.46E-03
7.41E+06	8.37E-04	1.37E-03	7.93E-03
7.05E+06	8.98E-04	1.82E-03	9.73E-03
6.70E+06	9.37E-04	2.20E-03	1.13E-02
6.59E+06	9.66E-04	2.51E-03	1.24E-02
6.38E+06	1.01E-03	3.17E-03	1.43E-02
6.07E+06	1.07E-03	4.12E-03	1.70E-02
5.77E+06	1.14E-03	5.38E-03	2.10E-02
5.49E+06	1.21E-03	7.12E-03	2.48E-02
5.22E+06	1.28E-03	9.27E-03	2.84E-02

Neutron energy upper bound (eV)	^{59}Co (n,γ)^{60}Co (b)	^{151}Eu (n,γ)^{152}Eu (b)	^{153}Eu(n,γ)^{154}Eu (b)
4.97E+06	1.36E-03	1.19E-02	3.29E-02
4.72E+06	1.44E-03	1.53E-02	3.76E-02
4.49E+06	1.56E-03	2.31E-02	4.45E-02
4.07E+06	1.73E-03	3.61E-02	5.40E-02
3.68E+06	1.95E-03	4.91E-02	6.48E-02
3.33E+06	2.10E-03	6.29E-02	7.22E-02
3.17E+06	2.20E-03	7.23E-02	7.69E-02
3.01E+06	2.29E-03	8.26E-02	8.19E-02
2.87E+06	2.39E-03	9.41E-02	8.75E-02
2.73E+06	2.49E-03	1.06E-01	9.28E-02
2.59E+06	2.58E-03	1.21E-01	9.79E-02
2.47E+06	2.68E-03	1.33E-01	1.03E-01
2.39E+06	2.74E-03	1.39E-01	1.06E-01
2.37E+06	2.76E-03	1.42E-01	1.07E-01
2.35E+06	2.79E-03	1.45E-01	1.09E-01
2.31E+06	2.85E-03	1.52E-01	1.12E-01
2.23E+06	2.96E-03	1.63E-01	1.19E-01
2.12E+06	3.07E-03	1.77E-01	1.27E-01
2.02E+06	3.21E-03	1.91E-01	1.35E-01
1.92E+06	3.39E-03	2.04E-01	1.45E-01
1.83E+06	3.56E-03	2.18E-01	1.55E-01
1.74E+06	3.72E-03	2.32E-01	1.66E-01
1.65E+06	3.89E-03	2.45E-01	1.78E-01
1.57E+06	4.16E-03	2.59E-01	1.90E-01
1.50E+06	4.45E-03	2.72E-01	1.97E-01
1.42E+06	4.77E-03	2.85E-01	2.02E-01
1.35E+06	5.22E-03	2.98E-01	2.07E-01
1.29E+06	5.67E-03	3.11E-01	2.11E-01
1.22E+06	6.06E-03	3.23E-01	2.16E-01
1.16E+06	6.33E-03	3.36E-01	2.20E-01
1.11E+06	6.47E-03	3.54E-01	2.25E-01
1.00E+06	6.44E-03	3.71E-01	2.35E-01
9.62E+05	6.44E-03	3.84E-01	2.52E-01
9.07E+05	6.45E-03	3.98E-01	2.70E-01
8.63E+05	6.48E-03	4.10E-01	2.87E-01
8.21E+05	6.51E-03	4.22E-01	3.03E-01
7.81E+05	6.56E-03	4.40E-01	3.18E-01
7.43E+05	6.62E-03	4.59E-01	3.32E-01
7.07E+05	6.68E-03	4.76E-01	3.43E-01

Neutron energy upper bound (eV)	^{59}Co (n,γ)^{60}Co (b)	^{151}Eu (n,γ)^{152}Eu (b)	^{153}Eu(n,γ)^{154}Eu (b)
6.72E+05	6.77E-03	4.92E-01	3.49E-01
6.39E+05	6.85E-03	5.08E-01	3.55E-01
6.08E+05	6.94E-03	5.23E-01	3.62E-01
5.78E+05	7.07E-03	5.37E-01	3.69E-01
5.50E+05	7.19E-03	5.51E-01	3.77E-01
5.23E+05	7.30E-03	5.64E-01	3.86E-01
4.98E+05	7.54E-03	5.98E-01	4.02E-01
4.50E+05	7.87E-03	6.51E-01	4.31E-01
4.08E+05	8.11E-03	6.96E-01	4.58E-01
3.88E+05	8.32E-03	7.27E-01	4.75E-01
3.69E+05	8.65E-03	7.81E-01	5.01E-01
3.34E+05	9.15E-03	8.81E-01	5.46E-01
3.02E+05	9.40E-03	9.26E-01	5.71E-01
2.98E+05	9.45E-03	9.34E-01	5.75E-01
2.97E+05	9.49E-03	9.41E-01	5.77E-01
2.95E+05	9.60E-03	9.58E-01	5.84E-01
2.87E+05	9.84E-03	9.96E-01	5.97E-01
2.73E+05	1.03E-02	1.07E+00	6.24E-01
2.47E+05	1.08E-02	1.14E+00	6.55E-01
2.35E+05	1.12E-02	1.19E+00	6.80E-01
2.24E+05	1.15E-02	1.23E+00	7.06E-01
2.13E+05	1.19E-02	1.27E+00	7.34E-01
2.02E+05	1.23E-02	1.31E+00	7.62E-01
1.93E+05	1.28E-02	1.35E+00	7.91E-01
1.83E+05	1.33E-02	1.39E+00	8.22E-01
1.74E+05	1.38E-02	1.42E+00	8.53E-01
1.66E+05	1.42E-02	1.46E+00	8.86E-01
1.58E+05	1.47E-02	1.49E+00	9.21E-01
1.50E+05	1.52E-02	1.52E+00	9.56E-01
1.43E+05	1.59E-02	1.55E+00	9.93E-01
1.36E+05	1.67E-02	1.57E+00	1.03E+00
1.29E+05	1.73E-02	1.60E+00	1.07E+00
1.23E+05	1.79E-02	1.63E+00	1.11E+00
1.17E+05	1.85E-02	1.68E+00	1.16E+00
1.11E+05	1.87E-02	1.73E+00	1.25E+00
9.80E+04	1.39E-02	1.85E+00	2.08E+00
8.65E+04	1.30E-02	1.94E+00	2.32E+00
8.25E+04	7.78E-03	2.00E+00	1.54E+00
7.95E+04	1.48E-02	2.08E+00	1.58E+00

Neutron energy upper bound (eV)	^{59}Co (n,γ)^{60}Co (b)	^{151}Eu (n,γ)^{152}Eu (b)	^{153}Eu(n,γ)^{154}Eu (b)
7.20E+04	1.17E-02	2.20E+00	1.62E+00
6.74E+04	1.55E-02	2.30E+00	1.69E+00
5.66E+04	1.48E-02	2.45E+00	1.78E+00
5.25E+04	1.59E-02	2.63E+00	1.87E+00
4.63E+04	7.75E-03	2.89E+00	2.00E+00
4.09E+04	1.59E-02	3.14E+00	2.15E+00
3.43E+04	2.57E-02	3.39E+00	2.30E+00
3.18E+04	2.47E-02	3.59E+00	2.41E+00
2.85E+04	2.49E-02	3.78E+00	2.54E+00
2.70E+04	6.42E-03	3.95E+00	2.63E+00
2.61E+04	6.00E-02	3.99E+00	2.68E+00
2.48E+04	5.13E-02	4.14E+00	2.74E+00
2.42E+04	1.40E-02	4.46E+00	2.84E+00
2.36E+04	1.91E-02	4.49E+00	2.86E+00
2.19E+04	1.76E-02	5.09E+00	3.07E+00
1.93E+04	2.68E-02	5.63E+00	3.58E+00
1.50E+04	2.85E-02	6.53E+00	4.23E+00
1.17E+04	2.65E-02	7.16E+00	4.58E+00
1.06E+04	6.10E-02	7.65E+00	4.87E+00
9.12E+03	3.94E-02	8.57E+00	5.54E+00
7.10E+03	6.66E-02	1.00E+01	6.54E+00
5.53E+03	3.35E-01	1.15E+01	7.79E+00
4.31E+03	1.58E-01	1.33E+01	8.77E+00
3.71E+03	3.98E-02	1.27E+01	9.51E+00
3.35E+03	2.93E-02	1.28E+01	1.01E+01
3.04E+03	1.64E-01	1.32E+01	1.06E+01
2.75E+03	2.28E-02	1.65E+01	1.10E+01
2.61E+03	2.18E-02	1.66E+01	1.12E+01
2.49E+03	7.45E-02	1.70E+01	1.16E+01
2.25E+03	2.10E-02	1.75E+01	1.20E+01
2.03E+03	2.16E-02	1.88E+01	1.33E+01
1.58E+03	5.00E-02	2.10E+01	1.53E+01
1.23E+03	2.91E-02	2.34E+01	1.70E+01
9.61E+02	3.61E-02	2.58E+01	1.92E+01
7.49E+02	4.72E-02	2.81E+01	2.16E+01
5.83E+02	6.67E-02	3.08E+01	2.40E+01
4.54E+02	1.07E-01	3.37E+01	2.77E+01
3.54E+02	2.04E-01	3.80E+01	3.21E+01
2.75E+02	5.10E-01	4.42E+01	3.81E+01

Neutron energy upper bound (eV)	^{59}Co (n,γ)^{60}Co (b)	^{151}Eu (n,γ)^{152}Eu (b)	^{153}Eu(n,γ)^{154}Eu (b)
2.14E+02	1.99E+00	5.83E+01	4.91E+01
1.67E+02	2.24E+01	8.56E+01	6.94E+01
1.30E+02	2.25E+01	9.17E+01	7.03E+01
1.01E+02	5.00E+00	9.50E+01	6.09E+01
7.89E+01	2.68E+00	5.41E+01	4.51E+01
6.14E+01	2.00E+00	9.24E+01	8.53E+01
4.79E+01	1.74E+00	1.24E+02	6.80E+01
3.73E+01	1.66E+00	7.83E+01	3.93E+01
2.90E+01	1.66E+00	8.36E+01	3.30E+01
2.26E+01	1.73E+00	1.04E+02	1.39E+02
1.76E+01	1.83E+00	5.06E+01	3.50E+01
1.37E+01	1.98E+00	1.16E+02	8.44E+01
1.07E+01	2.17E+00	9.98E+01	8.37E+01
8.32E+00	2.39E+00	1.21E+02	1.91E+01
6.48E+00	2.65E+00	9.88E+01	6.36E+01
5.04E+00	2.96E+00	8.38E+01	1.03E+02
3.93E+00	3.31E+00	1.03E+03	6.31E+02
3.06E+00	3.72E+00	2.55E+02	4.31E+02
2.38E+00	4.18E+00	6.44E+01	1.92E+02
1.86E+00	4.72E+00	1.06E+02	1.39E+02
1.45E+00	5.14E+00	1.15E+02	4.20E+01
1.30E+00	5.46E+00	3.19E+02	3.56E+01
1.13E+00	5.71E+00	1.59E+03	3.39E+01
1.08E+00	5.82E+00	2.76E+03	3.37E+01
1.04E+00	5.93E+00	2.11E+03	3.36E+01
1.00E+00	6.18E+00	6.57E+02	3.40E+01
8.76E-01	6.53E+00	4.47E+02	3.52E+01
8.00E-01	6.94E+00	6.22E+02	3.74E+01
6.83E-01	7.38E+00	1.18E+03	4.02E+01
6.25E-01	7.84E+00	2.90E+03	4.37E+01
5.32E-01	8.29E+00	9.58E+03	4.72E+01
5.00E-01	8.82E+00	1.93E+04	5.16E+01
4.14E-01	9.52E+00	9.27E+03	5.78E+01
3.67E-01	1.01E+01	7.02E+03	6.31E+01
3.25E-01	1.09E+01	5.56E+03	7.01E+01
2.75E-01	1.19E+01	2.92E+03	7.99E+01
2.25E-01	1.31E+01	2.08E+03	9.17E+01
1.84E-01	1.46E+01	1.91E+03	1.05E+02
1.50E-01	1.60E+01	1.99E+03	1.19E+02

Neutron energy upper bound (eV)	^{59}Co (n,γ)^{60}Co (b)	^{151}Eu (n,γ)^{152}Eu (b)	^{153}Eu(n,γ)^{154}Eu (b)
1.25E-01	1.78E+01	2.28E+03	1.36E+02
1.00E-01	2.06E+01	2.95E+03	1.62E+02
7.00E-02	2.44E+01	4.12E+03	1.97E+02
5.00E-02	2.80E+01	5.45E+03	2.30E+02
4.00E-02	3.17E+01	6.92E+03	2.64E+02
3.00E-02	3.72E+01	9.12E+03	3.13E+02
2.10E-02	4.45E+01	1.22E+04	3.77E+02
1.45E-02	5.35E+01	1.59E+04	4.57E+02
1.00E-02	6.83E+01	2.16E+04	5.87E+02
5.00E-03	9.96E+01	3.34E+04	8.59E+02
2.00E-03	1.65E+02	5.67E+04	1.43E+03
5.00E-04	3.52E+02	1.19E+05	3.04E+03

The lower energy bound for all three reactions was 1.00E-05 eV.

REFERENCES

[1] *Standards for Protection Against Radiation*, in *10 CFR 20*. 2009: United States.

[2] Ansaldo, *IR-DWF-10-000 IRIS Steam Generator Lower Support - Assembly*. 2006.

[3] Ansaldo, *IR-DWF-20 Series - IRIS Steam Generator Tube Bundle*. 2006.

[4] Ansaldo, *IR-DWF-24-000 IRIS Steam Generator Shroud Assembly*. 2006.

[5] Burn, K.W., *IRIS: Monte Carlo Results for Selected Ex-Core Radiation Responses*. 2009, ENEA.

[6] Burn, K.W., *Optimizing Cell Importances Using an Extension of the DSA-Theory Implementation, Preliminary Results.* Progress in Nuclear Energy, 1990. **24**: p. 39.

[7] Carelli, M.D., et al., *The design and safety features of the IRIS reactor.* Nuclear Engineering and Design, 2004. **230**(1-3): p. 151-167.

[8] Carelli, M.D. and B. Petrovic, *Here's Looking at IRIS.* Nuclear Engineering International, 2006. **51**(620): p. 12-18.

[9] Carelli, M.D. and B. Petrovic. *IRIS-Progressing toward a worldwide deployment*. in *Proceedings of the 2006 International Congress on Advances in Nuclear Power Plants*. 2006.

[10] Chadwick, M.B., et al., *ENDF/B-VII.0: Next Generation Evaluated Nuclear Data Library for Nuclear Science and Technology.* Nuclear Data Sheets, 2006. **107**: p. 2931-3060.

[11] Ciotti, M., M. Sarotto, and R. Orsi, *Deterministic Shielding Calculations for the IRIS Reactor*. 2009, ENEA.

[12] Demirbas, A. and S. Karshoglu, *The Effect of Boric Acid Sludges Containing Borogypsum on Properties of Cement.* Cement and Concrete Research, 1995. **25**(7): p. 1381-1384.

[13] Emmett, M.B. and J.C. Wagner, *Monaco: A New 3-D Monte Carlo Shielding Code for SCALE.* Transactions of the American Nuclear Society, 2004. **91**: p. 701-703.

[14] ENSA, *I9219CRQ00 - IRIS General Assembly*. 2008.

[15] ENSA, *I9219CRQ02 - IRIS Cover Head*. 2007.

[16] ENSA, *I9219CRQ04 - IRIS Barrel Assembly Rev. 1*. 2007.

[17] ENSA, *I9219CRQ06 - IRIS Lower Core Plate*. 2008.

[18] ENSA, *I9219CRQ08 - IRIS Reflector*. 2007.

[19] ENSA, *I9219CRQ91 - IRIS Pressure Vessel*. 2008.

[20] Erdogan, Y., A. Demirbas, and H. Genc, *Partly-Refined Chemical By-Product Gypsums as Cement Additives.* Cement and Concrete Research, 1994. **24**(4): p. 601-604.

[21] Franceschini, F., *Fuel Axial Model Revision 1*. 2008, Westinghouse Nuclear.

[22] Franceschini, F. and B. Petrovic, *Impact of the Detailed Fission Source Distribution on IRIS Shielding Analyses.* Nuclear Technology, 2009. **168**(2): p. 431-437.

[23] Haghighat, A. and J.C. Wagner, *Monte Carlo Variance Reductions with Deterministic Importance Functions.* Progress in Nuclear Energy, 2003. **42**(1): p. 25-53.

[24] Hayashi, K., et al., *Development of Low-Activation Reinforced Concrete Design Methodology-II: Concrete Activation Analyses of BWR/PWR.* Nuclear Technology, 2009. **168**(2): p. 571-575.

[25] Henrie, J.O., *Properties of Nuclear Shielding Concrete.* Journal of the American Concrete Institute 1959. **56**(7): p. 37-46.

[26] Herrnegger, F., et al., *Neutron field in the Wendelstein-7-X hall.* Fusion Engineering and Design, 2003. **66-68**: p. 849-853.

[27] IAEA, *Applications of the Concepts of Exclusion, Exemption and Clearance*, in *IAEA Safety Standards Series*. 2004, IAEA: Vienna.

[28] Kaplan, M.F., *Concrete Radiation Shielding: Nuclear Physics, Concrete Properties, Design and Construction*. 1989, New York: Longman Scientific and Technical.

[29] Khripunov, V., R.T. Santoro, and H.Y. Khater, *Profit from Borating Concrete in the ITER Biological Shield.* Fusion Engineering, 1997. **2**: p. 991-994.

[30] Kinno, M., et al., *Development of Low-Activation Reinforced Concrete Design Methodology - I: Manufacture of Low-Activation Concrete.* Nuclear Technology, 2009. **168**(2): p. 564-570.

[31] Lide, D.R., ed. *CRC Handbook of Chemistry and Physics*. 85 ed. 2005, CRC Press: Boca Raton, Florida.

[32] Morioka, A., et al., *Evaluation of radiation shielding, nuclear heating and dose rate for JT-60 superconducting modification.* Fusion Engineering and Design, 2002. **63-64**: p. 115-120.

[33] Nuclear Regulatory Commission. *Decommissioning a Nuclear Power Plant*. 2007; Available from: http://www.nrc.gov/reading-rm/basic-ref/students/decommissioning.html.

[34] Oak Ridge National Laboratory, *Modular Code System for Performing Criticality and Shielding Analyses for Licensing Evaluation with ORIGEN-ARP (Source & Executables)*. 2009.

[35] Oak Ridge National Laboratory, *One, Two- and Three-Dimensional Discrete Ordinates Neutron/Photon Transport Code System, RSICC Code Package CCC-650*. 2007.

[36] Parks, C., *Overview, Applications, and Ongoing Development of the SCALE Code System*. Presentation at Georgia Tech. 12 Feb. 2009.

[37] Peplow, D.E., *MAVRIC: Monaco with Automated Variance Redution Using Importance Calculations.* ORNL/TM-2005/39 Version 6.0, 2009. **I**(S6).

[38] Peplow, D.E., *Monaco: A Fixed-Source, Multi-Group Monte Carlo Transport Code for Shielding Applications.* ORNL/TM-2005/39 Version 6.0, 2009. **II**(F23).

[39] Wagner, J.C., E.D. Blakeman, and D.E. Peplow, *Forward-Weighted CADIS Method for Global Variance Reduction.* Transactions of the American Nuclear Society, 2007. **97**: p. 630-633.

[40] Wagner, J.C. and A. Haghighat, *Automated Variance Reduction of Monte Carlo Shielding Calculations Using the Discrete Ordinates Adjoint Function.* Nuclear Science and Engineering, 1998. **128**: p. 186-208.

[41] Westinghouse Electric Company, *IRIS - 1110-001 Concrete*. 2007.

[42] Westinghouse Electric Company, *IRIS - 1200 Drawing Series*. 2007.

[43] Westinghouse Electric Company. *Issued Design Certification - Advanced Passive 1000 (AP1000), Rev. 15*. 2009; Available from: http://www.nrc.gov/reactors/new-reactors/design-cert/ap1000.html.

[44] Westinghouse Electric Company. *Research Areas*. 2009; Available from: http://www.westinghousenuclear.com/Our_company/Research_&_Technology/research_areas.shtml.

[45] Yarar, Y., *Activation characteristics of concrete shields containing colemanite.* Journal of Nuclear Materials 1996. **233-237**: p. 1511-1515.

[46] Yarar, Y. and A. Bayulken, *Investigation of neutron shielding efficiency and radioactivity of concrete shields containing colemanite.* Journal of Nuclear Materials, 1994. **212-215**: p. 1720-1723.